

PROBING COSMOLOGY AT DIFFERENT SCALES

by

Daniel Pfeffer

A dissertation submitted to The Johns Hopkins University in conformity with the
requirements for the degree of Doctor of Philosophy.

Baltimore, Maryland

October, 2019

© 2019 Daniel Pfeffer

All rights reserved

Abstract

Although we are in an era of precision cosmology, there is still much about our Universe that we do not know. Moreover, the concordance Λ CDM model of cosmology faces many challenges at all scales relevant to cosmology. Either discrepancies have been discovered with Λ CDM predictions or the model has simply broken down and is not a useful predictor. The current rate of expansion is incorrectly predicted by Λ CDM, as are the size and distribution of dwarf halo galaxies for Milky Way like galaxies. Obtaining the observed cores in galaxies with the standard description of dark matter is troublesome and requires more than the base Λ CDM model, as does understanding star formation and how it impacted galaxy evolution requires much more than base Λ CDM knowledge and many more.

My work focuses on probing different scales in cosmology with different techniques to extract information about our Universe and its history. I use ultra-high-energy cosmic-rays (UHECRs) as a probe of the local universe and tested tidal disruption events (TDES) as a possible source of the UHECRs. By analyzing energy require-

ABSTRACT

ments, source densities and observed fluxes, I find that TDEs can explain the observed UHECR flux. The assumption of TDEs as the source of UHECRs can lead to a measurement of the density of super massive black holes which reside in the center of galaxies. At a larger scale, I build a tool to extract the luminosity function of CO from star-forming galaxies with line intensity maps (LIMs) and convolutional neural networks (CNNs). This new technique allows a faster analysis of LIMs in a more model-independent way than previous techniques. Finally, at the largest observable scales, I probe potential dark matter interactions and their impact on the cosmic microwave background (CMB). This work explores how different dark matter interaction mechanisms impact the CMB when considered simultaneously and individually.

As cosmology is a science of many scales, all of these scales must be studied to improve our understanding of the Universe. Dong so, my thesis has wide-ranging implications for cosmic-rays, star formation and galaxy evolution, and dark matter interactions.

ABSTRACT

Readers

Marc Kamionkowski (Primary Advisor)

Emanuele Berti

Brice Menard

Marc Postman

Andy Fruchter

Acknowledgments

It goes without saying that I would not be where I am right now if not for my advisor Marc Kamionkowski. You were always there if I had questions or issues and were very supportive in my shift away from academia at the end. Being in your group helped me grow as a scientist and expand my horizons and gave me the opportunity to learn from many other scientists as well.

Speaking of the Kamionkowski group, I must thank all of the former and current postdocs who I have worked with. I have learned much from our work and interactions. You were always there to help out even when I was slow to grasp a concept or messed up my unit conversions repeatedly. Thank you Ely Kovetz, Simeon Bird, Ilias Cholis, Kimberly Boddy and Vivian Poulin.

Many fellow graduate students have come and gone along this journey of mine. To my Bloomberg 423 office mates Patrick Breyse, Alice Cocoros, Bhaskar Balaji and Gabriela Sato-Polito, thank you for being there for stupid questions, goofing off with me and not commenting when I jam out to my music. To Patrick Breyse

ACKNOWLEDGMENTS

(again) and Julian Muñoz as more senior graduate students in the group, thank you for being another resource to the wonderful world of cosmology. To Tanvi Karwal, we have been in the same boat now for the past five years and it has been fun going through the entire experience with you even if we cannot work together without immediately yelling at each other. I also have to give a shout out to my lifting crew, Kim Berghaus, Michael Busch, Tanvi Karwal (again) and Lingyuan Ji. Even if I did not learn anything in the past couple of years, I have definitely gotten into much better shape.

Of course I must thank Kelley Key. My time here would not have been the same without someone like you in the administration and as a friend.

Finally I must thank my parents, Gerry Pfeffer and Cindy Virgil as well as my brother Alex Pfeffer. I am where I am because of the interactions I had with you three over the course of my life. You always encouraged me no matter which path I chose in life.

Dedication

To my loving parents and brother.

I have the final proof that I am the smarter son.

Contents

Abstract	ii
Acknowledgments	v
List of Tables	xi
List of Figures	xii
1 Introduction	1
2 TDEs and UHECR Hot Spots	9
2.1 The hot and warm spots	12
2.2 Time scales and energetics	14
2.3 Isotropic flux	19
2.4 Discussion: TDE scorecard	23
2.5 Conclusions	25
3 LIM with Neural Networks	27
3.1 Simulated Maps	34

CONTENTS

3.1.1	Dark Matter Simulations	35
3.1.2	CO Modelling	36
3.1.3	Noise and Foregrounds	38
3.2	Convolutional Neural Network	46
3.2.1	Network Architecture	47
3.2.2	Implementation	51
3.3	Results	56
3.3.1	Tests on trained data	59
3.3.2	Tests on untrained data	65
3.4	Discussion	70
3.5	Conclusion	73
4	Interacting DM Signatures on the CMB	74
4.1	Modified CMB physics	78
4.1.1	Dark matter scattering	78
4.1.2	Dark matter annihilation	81
4.2	Scattering and annihilation signals in the CMB	83
4.2.1	Previous limits from <i>Planck</i>	84
4.2.2	Both effects from multiple couplings	88
4.2.3	Both effects from scattering saturation	91
4.3	Looking for electromagnetic signals of Dark Matter in CMB data	94
4.3.1	Dipole dark matter	95
4.3.2	Millicharge dark matter	98

CONTENTS

4.4 Discussion/Conclusions	104
Appendix	107
A.1 Benchmark models of dark matter	107
A.1.1 Dipole dark matter	107
A.1.2 Millicharge dark matter	109
Bibliography	111
Vita	148

List of Tables

3.1	Experiment setup for COMAP Phase one	35
3.2	Summary of models used for Resnet testing	40
3.3	Resnet Architecture	51
3.4	Resnet accuracy	68

List of Figures

3.1	Parameter space of luminosity function values used in training	39
3.2	Line Intensity Map Slices with and without noise	45
3.3	Residual block structures	48
3.4	Set of residual blocks	52
3.5	Full Resnet architecture diagram	53
3.6	Training loss history	55
3.7	Resnet example tests	57
3.8	Resnet comparison to PS/VID technique	61
3.9	Resnet relative error on simple LIMs	62
3.10	Resnet relative error on random LIMs	64
3.11	Resnet relative error on LIMs with untrained features	67
3.12	Zoom in of Resnet relative errors	69
4.1	Analytic predictions to determine which dark matter interaction dominates	86
4.2	Dipole dark matter CMB power spectra residuals	88
4.3	Millicharge dark matter CMB power spectra residuals	91
4.4	Dipole dark matter exclusion contour	97

LIST OF FIGURES

4.5	Millicharge dark matter individual affect exclusion contours	101
4.6	Millicharge dark matter exclusion contours	102

Chapter 1

Introduction

Cosmology is a field of many scales with different physics governing these different scales. The universe itself is large, but its history and evolution vary based on what scale is being considered. Dwarf galaxies orbiting Milky-Way-like galaxies are described differently than the large-scale structure governing superclusters of galaxies. At still larger scales, cosmologists study the cosmic microwave background (CMB), the oldest light in the Universe, the scale of which is the size of the observable Universe. At the other end of the spectrum, the physics of very small scale is also relevant to cosmology. The early universe was a much denser and hotter place and is described by particle physics. Therefore, in attempting to understand the nature of the universe, we must learn about physics at many scales.

Due to its agreement with numerous data sets, the flat Λ CDM model has become the concordance model of cosmology [1–13]. Within Λ CDM there is radiation, baryon, cold dark matter (CDM) and dark energy. Radiation encompasses either photons or any relativistic

CHAPTER 1. INTRODUCTION

species of matter and is negligible in terms of its impact on the universe today. Baryons or what people generally consider as normal matter make up roughly 5% of the energy density of the universe. A slightly different form of matter is cold dark matter which accounts for 25% of the energy density of the universe. It is cold because it has little to no thermal velocity and is dark because we do not observe it through interactions with photons [14,15], but rather only gravitationally [16–18]. The rest of the universe, around 70%, is in the form of dark energy which would explain the accelerated expansion of the universe [19–22]. Dark energy can take many forms, but the simplest model that is extremely successful is that it is a cosmological constant Λ .

Although Λ CDM does an excellent job of describing the universe, it is not perfect and there is much room for improvement. Nearly perfect fluids are used in Λ CDM to describe the components of the Universe. Small perturbations to these fluids describe the growth and formation of structure. However, this approach fails when perturbations become too large and non-linear as they must to correctly evolve to today’s Universe. CDM can explain the density profiles, number densities and hierarchical nature of galaxies, but does not correctly predict the density profiles in the center of galaxies, nor the right number and size of dwarf galaxies [23–29]. Small changes to the CDM model such as allowing the dark matter to self-interact may alleviate some of these issues [24, 30, 31]. These changes would leave an imprint in the CMB. However, dark matter is not the only ingredient in our Universe, galaxies also contain baryons. Complex baryonic physics also influences galactic structure formation. Baryons may cause feedback in galaxies and shape the distribution of matter within [32–36]. It is possible that baryonic physics may be a solution to the lack of dwarf

CHAPTER 1. INTRODUCTION

galaxies observed [37–39]. Our observations of the Universe depend on the light we observe, but that can be heavily influenced by the baryonic physics within galaxies that is not fully understood. To uncover the mysteries of the Universe, my research is focused on probing the universe at different scales to better understand its structure and evolution.

This thesis is divided into the following chapters. In Chapter 2, I present my work with ultra-high-energy cosmic rays¹(UHECRs), both within an observed hot spot and the isotropic flux. In this work, I concentrated on the local universe and was interested in the energetics and distribution of sources required to produce the observed UHECR flux [40]. I find that tidal disruption events (TDEs) could be a possible source of the observed UHCER hot spot as well as the isotropic flux due to their rates, density of source black holes and fraction of energy that can be converted from the TDE itself into UHECRs. Simply put, TDE happen when a star comes close enough to a super massive black hole (SMBH) such that gravitational tidal forces overcome the binding energy of the star and tear it apart. Some fraction of the star will then form a short-lived accretion disk that produces an intense flair [41]. Jets can be produced by the TDEs that can then accelerate particles to ultra-high energies. On a slightly larger scale, I was interested in how one can extract information from line intensity maps (LIMs). LIMs are three dimensional images that are obtained by observing a single spectral line at multiple redshifts. They give us a low resolution spatial map of the structure of the universe and can access previously un-probed regions of the universe. In Chapter 3, I present my work in a new, semi-model-independent framework to extract the luminosity function of the source galaxies from LIMs. Instead of the conventional power spectrum and voxel intensity distribution technique, I make use

CHAPTER 1. INTRODUCTION

of the machine-learning tool of convolutional neural networks [42]. Finally, in Chapter 4, I explore the largest distance scales in cosmology with the CMB, in particular, the effects of DM interacting with the visible sector on this observable. Here I compare and contrast the effects of DM-baryon scattering and DM self annihilation on the CMB and determine the circumstances that dictate which of these effects dominates the resultant constraints [in preparation]. Doing so, I find regions where the two effects are comparable and must both be considered to derive constraints. In these regions, new CMB observables are predicted. Furthermore, two specific models are tested and I find caveats to the general predictions of which interaction dominates.

Of the many scales relevant to cosmology, in Chapter 2, I explore the smaller, intergalactic scales with UHECRs. In the past decade, the ability to observe UHECRs has improved significantly with the advent of the Pierre Auger Observatory (PAO) and the Telescope Array (TA). Recently, both the TA and the PAO have detected regions of excess UHECRs as compared to an isotropic background [43, 44], with statistical significances of $\gtrsim 3\sigma$ and $\gtrsim 2\sigma$, respectively. Even barring the observed excesses, the sources of UHECRs themselves remain unknown.

This work explores the local universe for two reasons. Firstly, although UHECRs are expected to be extra-galactic, they cannot come from too far away. UHECRs may interact with CMB photons during their flight and lose a large fraction of their energy [45, 46]. UHECRs are hence not expected to survive a journey of more than 200 Mpc. Secondly, the observed excesses are expected to originate somewhere close to the Milky Way. Due to

¹For the purpose of this work, UHECRs will be defined as cosmic rays with energies above 57 EeV.

CHAPTER 1. INTRODUCTION

intergalactic magnetic fields, the UHECRs will be randomly deflected during their flight [47]. Any source much farther than 4 Mpc away will spread out its cosmic rays over a large patch of the sky rather than appear as a sky-localized excess.

Active-galactic-nuclei (AGN) and gamma-ray bursts (GRBs) have been suggested to be UHECR sources, but they run into some unresolved problems [48–50]. We instead explore the possibility of using TDEs to explain the UHECR flux. The flux of UHECRs we would observe depend on a few factors. These factors include the distance to the host galaxy and the mass of the SMBH. From the SMBH mass we can then determine the rate of TDEs in a given galaxy [51]. While the UHECRs would be released during a small timescale, we observe them over a long time scale (possibly tens of thousands of years) [47, 52]. This spread is due to the random strengths and orientations of intergalactic magnetic field orientations along the path of the UHECR from the host galaxy to the Milky Way. Cosmic rays with different energies are deflected differently and have different path lengths, spreading out their arrival time. For the localized excesses, I investigated whether a single source could both produce the amount of excess observed and do it continuously. The local UHECR hot spot is used to fit parameters to determine the UHECR flux from a single TDE which is then used to predict the isotropic UHECR flux that should be observed on Earth. I find the expected isotropic flux is in rough agreement with the observed one. On relaxing some assumptions that went into the calculation, the observational and theoretical fluxes can match better.

Chapter 3 focuses on a new technique I engineered to gain information from line intensity maps (LIMs). LIMs probe galaxy evolution and large-scale structure without resolving

CHAPTER 1. INTRODUCTION

individual emitting sources. They map the aggregate emission of a single spectral line over cosmological scales [53]. Specifically, this work relates to the carbon monoxide (CO) Mapping Array Pathfinder (COMAP) experiment which maps the CO emission from star-forming galaxies over redshifts $2.4 - 3.4$ [54]. The distance scale this work explores is of the order of a few tens of thousands of Mpc (~ 100 times larger than the scales in Chapter 2).

LIMs are a relatively new technique to conduct surveys that are not luminosity-limited. This emerging field is still figuring out how to extract as much information as possible from these maps. In this chapter, I develop a new technique to determine the underlying CO galaxy brightness luminosity function from a LIM. There is no direct way to go from a LIM to the underlying luminosity function so non-analytic techniques must be used. A previous method involved running a Markov Chain Monte Carlo and assumed a physical model to fit which parameters of the model would result in an LIM with a power spectrum and voxel intensity distribution (PS/VID) that match that of the observed LIM [55]. This technique is slow and strongly model dependent. My new method makes use of machine learning, specifically convolutional neural networks (CNNs). A CNN is a machine-learning tool meant for extracting information from images and a LIM is just a three-dimensional image. The CNN was trained to take in a single LIM with possible noise and foregrounds and to return the underlying CO galaxy brightness luminosity function. A specific model was chosen to generate mock LIMs to train on, but the CNN was trained to be as model independent as possible. I found that the trained CNN was as or more accurate than the PS/VID method, as well as orders of magnitude faster and more robust. When tested on mock LIMs made with a different underlying physical model, the CNN had biases in its

CHAPTER 1. INTRODUCTION

expected luminosity function, but was still fairly accurate. More work must be done to optimize the use of CNNs for LIMs, but this work was the first step in introducing their use to the LIM community.

Finally, in Chapter 4, I compare the effects of dark matter annihilation and baryon scattering on the CMB. The CMB contains information about the early Universe, a much younger, denser and warmer place. A snapshot of the density perturbations at that time is encoded in the temperature and polarization anisotropies of CMB light. The CMB is a powerful tool to investigate the interactions of dark matter as it encompasses a large range of scales - from the size of the observable universe down to the small scales of particle physics and particle interactions. New dark matter interactions will change how these perturbations evolved and what they looked like when the photons of the CMB last scattered [13, 56–83]. Previous studies of the impact of interacting dark matter on the CMB have generally focused on individual interactions at a time. It is unclear if these interactions should be studied separately or if a joint analysis is necessary. My work aims to determine the circumstances under which these interactions can be considered individually and when they must be considered simultaneously as well as general classes of models for which either interaction dominates the constraints.

By comparing interaction rates for baryon scattering and annihilation to their individual CMB limits, I determined the scenarios in which scattering would dominate and when annihilation would dominate the CMB constraints. I then test individual interaction models to confirm the analytic prediction and check for new possible signatures in the CMB. For these individual models, the analytic predictions were confirmed, and regions of parameter

CHAPTER 1. INTRODUCTION

space were found where both models equally impacted the CMB leading to new features in the CMB power spectra.

By probing the universe at different scales, we obtain different information about its structure and evolution. The flux of UHECRs gives information about the density and distribution of local galaxies as well as a test of astrophysical mechanisms required to produced them. The CO LIMs explore properties of galaxies around the peak of star formation. Through the CMB power spectra, we can learn about the early universe as well as the particles that make up everything. Combining information from all these scales and times will lead to a better understanding of our Universe.

Chapter 2

Ultra-high-energy-cosmic-ray hotspots from tidal disruption events

In the past decade the ability to observe ultra-high-energy cosmic rays¹(UHECRs) has increased significantly with the advent of the Pierre Auger Observatory (PAO) and the Telescope Array (TA). Recently, both the TA and the PAO have detected regions of excess UHECRs as compared to an isotropic background [43, 44], with statistical significances of $\gtrsim 3\sigma$ and $\gtrsim 2\sigma$, respectively.

The sources of UHECRs are still unknown. One possibility is active-galactic-nucleus jets [48]. However, Ref. [84] derived a relation between the AGN electromagnetic luminosity

¹For the purpose of chapter work, UHECRs will be defined as cosmic rays with energies above 57 EeV.

CHAPTER 2. TDES AND UHECR HOT SPOTS

and its UHECR luminosity. Reference [49] then used the Veron-Cetty and Veron catalogue [85], along with this luminosity relation, to infer that the observed AGN are not luminous enough to explain the full-sky UHECR flux. Gamma-ray bursts (GRBs) are also capable of producing UHECRs [50], but they would have to have a rather flat spectrum of UHECRs produced by an individual GRB and would have to yield far more energy to UHECRs than to photons in order to explain the full-sky flux [84].

We consider a third mechanism as the dominant source of UHECRs, namely tidal disruption events (TDEs). A star is disrupted by a super massive black hole (SMBH) when it passes by close enough that tidal forces overcome the binding energy of the star. Some fraction of the star then becomes bound to the SMBH and forms a short-lived accretion disk which produces an intense flare², while the rest continues on [41]. Some of the TDEs produce jets, which were first proposed as a source of UHECRs in Ref. [84], and then expanded upon in Ref. [52], which showed that they can generate the luminosity required to account for the full-sky UHECR flux.

In 2014, the TA reported a “hot spot” of UHECRs in a circle of radius 20° , centred at a right ascension of $146.^\circ7$ and declination of $43.^\circ2$ [43]. Reference [86] tried to identify possible extragalactic sources for the hot spot, taking into account possible deflection of the UHECRs by Galactic and intergalactic magnetic fields. After accounting for random deflections by stochastic intergalactic magnetic fields (IGMFs), they drew a straight line through the images of the different rigidity bins of the events in the hotspot, expecting

²The SMBH does not need to be an AGN—i.e., actively accreting from the accretion disk—in order for the disruption to cause rapid accretion. The in-falling gas from the disrupted star could form an accretion disk with rapid accretion resulting in a relativistic jet outflow [84].

CHAPTER 2. TDES AND UHECR HOT SPOTS

the source to lie along this line. Two possible sources were identified, M82 and Mrk 180. While Mrk 180 is located roughly 185 Mpc away, near the GZK radius, and is thus unlikely to be the source, M82 is a starburst galaxy only 3.8 Mpc away [87] and moreover has a $\sim 3 \times 10^7 M_\odot$ SMBH at its centre [88]. The SMBH does not exhibit any AGN activity.

Likewise, the Pierre Auger Observatory has noted a “warm spot,” an excess of events in the direction of Centaurus A (Cen A). Cen A is also (coincidentally) approximately 3.8 Mpc away [89], with a SMBH with a mass estimated to be $5 \times 10^7 M_\odot$. Unlike M82’s, this SMBH does exhibit AGN activity.

In this chapter we investigate whether the TA hotspot can be explained by TDEs in M82. We first derive basic constraints to the model parameters from timescale and energetic arguments. We surmise that the UHECR hot spot is in roughly steady state in which the UHECR flux results from several TDEs that have occurred within the timescale for dispersion of a burst signal due to deflections in the Galactic and intergalactic magnetic fields (although we do briefly consider the possibility that the hot spot arises from a single burst.) This hypothesis is consistent if UHECRs are composed of protons or heavier nuclei such as iron, although the consistent parameter space is a bit smaller for heavier nuclei. Similar arguments apply to the warm spot from Cen A. We then investigate whether the UHECR luminosity density implied by the observed fluxes from the SMBHs in M82 and Cen A is consistent with the isotropic UHECR intensity that is observed. We find that the isotropic flux inferred in this way is higher, by about a factor of 16, than the observed isotropic flux, but we point out several factors that might alleviate the apparent discrepancy.

CHAPTER 2. TDES AND UHECR HOT SPOTS

The rest of this chapter is organized as follows. In Section 2.1, we review briefly the evidence for the TA hot spot and the PAO warm spot and provide the fiducial values we use for the hot-spot and warm-spot fluxes as well as the isotropic UHECR intensity. In Section 2.2 we discuss the constraints to TDE scenarios for the UHECR hot/warm spots that arise from energetics and timescale considerations. In Section 2.3 we consider constraints to the scenario that arise from consistency of the hot/warm-spot fluxes with the isotropic UHECR intensity. In Section 2.4 we summarize, review the successes and weaknesses of the TDE explanation for the hot/warm spots, and close with some speculations. In Section 2.5 we conclude by considering some possible future measurements.

This chapter is based heavily on work in [40] with coauthors Ely D. Kovetz and Marc Kamionkowski.

2.1 The hot and warm spots

The TA Collaboration reports evidence [43] for a UHECR excess in a circle of 20° radius. Because the TA does not report a value for the intensity in the hot spot, we use a value from Ref. [90] who infer the (number) intensity J_{hs} in this hot spot to be,

$$E^2 J_{\text{hs}} = (4.4 \pm 1.0) \times 10^{-8} \text{ GeV cm}^{-2} \text{ s}^{-1} \text{ sr}^{-1}, \quad (2.1)$$

at an energy $E = 10^{19.5}$ eV. The hot-spot energy flux in UHECRs with energies > 57 EeV is $F_{\text{hs}} = \Omega_{20^\circ} \int_{57 \text{ EeV}}^{\infty} E J_{\text{hs}}(E) dE$, where $\Omega_{20^\circ} \simeq 0.38$ sr is the hot-spot solid angle. The

CHAPTER 2. TDES AND UHECR HOT SPOTS

energy dependence of $J_{\text{hs}}(E)$ at energies above 57 EeV is, however, quite uncertain in the hot spot, and even for the full-sky flux [see, e.g., Fig. 7 in Ref. [91], which shows considerable disagreement between PAO and TA at the highest energies], so we use $\int_{57 \text{ EeV}}^{\infty} E J_{\text{hs}}(E) dE = E^2 J_{\text{hs}}|_{E=57 \text{ EeV}}$. We therefore take the energy flux in the hot spot to be,

$$F_{\text{hs}} = 1.7 \times 10^{-8} F_{1.7} \text{ GeV cm}^{-2} \text{ s}^{-1}, \quad (2.2)$$

and keep the quantity $F_{1.7}$, which parametrizes our uncertainty in the flux, in our expressions below.

Likewise, we take the observed isotropic (energy) intensity above 57 EeV to be $I_o = 7.9 \times 10^{-9} \text{ GeV cm}^{-2} \text{ s}^{-1} \text{ sr}^{-1}$. We take this value from Ref. [91] which uses data from Refs. [92] and [93]. Again, to be consistent with our treatment of the hot-spot flux, we take this to be the value of $E^2 J_{\text{iso}}$ at $E = 57 \text{ EeV}$. This isotropic flux appears below only in comparison to the hot-spot flux, and so it is appropriate to treat the full-sky flux in the same way as the hot-spot flux.

We estimate the UHECR energy flux from Cen A implied by the PAO warm spot as follows: Ref. [94] finds 13 events within a circle of radius 18° , where 3.2 are expected from an isotropic distribution. We thus take the energy flux from Cen A to be $(13 - 3.2)/3.2 \approx 3$ times the isotropic energy flux in that circle, or

$$F_{\text{ws}} = 7.6 \times 10^{-9} \text{ GeV cm}^{-2} \text{ s}^{-1}, \quad (2.3)$$

CHAPTER 2. TDES AND UHECR HOT SPOTS

keeping in mind the considerable uncertainty in this value.

2.2 Time scales and energetics

Our aim here is to understand whether TDEs from accretion of stars onto the SMBH in M82 may be responsible for the UHECR hot spot. We begin with some basic considerations, starting with time scales.

The hot spot is observed to be spread over an angular region of size $\theta \sim 20^\circ$. Such a spread is to be expected due to scattering in turbulent intergalactic magnetic fields (IGMFs) as the UHECRs propagate the 3.8 Mpc distance from M82, and there may be additional scattering (particularly for iron nuclei) from magnetic fields in the Milky Way. The rms deflection angle for a UHECR of charge Z in a homogeneous turbulent magnetic field in the limit of small deflections per coherence length is [47],

$$\delta_{\text{rms}} \approx 3.6^\circ Z E_{20}^{-1} r_{100}^{1/2} \lambda_{\text{Mpc}}^{1/2} B_{\text{nG,rms}}, \quad (2.4)$$

where $B_{\text{nG,rms}}$ is the rms strength of the magnetic field in nG, E_{20} is the UHECR energy in units of 10^{20} eV, $r_{100} = r/100$ Mpc is the distance over which the magnetic fields act, and λ_{Mpc} is the magnetic-field coherence length in units of Mpc. We take $\delta_{\text{rms}} = \theta/2$ so that a 2-dimensional region of size θ encloses $\sim 86\%$ of the events. Consider first scattering in Galactic magnetic fields. Characteristic values might then be $\lambda_{\text{Mpc}} \sim 10^{-4}$, $r_{100} \sim 10^{-4}$, and $B_{\text{nG}} \sim 10^3$ [95], implying Galactic deflection angles $\delta_{\text{rms,GMF}} \sim 0.36^\circ Z$. We thus infer,

CHAPTER 2. TDES AND UHECR HOT SPOTS

for these values, that for iron nuclei all the scattering could conceivably arise from Galactic magnetic fields, although for protons, the scattering must arise in the IGMF. The value of λ_{Mpc} within the Milky Way is, however, not fully agreed upon yet [95]. A value of λ_{Mpc} slightly larger than 10^{-4} would still give a $\delta_{\text{rms}} \sim 10^\circ$ for iron nuclei, but a smaller value would require the scatter of iron nuclei in the IGMF to be comparable to or greater than the scatter in the GMF. Although we have surmised that UHECRs are dispersed by turbulent magnetic fields, there could also be some additional dispersion due to coherent fields [96] in the Galaxy.

Either way, scattering in magnetic fields also gives rise to a spread [50, 52]

$$\begin{aligned}\tau &\simeq 3 \times 10^5 \left(\frac{r_{100} B_{\text{nG}}}{E_{20}} \right)^2 \lambda_{\text{Mpc}} Z^2 \text{ yrs} \\ &\simeq 3.5 \times 10^5 \left(\frac{\delta_{\text{rms}}}{3.6^\circ} \right)^2 r_{100} \text{ yrs},\end{aligned}\tag{2.5}$$

in the arrival times for UHECRs from a single TDE. Thus, if all the scattering takes place in the Milky Way, for which $r_{100} \sim 10^{-4}$, then $\delta_{\text{rms}} \sim 10^\circ$ implies a dispersion of $\tau \sim 270$ yrs in the UHECR arrival times. If scattering occurs primarily in IGMFs, then the spread in arrival times is $\tau \sim 10^5$. This is also roughly the same value of τ for iron nuclei if they are scattered a comparable amount in the IGMF and GMF. *We thus infer that UHECRs are spread in arrival time by some magnetic-dispersion timescale $270 \text{ yrs} \lesssim \tau \lesssim 10^5 \text{ yrs}$, with protons and iron nuclei at the higher end for a strong IGMF and iron nuclei at the lower end only if there is an extremely weak IGMF ($B_{\text{nG}} \approx 10^{-3} \text{ nG}$).*

We now consider energetics. If the observed flux of UHECRs in the hot spot is $F_{\text{hs}} \simeq$

CHAPTER 2. TDES AND UHECR HOT SPOTS

$1.7 \times 10^{-8} F_{1.7} \text{ GeV cm}^{-2} \text{ sec}^{-1}$, then the implied isotropic-equivalent source luminosity is $L = 4\pi D^2 F \simeq 8.3 \times 10^{-7} F_{1.7} M_{\odot} c^2 \text{ yrs}^{-1}$ (where $D = 3.8 \text{ Mpc}$ is the distance). If the observed UHECRs are due to a single TDE spread over a time τ , then the isotropic-equivalent energy implied with $\tau \simeq 270 \text{ yrs}$, the minimum τ possibly allowed for iron nuclei, is $2.2 \times 10^{-4} F_{1.7} M_{\odot} c^2$. If the dispersion time is $\tau \simeq 10^5 \text{ yrs}$, the value required for protons, then the isotropic-equivalent energy is $8.3 \times 10^{-2} F_{1.7} M_{\odot} c^2$. Of course, if the TDE is beamed into a solid angle that subtends a fraction $\Omega_{\text{jet}} \sim 0.1$ of 4π , then the energy requirements can be relaxed by a factor ~ 10 . Still, we conclude that if UHECRs are iron nuclei, the hot spot is conceivably due to a single burst. If the UHECRs are protons, the energetics are prohibitive, unless the Milky Way magnetic-field parameters are altered so that the angular spread in the hot spot arises from scattering in the Milky Way. Even if the energetics can somehow be worked out, the notion that we are seeing a hot spot just from M82 because of some chance occurrence (an extraordinarily energetic TDE at just the right time) is unsatisfying, and even more unsatisfying if we must also explain the warm spot as some similar chance occurrence in Cen A.

Another possibility is that the observed hot spot arises not from a single TDE, but from a number of TDEs in M82. This may occur if the dispersion τ in arrival times exceeds the typical time Δt between TDEs in M82. If so, then we are seeing UHECRs from $N \simeq (\tau/\Delta t) \gtrsim 1$ bursts at any given time. The hot-spot flux in this case will vary by a fractional amount $\sim N^{-1/2}$ over timescales $\sim \tau$. However, over the $\sim 5\text{-yrs}$ observation, the observed flux will remain effectively constant. This scenario, as we will now show, is plausible.

CHAPTER 2. TDES AND UHECR HOT SPOTS

We suppose that stars (which we assume for simplicity to all have a mass M_\odot) are captured by the SMBH with a rate Γ . We then suppose that only a fraction ζ produce the type of jets that can accelerate UHECRs and that a fraction ξ of the stellar rest-mass energy $M_\odot c^2$ goes into UHECRs. We further suppose that the UHECR emission may be beamed into a fraction Ω_{jet} of the 4π solid angle of the sphere. In order to obtain the observed UHECR hot-spot flux in steady state, we require that stars be captured by the SMBH at a rate,

$$\Gamma = 8.3 \times 10^{-7} \left(\frac{\Omega_{\text{jet}} F_{1.7}}{\xi \zeta} \right) \text{ yrs}^{-1}. \quad (2.6)$$

The mean time between UHECR-producing events is

$$\Delta t = (\zeta \Gamma)^{-1} = 1.26 \times 10^6 \frac{\xi}{\Omega_{\text{jet}} F_{1.7}} \text{ yrs}. \quad (2.7)$$

Both equations (2.6) and (2.7) are for a single SMBH with jets produced by TDEs pointed at the Earth. Here we assume that all of the jets produced by TDEs from a particular SMBH will always point in the same direction. If we were to assume that the direction of these jets were uncorrelated with each other, then an extra factor of Ω_{jet} would need to be added to equations (2.6) and (2.7). The new factor of Ω_{jet} would cancel out with the previous because only Ω_{jet} percentage of jets would be beamed towards the Earth. If this mean time is to be smaller than the magnetic-dispersion time τ , we require

$$\frac{\xi}{\Omega_{\text{jet}} F_{1.7}} \lesssim 7.7 \times 10^{-2} \tau_5, \quad (2.8)$$

where τ_5 is the magnetic-dispersion time in units of 10^5 yrs.

CHAPTER 2. TDES AND UHECR HOT SPOTS

We now compare the mass-accretion rate implied by equation (2.6) with the Eddington rate $\dot{M} = L_{\text{Edd}}/c^2 \simeq 3.8 \times 10^{45} M_3 \text{ erg s}^{-1}/c^2$, where M_3 is the SMBH mass in units of $3 \times 10^7 M_\odot$, for M82. Assuming that half of the disrupted star's mass is accreted, we find that the mass-accretion rate is smaller than Eddington if

$$\frac{\xi}{\Omega_{\text{jet}} F_{1.7}} \gtrsim 6.0 \times 10^{-6} M_3^{-1} \zeta^{-1}. \quad (2.9)$$

It is not, strictly speaking, required that this condition be respected. It is conceivable that a SMBH could appear quiescent, even with a super-Eddington time-averaged mass-accretion rate, if the accretion is episodic. Still, the scenario may be a bit more palatable if we do not have to wave away a super-Eddington accretion rate in this way. Or put another way, it is simply interesting to note that the scenario can work with a sub-Eddington time-averaged accretion rate as long as equations (2.8) and (2.9) are satisfied, or as long as

$$\zeta \gtrsim \frac{7.6 \times 10^{-5}}{\tau_5 M_3}. \quad (2.10)$$

This quantity must be $\zeta \leq 1$, and is estimated to be $\zeta \sim 0.1$ [52] (although that is a value for the average over all SMBHs, and does not necessarily apply to a single SMBH). Such a value is easily accommodated if $\tau_5 \sim 1$, as we might expect for UHECR protons, and even fits for iron nuclei, for which the lowest possible magnetic dispersion time gives $\tau_5 \sim 2.7 \times 10^{-3}$.

We have thus shown that the TA hot spot can be explained as a roughly steady-state phenomenon by the sub-Eddington capture and tidal disruption of stars by the SMBH in M82. The scenario works independent of whether the UHECRs are protons or iron nuclei,

CHAPTER 2. TDES AND UHECR HOT SPOTS

although the timescale parameter space is a bit narrower for iron nuclei, a consequence of the larger deflection of iron nuclei in the Milky Way magnetic field.

2.3 Isotropic flux

We now investigate whether the isotropic UHECR flux implied by this scenario is consistent with that observed under the assumption that the UHECR luminosity of M82 and of Cen A are fairly typical for such SMBHs. This analysis applies not only to the hypothesis that TDEs are responsible for the hot and warm spots, but to any scenario in which there are hot/warm spots associated with Cen A and M82.

We begin with a simple analysis. The isotropic-equivalent luminosities of M82 and Cen A are, respectively, $2.9 \times 10^{43} F_{1.7} \text{ GeV s}^{-1}$ and $1.4 \times 10^{43} F_{1.7} \text{ GeV s}^{-1}$. Both SMBHs are at a distance $R \lesssim 4 \text{ Mpc}$, and so the UHECR luminosity density in a 4-Mpc sphere around us is $\rho_L \simeq 5.4 \times 10^{-33} F_{1.7} \text{ GeV cm}^{-3} \text{ s}^{-1}$. If the UHECR emissions from Cen A and M82 are both beamed into a fraction Ω_{jet} of the 4π solid angle, then ρ_L is reduced by Ω_{jet} . If M82 and Cen A are not atypical, though, then there must be $\sim \Omega_{\text{jet}}^{-1}$ other beamed UHECR sources, aimed in other directions, for every source that we see. This then cancels the Ω_{jet} beaming reduction leaving ρ_L unchanged. Since both Cen A and M82 appear, in the jetted-TDE scenario, to be aimed at us, we infer that Ω_{jet} is unlikely to be small in this scenario. The tension we will find below between the hot/warm-spot fluxes and the isotropic intensity can be relaxed, though, if both Cen A and M82 just happen to be highly beamed and both in our direction. If our local neighbourhood is not atypical, then ρ_L provides an estimate of

CHAPTER 2. TDES AND UHECR HOT SPOTS

the universal UHECR luminosity density. If the local density is greater by a factor f_ρ than the cosmic mean density, then the universal UHECR luminosity density is ρ_L/f_ρ .

The isotropic UHECR intensity (energy per unit area per unit time per unit solid angle) is

$$I = \int_0^{R_G} dr r^2 f(r) \frac{\rho_L}{4\pi r^2} = \frac{\rho_L}{4\pi} \int_0^{R_G} dr f(r) = \frac{\rho_L R_G}{8\pi}, \quad (2.11)$$

where $R_G \simeq 200$ Mpc is the GZK radius, and the second equality is obtained by approximating the fraction of UHECR energy emitted at a distance r that makes it to us to be $f(r) \simeq 1 - (r/R_G)$ [97]. If the TA hot spot and PAO warm spot are real and attributed to M82 and Cen A, respectively, then the isotropic UHECR flux should be $I = 1.37 \times 10^{-7} F_{1.7} f_\rho^{-1} \text{ GeV cm}^{-2} \text{ s}^{-1} \text{ sr}^{-1}$. This is, for $f_\rho = 1$, 16 times greater than the isotropic intensity $I_o = 7.9 \times 10^{-9} \text{ GeV cm}^{-2} \text{ s}^{-1} \text{ sr}^{-1}$. The discrepancy cannot be alleviated with a smaller value of $F_{1.7}$ because, as discussed after equation (2.2), we are using the specific intensities at $E \simeq 10^{19.5}$ eV, which are fairly well determined, as proxies for the full energy flux and isotropic intensity.

It is, however, likely that the tension can be alleviated, at least in part, with a value $f_\rho > 1$. The local overdensity is uncertain, but as one indication of the value of f_ρ , we can use the total SMBH mass in the $R \simeq 4$ Mpc sphere, assuming that the UHECR luminosity density is proportional to the density of mass SMBHs. In addition to the SMBHs in Cen A and M82, there is also the $\sim 4 \times 10^6 M_\odot$ SMBH in the Milky Way and the $\sim 10^8 M_\odot$ SMBH in Andromeda, a $\sim 7.7 \times 10^7 M_\odot$ SMBH in M81, as well as a $\sim 10^6 M_\odot$ SMBH in M32. This totals to $\sim 2.5 \times 10^8 M_\odot$ in SMBHs within a distance $R \simeq 4$ Mpc implying a

CHAPTER 2. TDES AND UHECR HOT SPOTS

local SMBH density $\simeq 9.3 \times 10^5 M_\odot \text{ Mpc}^{-3}$, roughly 3 times the universal SMBH density $\simeq 2.9 \times 10^5 M_\odot \text{ Mpc}^{-3}$ [98]. There is still residual factor of ~ 5 discrepancy that remains, even accounting for this $f_\rho \sim 3$, that must be accounted for if the TDE explanation for the TA and PAO hot spots is to remain viable. This level of discrepancy is we believe, given the order-of-magnitude nature of the analysis, as well as the measurement and astrophysical uncertainties, not necessarily fatal for the TDE scenario. The local luminosity density ρ_L we inferred could have been reduced a bit by considering a sphere of slightly larger radius; there are uncertainties almost of order unity in the measured fluxes; and the Poisson fluctuation in our inference of ρ_L is also of order unity.

So far we have been using the UHECR flux from M82 and Cen A to infer a luminosity density, and the uncertainty from small-number statistics has been noted above. There is, however, an additional uncertainty that may arise from the dependence of the mean TDE rate on SMBH mass. SMBHs are distributed with a mass function dn/dM [98, 99], and there is evidence that the TDE rate varies with the SMBH mass. We infer an UHECR luminosity density from measurement of the UHECR flux from one or two $\sim 3 \times 10^7$ SMBHs. Suppose, though, that the TDE rate varies as $\Gamma(M) = \Gamma(M = 3 \times 10^7 M_\odot)(M/3 \times 10^7 M_\odot)^{-\beta}$. The luminosity density we infer from the measured M82 flux would then be $L_{\text{tde}} \int (dn/dM)(M/3 \times 10^7 M_\odot)^{-\beta}$, where L_{tde} is the UHECR luminosity from one burst. If we then use the best estimate $\beta \simeq 0.22$ from Ref. [51], the SMBH mass function from Ref. [98], and integrate from $10^5 M_\odot$ (below which there is little evidence for SMBHs) to $10^8 M_\odot$ (above which stars will be swallowed without being tidally disrupted [100]), we find—unfortunately for the TDE scenario—a luminosity density ~ 1.7 times higher. This

CHAPTER 2. TDES AND UHECR HOT SPOTS

power-law index β is, however, quite uncertain, and if we suppose that it is instead $\beta \simeq 0.5$, then the inferred luminosity density is decreased by ~ 0.5 . This may thus provide some wiggle room for the tension between the M82 and Cen A fluxes and the isotropic intensity, although is unlikely to be the entire explanation. Changes to the upper and lower limits of integration do not alter this conclusion. We do note that the masses of the SMBHs in Cen A and M82 are quite similar, both around $(3 - 5) \times 10^7 M_\odot$. If, for some reason, the TDE rate were to be maximized for SMBHs of this mass, and smaller for SMBHs of both lower and higher masses, then the universal UHECR luminosity could be reduced significantly relative to what we inferred above. In this case, the high fluxes toward M82 and Cen, relative to the isotropic intensity, would be a consequence of our chance proximity to two SMBHs of this specific mass.

The tension between the hot/warm-spot fluxes and the isotropic intensity may also be relaxed if UHECR consist at the source, at least in part, of other nuclei, like helium, carbon, nitrogen, or oxygen. The path length of such nuclei through the intergalactic medium is far smaller than the ~ 200 Mpc GZK distance of protons and iron nuclei [97]. If there is significant UHECR production in such nuclei, then the isotropic intensity inferred from the measured $D \lesssim 4$ Mpc luminosity density will be smaller. Such a scenario implies a different observed UHECR composition in the hot/warm spots and in the isotropic component. There may already be some evidence for intermediate-mass nuclei in UHECRs [101].

2.4 Discussion: TDE scorecard

The previous sections lead to the following conclusion: Energetics make it unlikely, although not impossible, that the hot spot toward M82 is the result of a single burst, a tension that is probably greater if UHECRs are protons rather than iron nuclei. Dispersion in galactic and intergalactic magnetic fields disperse the UHECR arrival times. This magnetic-dispersion time, if anything, has to be higher for protons than for iron nuclei. The single-burst scenario is also unappealing as it implies that the hot spot is evanescent, something that we see as a chance occurrence. This chance event is made even less likely if the warm spot toward Cen A is also explained another chance event.

The energetics requirements are relaxed, though, if the UHECRs in the hot spot result from a number of TDEs in M82 that have occurred over a magnetic dispersion time, a scenario in which the UHECR fluxes in the hot/warm spots are roughly in steady state. The required efficiency of UHECR production in each TDE event can then be reduced at the expense of an increased TDE rate. We do show, though, that the TDE rates can still remain low enough so that the time-averaged accretion rate in M82 remains sub-Eddington, something that may be desirable, though not necessarily required, to explain the quiescent nature of the SMBH in M82. (This is less of a concern, of course, for Cen A, which is quite active.) This latter, softer, requirement, is satisfied, though, only at the expense of introducing a slight tension in the required UHECR efficiency per TDE. That tension can be reduced if the TDE is highly beamed. Significant beaming introduces, however, the notion that the UHECR flux from M82 results from our chance position within the TDE's

CHAPTER 2. TDES AND UHECR HOT SPOTS

jet, an ingredient that is less appealing if we must also explain the PAO warm spot in terms of TDEs from Cen A’s SMBH. Any significant beaming requirement for Cen A would also be more difficult given that the radio observed jet in Cen A is not pointed toward us.

We note that the time between jetted TDEs in our scenario is a bit higher than the rate expected from existing TDE statistics. Scalings between TDE rates and SMBH masses derived in [51] suggest that the characteristic time between TDEs in a $3 \times 10^7 M_\odot$ SMBH is $\Gamma^{-1} \sim 10^4$ yrs. [52] estimate further that only a fraction $\zeta \sim 0.1$ of TDEs are jetted. If we take this value for M82, then the time between UHECR-producing events is roughly the same as the magnetic-dispersion time. There are, however, considerable uncertainties in these estimates, and there may also be considerable variation between the jetted fraction for one particular SMBH and the mean inferred by averaging over all SMBHs.

We then investigated the isotropic flux of UHECRs that is expected if the sources of UHECRs in M82 and Cen A are not atypical. This analysis applies not only to the hypothesis that the UHECR sources in M82 and Cen A are TDEs, but to any scenario in which there are hot/warm spots from Cen A and M82. The observed UHECR fluxes from M82 and Cen A imply a local UHECR luminosity density. We find that if the universal UHECR luminosity density is taken to be this local luminosity density, then the isotropic UHECR intensity is about 16 times larger than that observed. There is, however, some evidence that the local mass density in SMBHs is higher, perhaps by ~ 3 , than the universal density. Even so, there is still a tension, at the ~ 5 level, between the hot/warm spot fluxes and the isotropic intensity. Possible explanations for this residual tension may arise from our underestimate of the local overdensity; small-number statistics in the number of

CHAPTER 2. TDES AND UHECR HOT SPOTS

SMBHs; uncertainties in the characterization of the hot/warm spots; a mixed composition of UHECRs including intermediate-mass nuclei with smaller GZK cutoffs; and/or some SMBH-mass dependence of the TDE rate.

Before closing, it is interesting to wonder whether the $\text{SMBH} \sim 4 \times 10^6 M_\odot$ SMBH at the centre of Milky Way should produce UHECRs [102]. The answer is probably not. Assuming the Milky Way is a core galaxy, the expected time, from Ref. [51], between TDEs for the Milky Way’s SMBH is 3.9×10^4 yrs. As discussed above, the magnetic-dispersion time within the Milky Way can be, for reasonable magnetic-field parameters, quite a bit smaller than this. It is thus not surprising that we do not see an UHECR hot spot toward the Galactic centre, even if our SMBH does produce TDEs at the expected rate.

Finally, we speculate on the possibility that the IMBH in M82 (should the evidence for that IMBH survive) may have something to do with the TA hot spot [103,104]. It may be possible for IMBHs to produce their own TDEs. Another possibility is that IMBHs might perturb the orbits of stars in a way similar to the Kozai mechanism, and thus increase the rate of TDEs in the host galaxy [105]. The difference in the UHECR flux from M82 and Cen A might thus be explained by an IMBH-enhanced TDE rate in M82 relative to what it would be otherwise.

2.5 Conclusions

We have investigated the possibility that tidal disruption events fuelled by the accretion of stars onto the SMBH in M82 could account for the hot spot reported by the Telescope

CHAPTER 2. TDES AND UHECR HOT SPOTS

Array and that TDEs onto the SMBH in Cen A could explain the warm spot seen by the Pierre Auger Observatory toward Cen A. Given the measurement uncertainties and considerable astrophysical uncertainties, it is difficult to make precise statements about the viability of the scenario. Although there are some tensions at the order-of-magnitude level, outlined in detail above, there is, as far as we can tell, no silver bullet that rules the scenario out at the level of more than an order of magnitude.

Future measurements should help shed additional light on the viability of TDEs as the sources of UHECRs. The viability of the TDE scenario for the isotropic flux has been discussed in Refs. [84] and [52], but if the hot/warm spots are real and attributed to M82 and Cen A, then there are additional challenges discussed above. It will be interesting to see if the evidence for the hot and warm spots continues with more data (or perhaps gains additional support from independent measurements, such as ultra-high-energy-neutrino detection). If so, the characterization of those fluxes should improve. For example, there may be differences in the energy distribution of UHECRs in the hot/warm spots, that come from 3.8 Mpc, versus those in the rest of the sky, which come from much greater distances and thus experience greater photo-pion absorption.

Chapter 3

Deconfusing intensity maps with neural networks

A significant experimental effort is underway to study the high-redshift universe with line intensity mapping (LIM). LIM experiments probe galaxy evolution and large-scale structure without resolving individual emitting sources. Instead, these surveys map the aggregate emission of a single spectral line over cosmological scales see [53] for a review. Because the target emission comes from narrow spectral features, one can observe at many closely-spaced frequency bands to map the distribution of emitters in three dimensions. Intensity maps can therefore access a large number of spatial modes for large-scale structure measurement, and can study the statistical properties of large numbers of galaxies which are too faint to detect individually.

This great potential science output has spurred the creation of LIM surveys targeting a

CHAPTER 3. LIM WITH NEURAL NETWORKS

number of different spectral lines. The first line targeted was the 21 cm spin-flip transition in neutral hydrogen, which has been long known as a powerful probe of large-scale structure and reionization [106] and references therein. The 21 cm intensity mapping signal has been detected in cross-correlation by a pair of surveys [107–109], and a number of other surveys have been completed or are in progress across a wide swath of cosmic history [110–116]. Recently, though, there has been a surge of interest in using other lines for intensity mapping. Different lines trace different processes and different phases in the interstellar- and intergalactic media, and also have different experimental systematics. There are tentative detections of intensity maps of Lyman- α [117], C $_{\text{II}}$ [118, 119], and CO(1-0) [120], and experiments are underway or proposed to make definitive measurements of these and other lines [54, 121–130].

With this degree of experimental investment, it is important to develop the necessary theory and analysis tools to interpret the results of these surveys. Several challenges remain with this task. Line intensities are determined by complex and highly nonlinear gas physics which can only be captured by quite sophisticated models see, e.g. [131]. As a result of this complexity, many works focus on constraining intermediate statistical properties of the target galaxies, typically either a relationship between halo mass and line luminosity [54] or a line luminosity function [132].

This goal is made more difficult by the unresolved nature of intensity mapping data, as we must construct statistics which link the intensity field and the underlying galaxy distribution. For example, the power spectrum of a map can be used to determine the first two moments of the target luminosity function [133, 134]. Further detail can be obtained

CHAPTER 3. LIM WITH NEURAL NETWORKS

using, for example, the one-point statistics of a map [55,132]. However, these statistics may not suffice to extract all of the useful information from a confused, highly non-Gaussian intensity map, especially given that the target line is rarely the only or the most dominant source of emission. These statistics must be modified and lose additional information due to the near-guaranteed presence of foreground contamination, both from local Milky Way emission see, e.g. [135,136] and from extragalactic sources [137,138]. In light of the difficulty of measuring a luminosity function from a contaminated map, it may be useful to consider different analysis approaches. In this work, we will explore possibilities for applying machine learning methods to intensity maps.

In recent years, machine learning (ML) methods have shown to be very useful for a variety of applications in the field of cosmology¹, and will continue to contribute significant cosmological insights over the following decade and beyond [139]. The utility of machine learning methods emerges from their ability to find patterns in data, and, in many cases, to relate these patterns to higher-level information about samples from the data set. For example, when applying a neural network to solve the classic computer vision application of classifying handwritten digits, the network learns patterns in the spatial distribution of the two dimensional pixel intensities in order to predict the higher-level class (an integer between 0-9) of an individual digit sample drawn from the test set. Similarly, in cosmology, machine learning can be used on data from simulations, observations, or (possibly) a combination of the two to predict cosmological or astrophysical parameters [140–145], perform model discrimination [146,147], augment simulations and create synthetic data [148–154], identify

¹comprehensive list at <https://github.com/georgestein/ml-in-cosmology>

CHAPTER 3. LIM WITH NEURAL NETWORKS

structures and predict their properties [155–157], or to reconstruct initial conditions [158], among many other applications.

Convolutional neural networks (CNNs) are a common class of deep learning first proposed in [159, 160] and popularized by the state-of-the-art classification results of [161]. CNNs are best designed to process data that come in the form of multiple arrays; the most common example being the three colour channels, or RGB pixel arrays, of two dimensional images, and they have had success in a wide variety of detection, segmentation, and recognition applications. A CNN transforms from an input N -dimensional array to e.g. a prediction of which class the array belongs to. Convolutional layers consist of a number of filters, each containing a set of trainable weights (determined through backpropagation [162]) which are applied to a series of local patches of the previous layer. This allows the network to detect local features in the previous layer, and the network can learn higher-level information in each succeeding level.

CNNs are therefore particularly suited to problems in cosmology that require environmental multi-scale information to solve. For example, it is well known that the large-scale structure of the universe is defined by the network of clusters (small), filaments (elongated), and voids (large), of the cosmic web [163], each with differing physical scales. One may then hope that if, for example, the observable signal from clusters is related to the surrounding environment: the first levels of a CNN will extract features relevant to the scale of a cluster, following levels will focus on features relevant to broader cluster environments, succeeding levels will add features related to the large-scale distribution of matter in the universe, and this multi-scale information will be combined in the final levels to make a prediction

CHAPTER 3. LIM WITH NEURAL NETWORKS

(see [164] for investigations into which input stimuli excite individual feature maps at any layer in a model).

Although powerful in theory, many observational cosmological applications of supervised machine learning still have obstacles to overcome before becoming competitive with alternative methods. Astronomy is a field of observation, and contains little to no possibility of experimentation. Additionally, the exact amplitude, extent, and spectral evolution of many of the cosmic signals that we are attempting to detect in fields such as intensity mapping are presently unknown, and labeled observational data sets are in many cases theoretically difficult or impossible to acquire. The field has therefore been focused more on studies performed on synthetic data to determine the general viability of machine learning methods to extract cosmic signals.

The use of synthetic data is not uncommon in machine learning applications [165, 166], but is generally used to augment small existing data sets and is followed by additional training on the true labeled data. Currently this is not possible for many observational cosmology applications, so we must hope that: a) the synthetic data perfectly reproduces reality, and that by training on synthetic observations and using the network to predict on a true observation of our universe therefore produces no biases or uncertainties (unlikely), b) the network is sufficiently robust to any differences between the synthetic and real data (e.g. unaccounted for instrument errors, unknown foreground contamination, etc.), and any biases and uncertainties are well understood, or c) labelled training data from cosmological measurements becomes plentiful enough to rely on, and machine learned methods outperform traditional ones. In this work we rely purely on synthetic data, and focus on scenario

CHAPTER 3. LIM WITH NEURAL NETWORKS

b). By first studying the ideal case of perfectly known cosmic signal and instrument noise, and then extending to add unknown foregrounds and noise to mock up a real observation, we can shed light on the true ability of a network trained on synthetic data to measure cosmic signals.

This work is not the first attempt train CNNs on simulated intensity maps. Previous works primarily study maps of the 21 cm spin-flip transition in neutral hydrogen [167–170]. Many of these works focus on the Epoch of Reionization (EoR), where the signal is dominated by emission from the intergalactic medium which is gradually becoming ionized by emission from the first galaxies. In this work, we consider a different regime, where line emission primarily comes from within individual galaxies. In this case, individual sources are typically small compared to instrument resolution, so there is a well-defined line luminosity function that we can seek to constrain. We focus on CO intensity mapping as opposed to HI, which gives insight into the molecular phase of the high-redshift ISM. We seek to be as model-agnostic as possible in our predictions by forecasting constraints on the value of the luminosity function in different bins rather than constraining a specific parameterized model.

For our fiducial survey, we consider a map of the CO(1-0) line at redshift $z \sim 3$ made by the CO Mapping Array Pathfinder (COMAP) experiment [54], currently taking data at the Owens Valley Radio Observatory. The CO luminosity function probes the abundance of molecular gas in high-redshift galaxies. As stars form from molecular gas, the CO luminosity is an important probe of the broader galactic ecosystem see reviews by, e.g. [171–173]. As stated previously though, our ML methods will be directly relevant to any line which is

CHAPTER 3. LIM WITH NEURAL NETWORKS

emitted by a population of discrete sources.

We demonstrate that for our fiducial model the neural network we create can recover the luminosity function from a CO intensity map with accuracy comparable to that of conventional methods. The accuracy only degrades slightly when contamination is introduced from instrument noise and uncleaned foregrounds. However, when testing on models on the fringes of our training space, or on models which were not trained at all, we find that the network sometimes outputs substantially inaccurate results. These findings demonstrate that, while machine learning methods have great potential for this type of data analysis, care must be taken when using synthetic data to analyze real observations.

This chapter is organized as follows. In Section 3.1, we describe how we generate our data and training set. In Section 3.2, we describe the CNN that we will train. In Section 3.3, we test the accuracy of our CNN on different scenarios for underlying LIM, noise and foregrounds. In Section 3.4, we discuss the strengths and weaknesses of our CNN. We conclude in Section 3.5. Throughout this work we assume a cosmology consistent with [174] with $\Omega_m = 0.286$, $\Omega_\Lambda = 0.714$, $\Omega_b = 0.047$, $h = 0.7$, $\sigma_8 = 0.82$, and $n_s = 0.96$.

This chapter is based heavily on work in [42] with coauthors Patrick C. Breysse and George Stein.

3.1 Simulated Maps

Very little actual CO intensity mapping data currently exists, so as stated above we have to resort to synthetic data to train our neural network. For this purpose, we use a set of simulated CO line intensity observations constructed by coupling the $L_{\text{CO}}(M_{\text{halo}})$ model of [54] to dark matter halo catalogues created using the Peak Patch method [175]. Our goal is to train a neural network that can take one of these simulated maps as input and output a list of galaxy abundances at given CO luminosities. In addition to the intrinsic CO signal we add various noise sources to our maps, including the thermal white noise expected from the COMAP experiment, possible point source foregrounds with continuum spectra, and ‘geometric’ noise from crude approximations of typical instrumental scan strategies. Our simulations are not intended to fully reproduce the range of possible signals and noise in a real CO experiment. Rather they are meant to explore how a CNN-based analysis might perform in a variety of conditions.

Table 3.1 lists the experimental parameters we use for our mock LIMs. We represent our generated LIMs as three dimensional arrays of size $64 \times 64 \times 10$. Each element records the total intensity measured at that location in the map. The first two dimensions are spatial dimensions on the sky representing a $1.5^\circ \times 1.5^\circ$ survey field, while the third dimension carries the spectral information. Although COMAP is designed with 512 frequency channels, we intentionally degrade the frequency resolution of our mocks down to 10 channels due to memory considerations. The 64×64 maps oversample the COMAP beam somewhat, so we can add in the effects of COMAP beam smoothing by convolving each slice of our maps with

CHAPTER 3. LIM WITH NEURAL NETWORKS

Parameter	Value
Beam FWHM (armin)	4
Frequency Band (GHz)	26-34
Redshift coverage	2.4-3.4
Channel width (MHz)	15.6
Noise per 16 arcmin ² voxel (μ K)	11
Field size (deg ²)	2.25

Table 3.1: Experiment setup for COMAP Phase one.

a 4' Gaussian filter. For a given spectral line, the observed frequency directly determines the emission redshift, so the third dimension in our maps represents the redshift (or distance, given a cosmological model) of CO emitters along the line of sight. In all of the following, a “voxel” refers to a single element in a three-dimensional map, and a “pixel” refers to all of the voxels along a line of sight when the first two dimensions (position on the sky) are kept constant.

3.1.1 Dark Matter Simulations

We generated the large ensemble of dark matter halo catalogues required to train our CNN using the Peak Patch method, a fully predictive initial-space algorithm to quickly generate dark matter halo catalogues in large cosmological volumes [175].

To cover the full redshift range of the COMAP experiment ($z = 2.4 - 3.4$), with no repetition of structure, the simulation box size was $(1140 \text{ Mpc})^3$ (comoving) and used a cubic lattice of 4096^3 particles. This achieves a minimum halo mass of $2.5 \times 10^{10} M_\odot$ [$M_{200,M}$], comparable to values typically assumed for the minimum mass of a CO-emitting halo [54, 133], and when projected onto the sky results in a $9.6^\circ \times 9.6^\circ$ field. We then separate

CHAPTER 3. LIM WITH NEURAL NETWORKS

the $9.6^\circ \times 9.6^\circ$ area into multiple $1.5^\circ \times 1.5^\circ$ patches to match the size of a COMAP field. Each $1.5^\circ \times 1.5^\circ$ patch we use does not overlap with any other to minimize nonphysical correlations in our training data.

The efficiency of the Peak Patch method allowed for 161 independent full-size realizations in 82,000 CPU hours. The resulting halo catalogues contain roughly 54 million halos, each with a position, a velocity, and a mass. Peak Patch has the ability to simulate continuous light-cones on-the-fly, so stitching snapshots together was not required to create the light-cone. The dark matter halo catalogues were additionally mass corrected by abundance matching along the light-cone to [176].

3.1.2 CO Modelling

The peak-patch simulations described above give us a map of dark matter halos, which we can turn into a CO intensity map by assuming a CO luminosity-halo mass relation. For this purpose, we adopt the model of [54] which we briefly summarize here.

The model is defined by empirical parametric relations between the halo mass M_{halo} , star formation rate (SFR), infrared (IR) luminosity L_{IR} , and the CO luminosity L_{CO} , in the following chain:

$$M_{\text{halo}} \xrightarrow{\text{A}} \text{SFR} \xrightarrow{\text{B}} L_{\text{IR}} \xrightarrow{\text{C}} L_{\text{CO}}.$$

A: The star formation rate of a given dark matter halo is obtained by using the results of [177, 178], which empirically quantified the average stellar mass history of dark matter halos as a function of halo mass and redshift. A log-normal scatter of σ_{SFR} is

CHAPTER 3. LIM WITH NEURAL NETWORKS

added to describe the scatter about the mean value.

B: IR luminosities are given through the relation

$$SFR = \delta_{MF} \times 10^{-10} L_{IR}, \quad (3.1)$$

where the SFR is in units of $M_{\odot} \text{ yr}^{-1}$ and L_{IR} is in units of L_{\odot} .

C: CO luminosities are obtained from the total infrared luminosity, assuming a power-law relation of the form

$$\log L_{IR} = \alpha \log L'_{CO} + \beta, \quad (3.2)$$

where L'_{CO} is in units of K km s^{-1} , which we then convert in our final maps to brightness temperature in μK . A second log-normal scatter of σ_{CO} is also added to describe the scatter about this mean value.

This model therefore contains five free parameters: three parameterizing the mean relations $\{\delta_{MF}, \alpha, \beta\}$ and two parameters describing the scatter about the mean, $\{\sigma_{SFR}, \sigma_{LCO}\}$. In this work, we vary all five parameters about their fiducial values in the training step [54]. We do not train our CNN to predict these model parameters as one may do with a Markov Chain Monte Carlo (MCMC) or similiar analysis. Our CNN is trained to relate LIMs to luminosity functions independent of model.

We want to train our network with maps simulated from a variety of different CO-halo connections, which we can accomplish by generating training data using different parameter values. We will refer to models generated with the fiducial [54] parameters ‘fiducial Li’ maps

CHAPTER 3. LIM WITH NEURAL NETWORKS

and maps generated with random parameters ‘random Li’ maps. Here ‘Li’ refers to the first author in Ref. [54]. We take as “priors” on these parameters 10% of the priors quoted in [54].

We used the publicly available `limlam_mockers`² package for line intensity mocks to create the COMAP intensity mocks and corresponding luminosity functions from the 161 halo catalogues, resulting in 5796 possible independent $1.5^\circ \times 1.5^\circ$ COMAP mocks for each choice of parameters/noise/foregrounds. Figure 3.1 shows range of luminosity functions generated for training purposes. As the luminosity increases, the variance of the luminosity increases as well.

3.1.3 Noise and Foregrounds

²https://github.com/georgestein/limlam_mockers

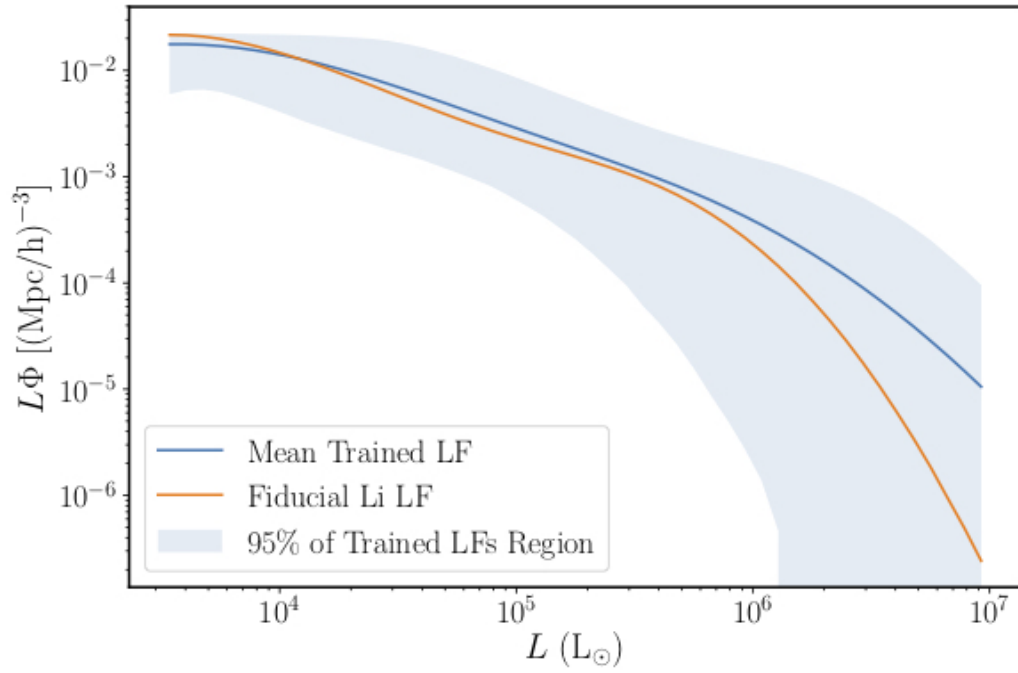


Figure 3.1: Range of luminosity function values used while training. The shaded region is the range where 95% of luminosity function values of a given luminosity fell. The orange curve shows the 'Fiducial Li' luminosity function and is different than the mean luminosity function used in training. Note that the 'Fiducial Li' curve is within 95% region of trained luminosity functions.

	Model Type	Summary	Used for Training
CO Signal	Fiducial Li	[54] CO-halo mass model with fiducial parameter values	No
	Random Li	[54] model with randomly chosen parameter values	Yes
	Padmanabhan	[179] CO-halo mass model with fiducial parameter values	No
	Less Bright Sources	Random Li maps chosen to contain < 500 sources with $L \leq 10^6 L_{\odot}$	Yes ¹
Instrument Noise	No noise	No added noise. Hypothetical sample-variance dominated measurement	Yes
	Fiducial Noise	Thermal white noise with fiducial COMAP amplitude	No
	Random Noise	Thermal white noise with amplitude drawn uniformly from $[0, 7.98]$	Yes
	Geometric Noise	Added white noise to map edge with amplitude following Eq. (3.4)	No
Foregrounds	No Foregrounds	No added foregrounds, simulates perfect foreground cleaning	Yes
	Fiducial Foregrounds	Point-source emitters drawn following [180] data	No
	Random Foregrounds	[180] with random parameters	Yes

¹ ‘Less Bright Sources’ maps are a subset of the ‘Random Li’ mocks, so they appear naturally in the training data.

Table 3.2: Summary of signal, noise, and foreground models used for training and testing.

CHAPTER 3. LIM WITH NEURAL NETWORKS

To explore how our network might perform in a true analysis we must include instrumental noise and foregrounds in our simulations. In this study we use relatively simple models for both of these effects, considering only thermal instrumental noise and point-source extragalactic foregrounds.

Thermal noise can be modeled by adding an independent Gaussian random number with zero mean and a variance of σ_{wn}^2 to each voxel of a LIM. In the case of COMAP Phase 1 the noise is expected to be $\sigma_{wn} \simeq 11 \mu\text{K}$ [54] in a $4'$ voxel for a map with 512 frequency channels. To scale this noise to different voxel sizes we make use of

$$\sigma_{wn} \propto \frac{1}{\delta\theta\sqrt{\delta v}}. \quad (3.3)$$

We find that, in order to match the COMAP noise properties, our voxels need to have $\sigma_{wn} \approx 4.39 \mu\text{K}$. As the noise properties of a given survey may not be precisely known *a priori*, we will split our mocks between those with ‘fiducial noise’, i.e. those with the above COMAP noise model, and those with ‘random noise’, in which we assume a different noise amplitude σ_{wn} . In either case, a given mock will have a random realization of the given noise model.

A uniform white noise is the only noise source in the ideal case, but in practice many observations include additional, sometimes unknown, sources. One example comes from the scan strategy of the telescope which in general results in different integration times on different pixels, with the central region of the survey generally having a longer integration and therefore a lower noise level. Later when testing our network, we will also include a

CHAPTER 3. LIM WITH NEURAL NETWORKS

model of this type of ‘geometric’ noise, where pixels within 5% of the edge of the survey area have an additional white noise contribution given by

$$\sigma_{\text{geo}} = \sigma_{\text{geo,max}} \frac{\max(d_{\text{max}} - d, 0)}{d_{\text{max}}}. \quad (3.4)$$

In this simple model, $\sigma_{\text{geo,max}}$ is the maximum amount of geometric noise we should add at the absolute edge, d is the shortest distance from the edge of the LIM to a given pixel as a fraction of the the length of the LIM. We cut off the added noise at a distance $d_{\text{max}} = 0.05$. For our tests we somewhat arbitrarily $\sigma_{\text{geo,max}} = 100 \mu\text{K}$. We leave detailed modeling of specific scan strategies to future work.

Our simulated intensity maps also include radio point sources as possible foregrounds, modeled following [181]. We assume the differential source count per unit area per flux is described by the power law,

$$\frac{dN}{dS} = N_0 \left(\frac{S}{1 \text{ mJy}} \right)^{-\gamma}, \quad (3.5)$$

where N_0 is a normalization parameter per unit area and flux, S is the source flux, and γ is the power-law index [180]. The range of the parameters in this foreground model were found to be $N_0 = 32.1 \pm 3.0 \text{ deg}^{-2} \text{ mJy}^{-1}$ and $\gamma = 2.18 \pm 0.12$ for frequencies around 30 GHz.

As we assume our foregrounds are continuum emitters, we assign them pixel-by-pixel rather than voxel-by-voxel. As with our signal and noise models, we can choose to draw either ‘fiducial foregrounds’ where we assume best fit parameter values from the above foreground models, or ‘random foregrounds’, where we randomly assign parameter values

CHAPTER 3. LIM WITH NEURAL NETWORKS

before generating a realization. In each pixel, we Poisson draw the number of sources based on the expected sources per square degree (thus neglecting large-scale structure correlations in our foregrounds). We then randomly assign each source an overall with probability set by Eq. (3.5) and a spectral index drawn from the distributions plotted in Figure 3 of [180]. We can then use this slope and normalization to compute the contribution of the source to each of our frequency channels.

This is a somewhat simplistic and optimistic model of foreground contamination, as it does not include Galactic emission and ignores emission from point sources below the detection threshold of [180]. However it does capture the essential features necessary for our purposes, in that it results in a map of bright, continuum emission which does not correlate with the large-scale structure of our CO signal. As with the instrument noise, we leave a detailed exploration of foreground emission to future work.

Both the white-noise and foreground additions to the LIMs are randomly generated each time an LIM is used for training although there is a 10% and 50% chance that no noise or foregrounds respectively are generated when training on a given map. The same is true of geometric noise, but it is only used for testing purposes after training. We ensure these additions are not static objects in order to help prevent overfitting and give the network more unique LIMs to use for training. The reason to train some maps without noise and foregrounds is to make the network more robust and handle situations in which they might not be an issue. Conventional techniques exist for removing foregrounds and a future survey may be sample-variance dominated so we believe it is valid to train our network for such scenarios.

CHAPTER 3. LIM WITH NEURAL NETWORKS

In the above we have described several different choices we can make when modeling the signal and noise in our maps. For the convenience of the reader we summarize these options in Table 3.1.3. Unless specified, a given map is assumed to use ‘random noise’ and ‘random foregrounds’ models.

In summary, to construct a single CO realization, we:

- Generate a dark matter halo catalogues 3.1.1
- Apply a CO-halo mass model, to paint CO luminosities onto halos (Sec. 3.1.2).
- Use the CO luminosities to produce clean CO LIMs as well as record the true underlying luminosity function (Sec. 3.1.2).
- Generate noise and foreground realization and add to map (Sec. 3.1.3).
- Apply Gaussian smoothing of $4'$ beam to map to match COMAP beam size.

When training, we use the ‘Random Li’, ‘Random Noise’, and ‘Random Foreground’ models from Table 3.1.3. The first three steps are done before training as it would take too long to generate new LIMs from scratch each time one was needed. Noise, foregrounds, and beam smoothing are added during training each time a LIM is looked at.

Sample slices of our mock LIMs can be seen in Figure 3.2. We show a ‘Fiducial Li’ LIM as well as maps for white noise, foregrounds, and the sum of all three components. Both the foregrounds and features of the original random Li LIM are visible in the combined LIM. For clarity, we also show a realization of the Geometric Noise that we will use for later tests, as well as a version of the combined signal/noise/foreground map before beam smoothing.

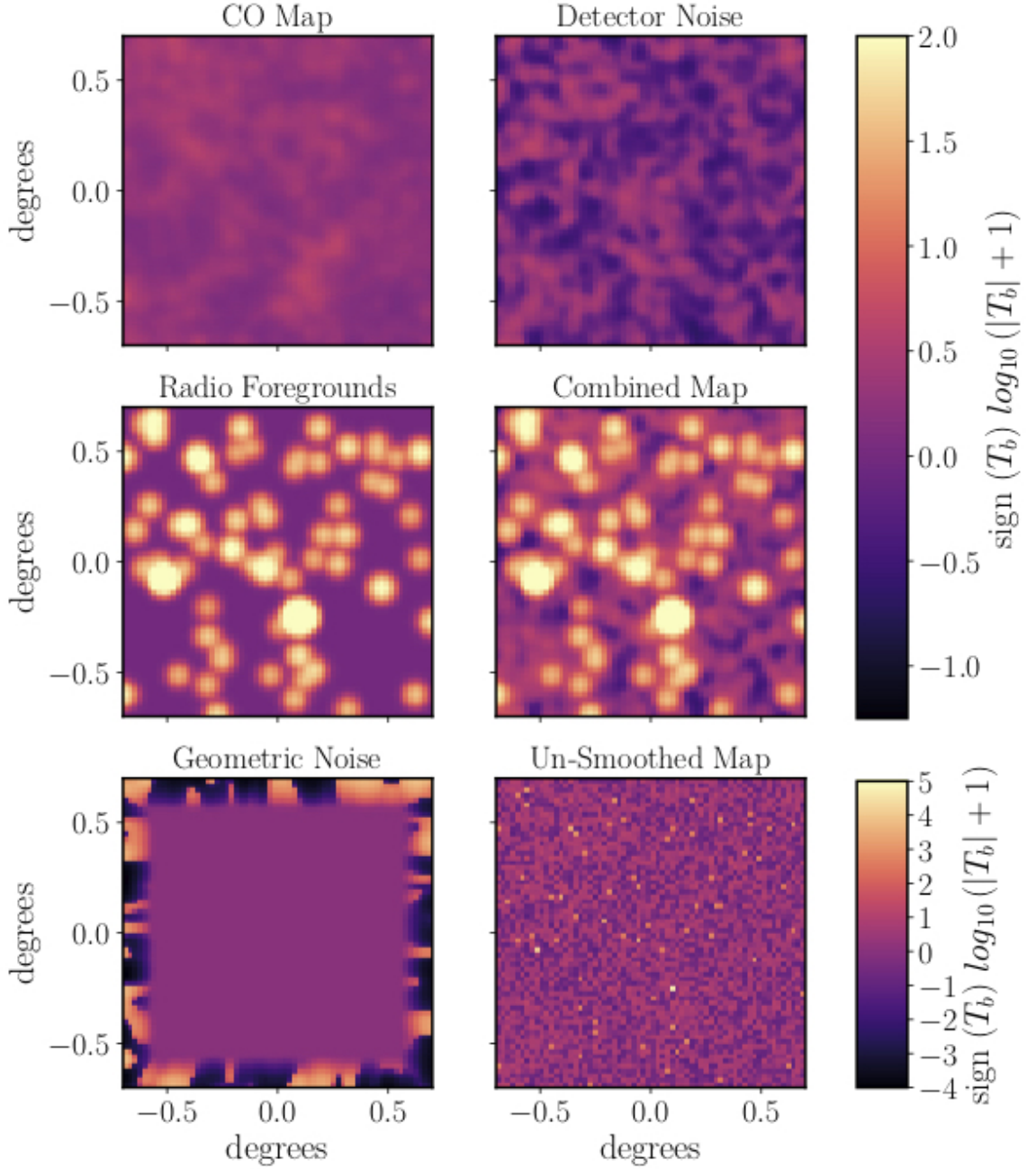


Figure 3.2: Single slices of different components of our LIMs. All of the maps have had the log-modulus applied to their intensities (see Eq. 3.6). *Top Left:* ‘Fiducial Li’ LIM. *Top right:* ‘Fiducial Noise’-only realization. *Middle left:* Point source foregrounds from ‘Fiducial Foregrounds’ model. *Middle right:* Sum of previous signal, noise, and foreground maps. *Bottom left:* ‘Geometric Noise’ realization. *Bottom right:* Signal+noise+foreground map before beam smoothing. Note the difference in the color scales between the top two rows and the bottom row.

3.2 Convolutional Neural Network

The goal of our CNN is to take any LIM as input, and output values of the underlying luminosity function. Due to GPU-memory and training-speed constraints we use $64 \times 64 \times 10$ maps. By using less frequency channels than COMAP is capable of, we can make a larger CNN, train with larger batch sizes and train faster. Our forecasts will thus underestimate the constraining power of a network which could handle the full $64 \times 64 \times 512$ COMAP data cube.

CNNs are fast NNs designed for classification and regression on images, looking for patterns in a translationally invariant fashion. Normal images contain two spatial dimensions and a third which stores the intensity of different colors of light (usually three for RGB images). LIMs behave similarly, albeit with many more spectral channels. However, a key general advantage of LIMs is that, neglecting noise and foregrounds, the spectral information can be converted directly into a line-of-sight distance. CNNs typically convolve images in two dimensions, but we can modify this approach to use 3D convolutions and easily make use of the added tomographic information. This one change allows us to make use of the standard framework of CNNs for three-dimensional LIMs.

After testing a number of CNN architectures we choose a residual learning framework first proposed in [182] for our network architecture. Each layer in these networks (commonly abbreviated as *ResNets*) learns the residual mapping with reference to its inputs instead of directly learning the underlying mapping. This has been shown to improve the training of deep networks with negligible memory or speed tradeoffs. The form of Resnet that we

CHAPTER 3. LIM WITH NEURAL NETWORKS

used is a modification of the 50-layer network from [182]. We first changed the reduced the size of the initial convolution to prevent losing small scale structure too quickly, added an extra residual block in each layer to increase the learning ability of the network without significantly increasing the memory requirement and removed the fourth and fifth layers of the network. Furthermore we modified the end of the network to match our required output. As mentioned previously, we have also modified the architecture to use three-dimensional convolutions.

This architecture was not designed for this specific problem so we do not believe that it is truly the most optimal possible CNN. A detailed architecture optimization is beyond the scope of this work, but as ResNets are very common in recent cosmological applications of CNNs we expect the relative results shown here to be representative. For example, we would expect the decrease in accuracy of prediction when considering noise/foregrounds beyond the fiducial case to hold for more general network designs.

3.2.1 Network Architecture

Here we summarize the modified [182] network we use for this work. A basic tenet of machine learning is that bigger networks allow one to learn more (i.e. learn a more complicated model or learn a less complicated model better). However, there are exceptions to this rule. Adding more layers to a network can lead to degradations of the data flowing through the network and the gradients needed for back propagation, decreasing the accuracy of a CNN. To get around this, one can make use of a Resnet. At the heart of the Resnet is the residual block. A residual block consists of multiple convolutional layers and a shortcut

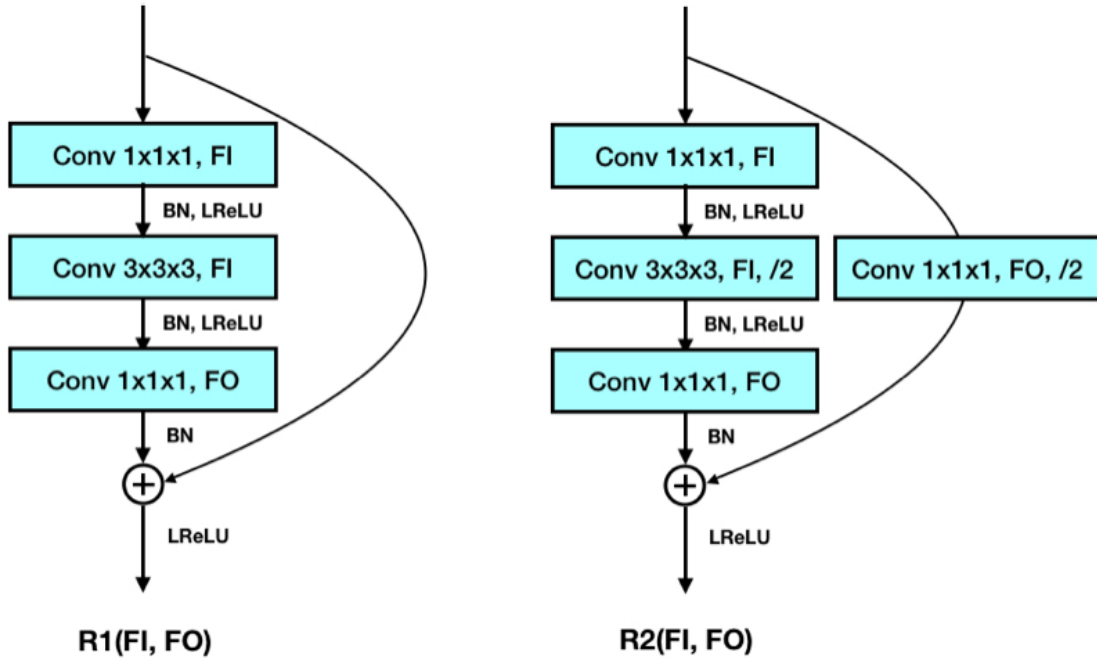


Figure 3.3: Basic residual block structures used. The teal blocks are used to denote convolutional layers. Both blocks use a bottleneck design of a 1x1x1 convolution followed by a 3x3x3 convolution and ending with a 1x1x1 convolution of varying filter size. They also include a shortcut which directly adds the input data to the output of the three convolutions in the bottleneck. See text in Section 3.2.1 for more details.

CHAPTER 3. LIM WITH NEURAL NETWORKS

that connects the input directly to the output. Adding a shortcut helps prevent degradation of network performance because it allows the residual block to function as a small change on top of an identity mapping between input and output. This means no residual block should give worse results than a previous layer of the network, an issue which large networks without residual blocks face.

After most convolutions, we make use of batch normalization (BN) before applying the leaky rectified linear unit (LReLU) activation function [183]. BN helps prevent vanishing and exploding gradients by normalizing the output of a convolution for a given batch of data [184]. Zero padding is used throughout to obtain the required output dimensionality. Multiple convolutions are grouped together to form residual blocks. Our residual blocks make use of a bottleneck design. The bottleneck replaces two $3 \times 3 \times 3$ convolutions with three layers of two $1 \times 1 \times 1$ and one $3 \times 3 \times 3$ convolutions. The $1 \times 1 \times 1$ convolutions in the bottleneck are responsible for reducing and increasing dimensionality. Bottleneck designs are used to decrease computational time while retaining network performance.

In our network we use two different types of residual blocks which can be seen in Figure 3.3. Both blocks depend on two parameters: filters-in (FI) and filters-out (FO). FI and FO are the number of filters the convolutions use at the beginning and the number of filters the output should have, respectively. The first residual block on the left, $R1(FI, FO)$, takes input of any size and number of channels. It then uses a $1 \times 1 \times 1$ convolution to change the number of filters to FI and is followed by BN and a LReLU. Next we use a $3 \times 3 \times 3$ convolution with FI channels followed by another BN and a LReLU. The third convolution is a $1 \times 1 \times 1$ convolution that changes the number of filters to FO and is followed by BN. We then make

CHAPTER 3. LIM WITH NEURAL NETWORKS

use of the shortcut and take the original input and add it directly to the output of the third convolution. We employ an ‘identity shortcut’, named so as we do not modify the input data when using it in the shortcut. A final LReLU is applied before sending the data to the next layer. The second residual block is similar, but it changes the dimensionality of the data midway through. The second convolution in this block uses a stride of $2 \times 2 \times 2$ (denoted by $/2$ in the diagram) to lower the dimensionality. As we changed the shape of the data midway through the block, the shortcut is no longer an identity shortcut. We apply a $1 \times 1 \times 1$ convolution with stride $2 \times 2 \times 2$ and FO filters to the shortcut to ensure it matches the output of the rest of the block.

We define an $R1 \times N$ block as N $R1$ blocks in a row as seen in Figure 3.4. With our residual blocks in place, we can now build our full network. Figure 3.5 displays the full network that accepts a $64 \times 64 \times 10$ LIM and outputs 49 values of the luminosity function. The network starts with a $3 \times 3 \times 3$ convolution with 64 filters and a stride of $2 \times 2 \times 2$ to reduce the dimensionality by 2. As usual, we follow the convolution layer with BN and a LReLU. We then follow up with a 3D max pool with kernel $3 \times 3 \times 3$ and stride of $2 \times 2 \times 2$. A max pool layer takes the maximum value within the kernel as output as opposed to a convolution which is effectively the weighted average of the input. This pool reduces the dimensionality of the data by 2 because of the $2 \times 2 \times 2$ stride. After the pool, we apply three $R1$ blocks. We then apply an $R2$ block followed by four $R1$ blocks. The $R2$ block reduces dimensionality while the $R1$ blocks increase the depth of the network. Following the final set of $R1$ blocks, the data is in the form of a $2 \times 2 \times 1$ map with 2048 filters. On these objects we apply a 3D global average pool which takes the maximum value of the $2 \times 2 \times 1$ data for each channel and

CHAPTER 3. LIM WITH NEURAL NETWORKS

layer name	output size	layer features
conv1	32x32x5	3x3x3, 64 stride 2
conv2_x	16x16x3	3x3x3 max pool stride 2 $\begin{pmatrix} 1x1x1, 128 \\ 3x3x3, 128 \\ 1x1x1, 256 \end{pmatrix} \times 3$
conv3_x	8x8x2	$\begin{pmatrix} 1x1x1, 256 \\ 3x3x3, 256 \\ 1x1x1, 512 \end{pmatrix} \times 5$
global_pool	2048	7x7x7, global avg pool 3D
fc1	1000	1000 fully connected
fc2	49	49 fully connected

Table 3.3: Architecture for our Resnet. Building blocks, as seen in Figures 3.3 and 3.4, are shown in parentheses with the number of blocks stacked. Dimensionality reduction is performed by conv2.1 and conv3.1 by using a stride of 2 for the max pooling or convolution layers. The total number of training parameters in the network is $\sim 2.7 \times 10^6$.

returns a single value for each channel³ giving 1-dimensional data. Second to last, we use a fully connected layer with 1000 neurons which is followed with BN and a LReLU. Finally, we end with a fully connected layer of 49 neurons with a linear activation function. Each one of these neurons represents the value of the luminosity function at a specific luminosity. This architecture can be seen in Table 3.2.1.

3.2.2 Implementation

We have made a custom implementation of our Resnet in `Keras` using the `TensorFlow` backend [185,186]. We use the default $\alpha = 0.3$ for our LReLU's. To help with overfitting we apply a dropout rate of 50% to the second to last layer [187,188]. We obtained our best result when using the Adam optimizer [189]. We used a mean-squared-error loss function for training.

³channels for CNNs refer to the number of convolutional filters applied at the last convolutional layer

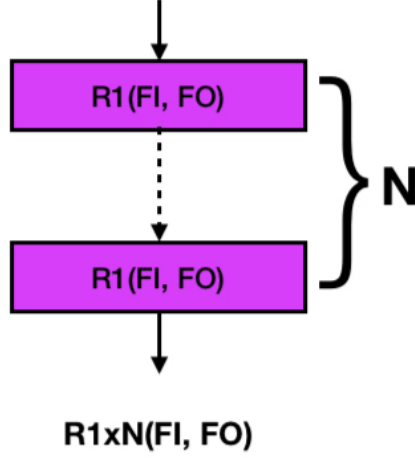


Figure 3.4: A series of N $R1$ blocks is defined as an $R1xN$ block. This structure appears multiple times in our Resnet. The purple blocks are used to denote $R1$ blocks.

As neural networks work better when data contained within them is similar in magnitude (this includes the input and the data passed between layers), we apply a log modulus function to the values in the intensity map given by

$$\hat{T} = \text{sign}(T) \log_{10} (|T| + 1), \quad (3.6)$$

where T is the intensity of a given voxel in brightness temperature units. The sign and absolute value of T allow us to handle voxels with negative intensity which can come about due to the added white noise. After transforming the size of the LIM and the intensities within each voxel, we feed the new LIMs into the CNN. The output of our network was chosen to be

$$\mathcal{L}(L) = \log_{10} (L\Phi) \quad (3.7)$$

at 49 values of L , where $\Phi = \frac{dn}{dL}$ is the number density of CO hosting galaxies with luminosity

CHAPTER 3. LIM WITH NEURAL NETWORKS

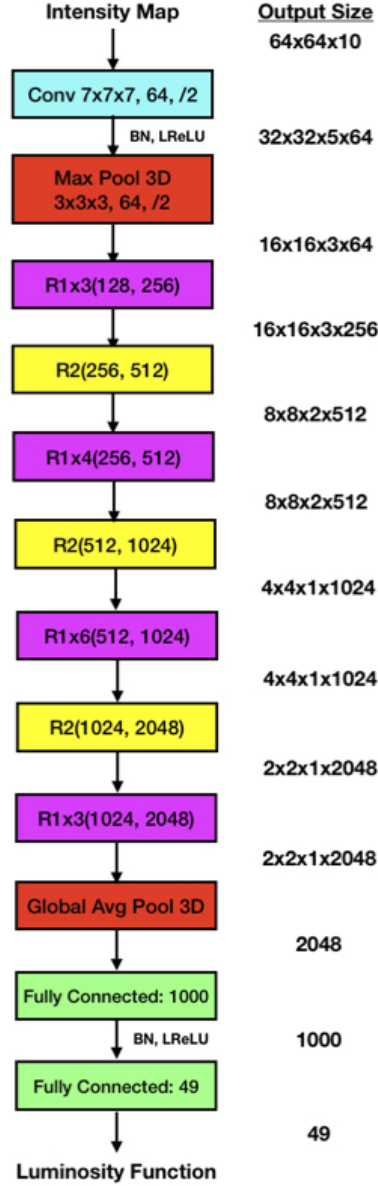


Figure 3.5: A diagram of our full network. A 64x64x10 intensity map is converted to 49 different luminosity function values through the use of many convolution layers, two pooling layers and two fully connected layers. Here, the teal blocks represent convolutional layers, the purple represent R1 blocks, the red show pooling layers, the yellow show R2 blocks and green show fully connected layers.

CHAPTER 3. LIM WITH NEURAL NETWORKS

between L and $L + dL$. Returning $\log_{10}(L\Phi)$ gives an output that only spans an order of magnitude. It should be noted that the CNN itself does not know that it is measuring a luminosity function at specific values, only that it is returning 49 ordered numbers. We consider luminosity bins logarithmically spaced between $10^{3.5}$ and $10^7 L_{\odot}$.

For training and testing our model we start with 5796 ‘Random Li’ LIMs, generated as described in Sec. 3.1. The LIMs were split into training and validation data with 80% of the maps being used for training and 20% used as validation to test our results. Separating the training and validation data at this point means the network cannot benefit from simply learning the underlying peak-patch halo catalogues. As noise and foregrounds may be modeled imperfectly in a real observation, we made the conservative choice to use ‘Random Noise’ and ‘Random Foreground’ contamination models. At each step, one of the training signal maps is combined with noise and foregrounds generated with random parameter values. This allows us to turn our few thousand signal maps into order a million training realizations. We also make sure to train on noiseless LIMs 10% of the time and foregroundless LIMs 50% of the time to make sure the trained CNN learns to interpret clean LIMs. While training the network it was learned that training on LIMs without foreground only 10% of the time led to significant biases when testing on maps without foregrounds after training.

We trained with batch sizes of 40 LIMs, set by the GPU capacity, and the somewhat arbitrary choice of 150 batches to an epoch for 200 epochs. We employed 4 Nvidia K80 GPUs with 24 GB each. The training history of the final CNN is shown in Figure 3.6. We find that the network does most of its learning within a few epochs. Learning then slows

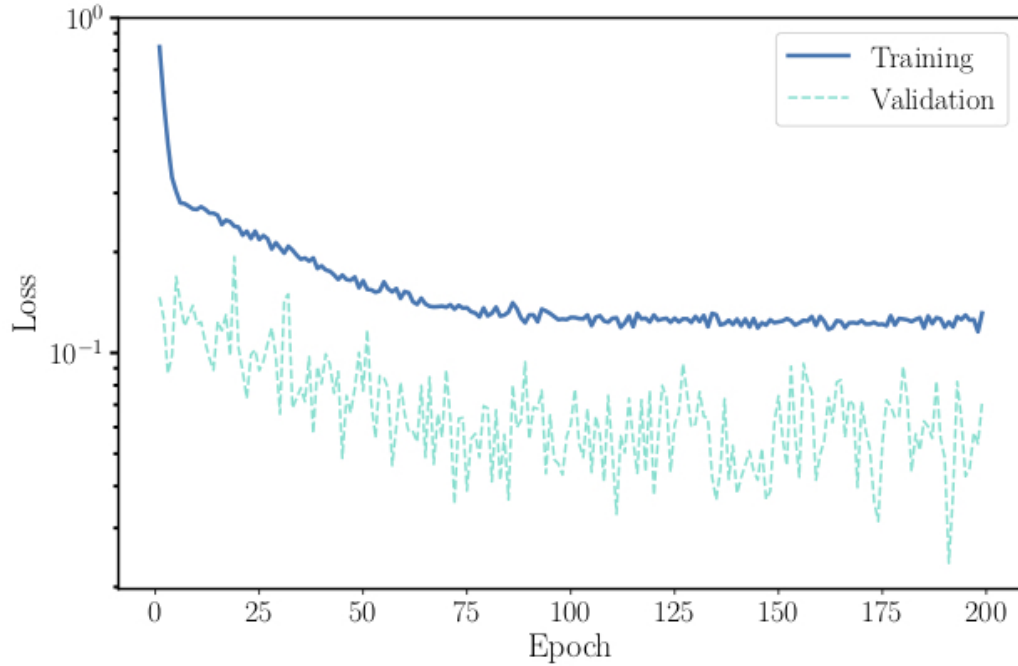


Figure 3.6: Training and validation loss after each epoch. The validation loss being less than the training loss is a result of the dropout in the second to last layer of the network.

down dramatically, but the decreasing trend in the loss remains until about 100 epochs. Note that the validation loss can be less than the training loss because of the dropout applied to the second to last fully connected layer of the network. This is because during training the Resnet only has 50% of the neurons in the second to last layer working at a time, but during validation or post-training testing 100% of the neurons are functioning. The Resnet is not as effective without all of its neurons functioning so the loss is often less for validation tests than during training.

3.3 Results

We refer to the trained network as our Resnet. As a sanity check, we tested it on ‘Random Li/Noise/Foreground’ LIMs which had been rotated by integer multiples of 90° . Our resnet should be rotationally invariant (at least for 90° rotations about an axis parallel to the line of sight of the LIMs), so it should perform similarly on the rotated maps. After 100 trials, both rotated and unrotated maps had the same average loss and same average variance of the loss within $< 1\%$.

Example outputs of our Resnet can be seen in Figure 3.7. We show three cases chosen by hand to illustrate different regimes. In the first, the Resnet accurately predicts the luminosity function for a LIM generated from parameters similar to the ‘Fiducial Li’. The next shows a case where the Resnet performs similarly well for a LIM with a very different luminosity function. Finally, we show a case where the Resnet fails to accurately reproduce the true luminosity function. By inspection, we find that the Resnet tends to perform worst when the underlying luminosity function has a low number of bright sources compared to the ‘Fiducial Li’ model.

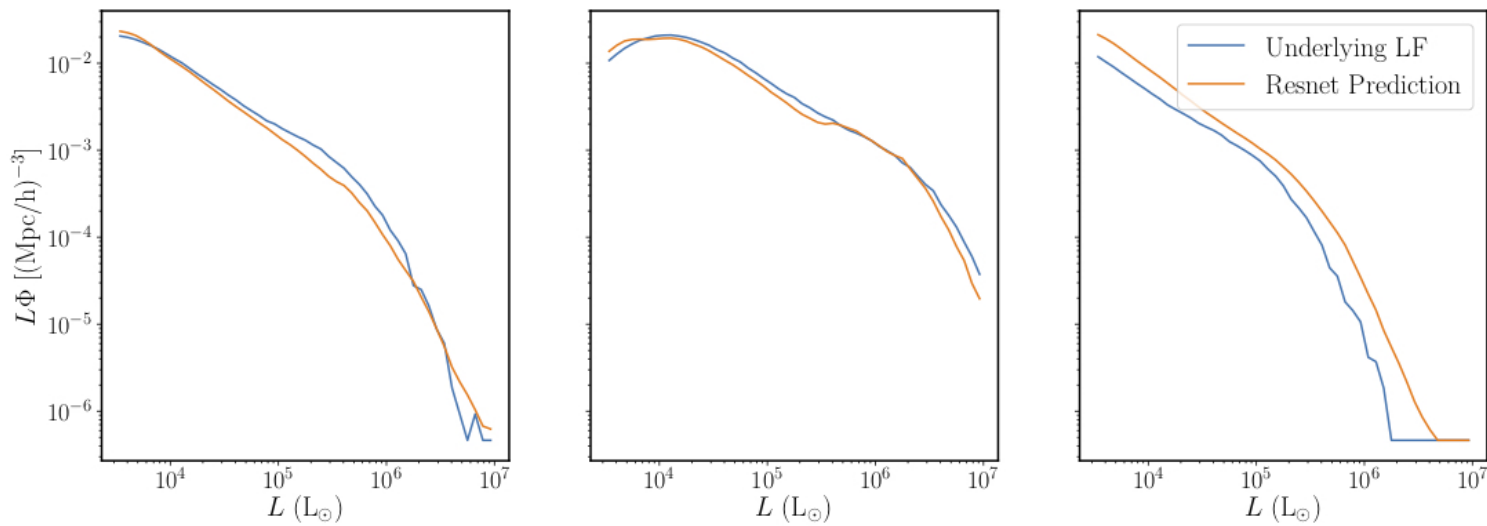


Figure 3.7: Three luminosity function predictions from the Resnet and the accompanying true underlying luminosity function. The left figure shows a map with underlying luminosity function that is similar to ‘Fiducial Li’, the middle and right figures show the same for models which differ significantly from the fiducial case, the Resnet performs well in the middle case and poorly in the right case. The three maps were manually chosen from the validation set.

CHAPTER 3. LIM WITH NEURAL NETWORKS

When training, we know the true luminosity function of a simulated map, so we can use a loss function to assess the network’s performance. However, in a real analysis we would hope to test our trained network on a single data set where the true values are unknown. In order to estimate how much we could trust the network in this situation, we examine the fractional difference

$$\delta L\Phi = \frac{L\Phi_{\text{prediction}}(L) - L\Phi_{\text{true}}(L)}{L\Phi_{\text{true}}(L)}. \quad (3.8)$$

as a function of luminosity between the predicted and true quantities. With a large ensemble of test realizations, we can generate a confidence interval around the true value, which approximates the error bar we would place on a true measurement. For our figure of merit, we will quote the 95% confidence interval on $\delta L\Phi$.

Now that we have a trained Resnet, we can study how it performs under different conditions. We focus on three main scenarios:

1. The case the Resnet was designed to handle best: a ‘Fiducial Li’ luminosity function with varying noise and foreground amplitudes. This models the situation where our fiducial model is close to the truth.
2. A variety of ‘Random Li’ mocks. Though the Resnet was trained on models in this space, the nature of our priors means that less time is spent on training models that differ significantly from fiducial.
3. Models and contaminants outside of the space of training data. This accounts for

CHAPTER 3. LIM WITH NEURAL NETWORKS

the possibility that the signal on the sky contains aspects not accounted for in the synthetic data.

For each test, we examined a number of maps equal to the number of validation maps used ($5796 \times 0.2 \approx 1159$ maps). It should be reiterated that all of the dark matter catalogs used in this testing step were taken from the set left out of the training data. Refer to Table 3.1.3 for a reminder of what effects are included in each test set.

3.3.1 Tests on trained data

In order to assess the performance of our Resnet we can compare to forecasts using analytic methods. For the simulated COMAP data we are using here, we can compare our forecasted constraints on the luminosity function to those from [55]. Their work, which forecast constraints on the underlying luminosity function of a LIM using a joint power spectrum and voxel intensity distribution analysis (PS/VID analysis hereafter), used what we are calling ‘Fiducial Li’ and ‘Fiducial Noise’ models with no foregrounds.

The comparison is shown in Figure 3.8. The contour for the Resnet shows the 95% confidence interval about the median of the relative errors over the entire set of LIMs tested while the [55] 95% confidence interval comes from their MCMC analysis. The red crosses show the luminosity bins we used for our Resnet. Though we are comparing two forecasts using the same models, the forecasts are not exactly equivalent. The PS/VID forecasts found errors on the *parameters* of the [54] model, then propagate those errors to the luminosity function. The PS/VID analysis was also able to use the full frequency

CHAPTER 3. LIM WITH NEURAL NETWORKS

spectrum of the COMAP data, while our preliminary tests here had to sacrifice much of this information for memory reasons.

With these caveats in mind, the CNN and analytic forecasts appear to perform comparably well, with the Resnet confidence interval actually being smaller at low luminosities. The Resnet does worst at the highest luminosities, where any given box is expected to have very few sources. We trained on a range of Li model parameters so the Resnet was not specifically trained for the fiducial case we show in Figure 3.8. The Resnet generally has a precise prediction, but is biased. For low luminosities it generally over predicts while for higher luminosities it under predicts. Within these over and under predictions, it still generally contains 0 relative error within the 95% confidence intervals and is not very biased. We leave a full comparison between these methods, where the PS/VID MCMC is run on our type of non-parametric model and we have enough computing resources to train on the full COMAP cube, to future work. Even this rough comparison though is enough to suggest that, in the best case scenario, a CNN can perform similarly to or better than analytic analyses. As this is the test case that most resembles past work, we will compare all of our upcoming tests to the confidence interval obtained here.

Next we examine how our forecasts vary with different noise and foreground levels. Figure 3.9 shows the accuracy of the trained Resnet on ‘Fiducial Li’ LIMs with varying amounts of contamination. As the noise level of the maps is increased, the quality of the prediction decreases as expected. When foregrounds are added, the Resnet becomes biased towards under predictions. All of the forecasts still begin to fail drastically at the highest luminosities where we start to run out of bright emitters.

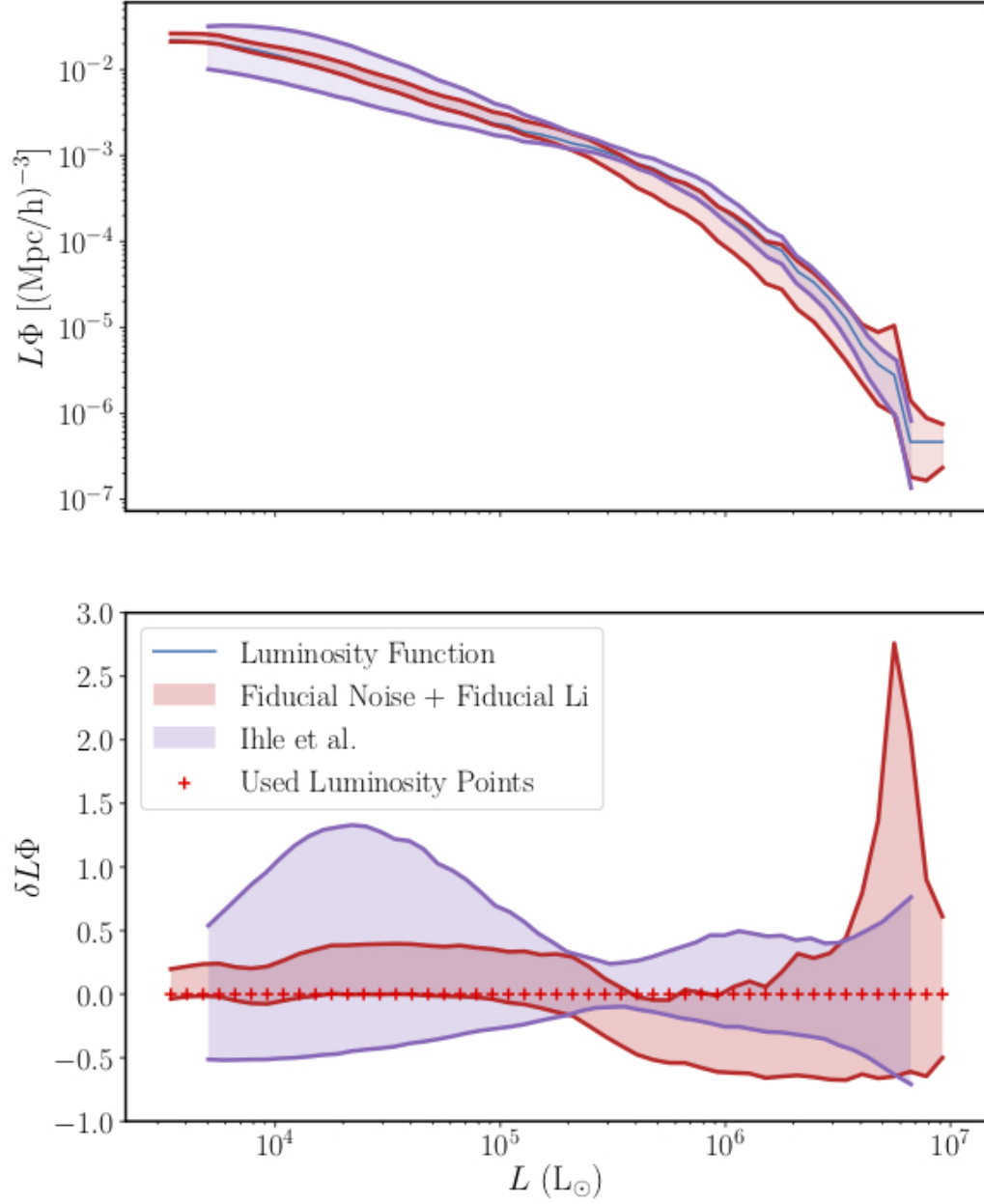


Figure 3.8: Comparison of 95% confidence intervals between our Resnet run on ‘Fiducial Li’/‘Fiducial Noise’/‘No Foregrounds’ test data and the results of [55]. *Top*: 95% confidence intervals placed directly on top of a ‘Fiducial Li’ luminosity function. *Bottom*: Same 95% confidence intervals on the relative error of the two forecasts. Red crosses show the luminosities used to train Resnet.

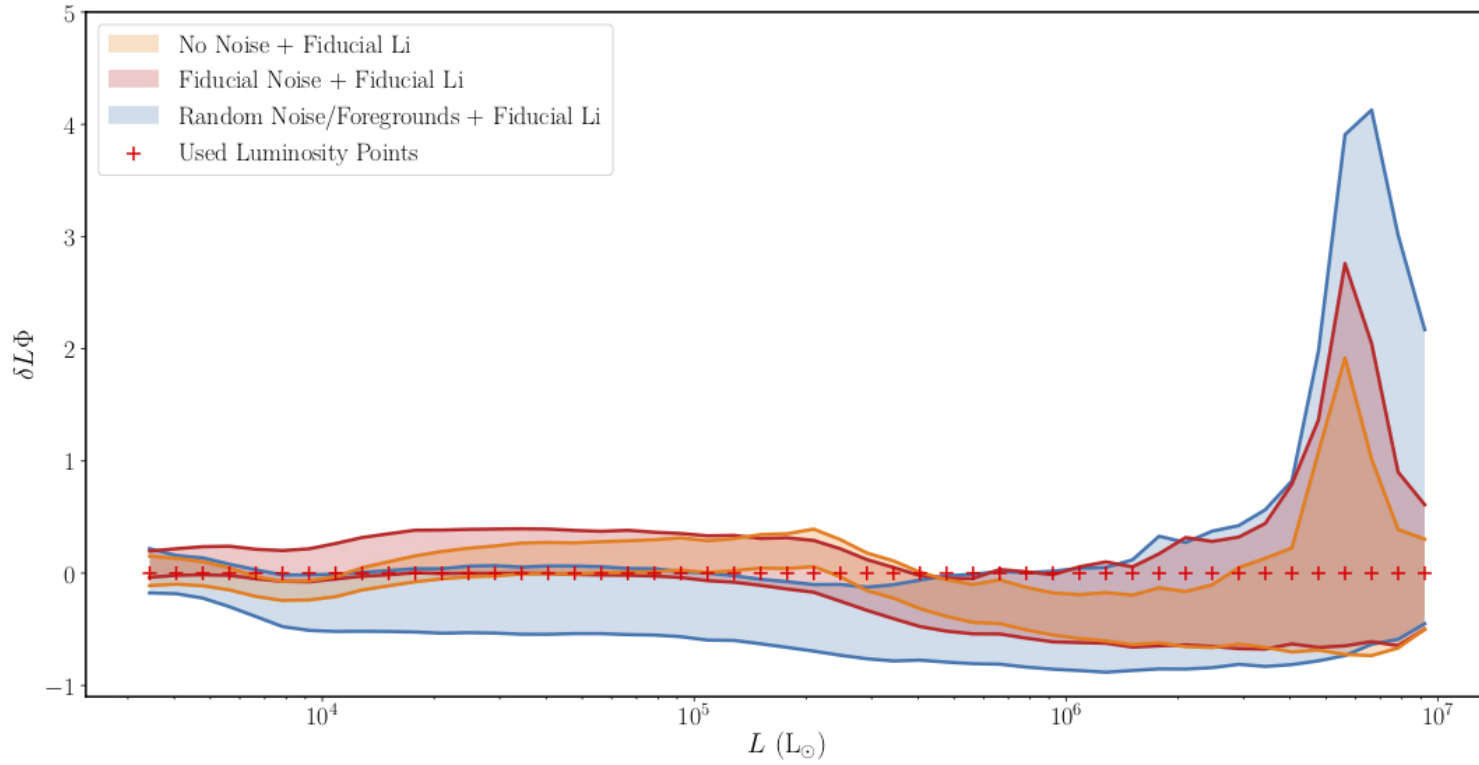


Figure 3.9: Relative 95% confidence intervals for test data with no noise/foregrounds (orange), fiducial noise with no foregrounds (red), and random noise/foregrounds (blue). All LIMs used the ‘Fiducial Li’ signal model. Scenario descriptions are in Table 3.1.3. The red interval shows the same case from Figure 3.8.

CHAPTER 3. LIM WITH NEURAL NETWORKS

Now that we know our Resnet can generally handle contamination, we want to see how it performs with different signal models. Figure 3.10 shows the 95% confidence intervals for the Resnet results when tested on ‘Random Li’ test LIMs, with same noise scenarios as Figure 3.9.

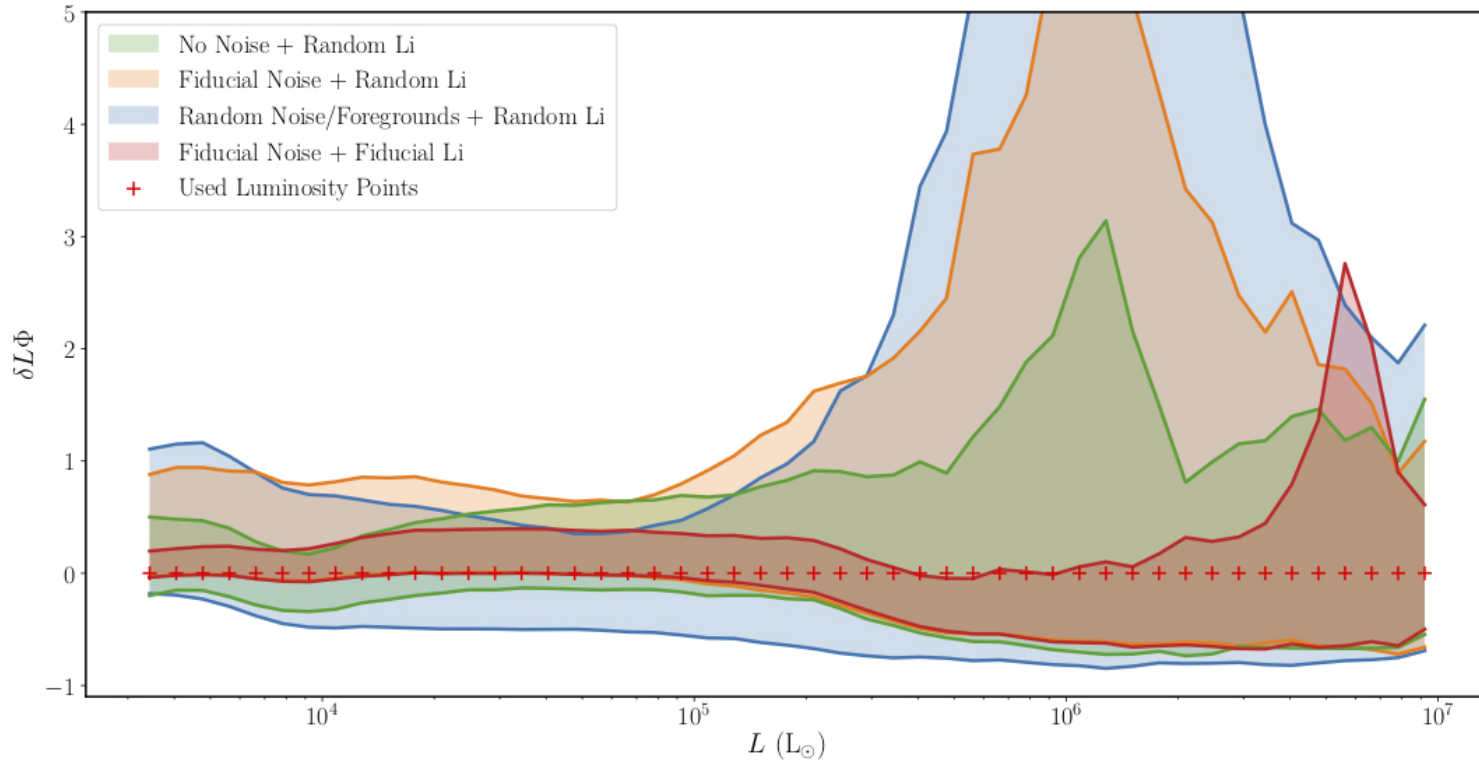


Figure 3.10: Same as Figure 3.9, but instead of testing on ‘Fiducial Li’ LIMs it is tested on ‘Random Li’ models. The red contour from the previous two figures is shown here as a comparison. Red crosses show the luminosities that we trained the Resnet on.

CHAPTER 3. LIM WITH NEURAL NETWORKS

Due to the diversity of the Random Li LIMs and luminosity functions, these tests are less constraining than the ones in Figure 3.9. However, the scenarios here do not exhibit the over and under prediction biases that the Fiducial Li LIMs tests did. In the ‘Random Li’ test set, we expect to periodically encounter cases such as the right panel of Figure 3.7, where the Resnet performs poorly. These outliers reduce the performance of the Resnet, particularly at high luminosity. This suggests that, while the CNN may give biased results on our best-fit model, it is less likely to very large over or under predictions that may happen in situations where the true data might deviate significantly from expectations.

3.3.2 Tests on untrained data

So far the Resnet was tested on LIMs made from models within the space of the training data. However, any real observation has a chance of including unexpected effects which are not modeled in advance. It is generally believed that supervised machine learning, as used in this work, lends itself best to interpolation rather than extrapolation. Therefore, to see how robust the trained Resnet is, we must test it on scenarios not included in the training data. Each of the tests below use ‘Random Noise’ and ‘Random Foreground’ models.

First, we consider maps with an altogether different model for the underlying luminosity function, specifically that of [179]. The ‘Padmanabhan’ model uses a double power law to relate halo masses to L_{CO} , as opposed to the ‘Fiducial Li’ which uses power-law scalings on top of the [177, 178] star formation rates. Although both models generally produce similar expected luminosity functions, the detailed shapes are somewhat different with the Padmanabhan model expecting more bright sources. We tested on only fiducial parameters

CHAPTER 3. LIM WITH NEURAL NETWORKS

of the ‘Padmanabhan’ model.

Next we consider an extra noise source, specifically the ‘Geometric Noise’ model described in Section 3.1.3. This is added in addition to the existing ‘Random Noise’ model, and is meant to represent the extra noise around the edges of a survey due to decreased observing time.

Finally, we noted previously that the worst outliers in our ‘Random Li’ sample came from maps with very few bright sources. To examine this behavior, we consider a hand-curated sample of ‘Random Li’ LIMs that contain fewer than 500 sources above $L = 10^6 L_\odot$. The [54] best fit parameters lead to more than 1000 sources in this luminosity range, so these maps deviate significantly from the fiducial case. This test considers the possibility that, while the true signal is within the range of the test data, it by chance specifically comes from a regime where the network performs badly.

The confidence intervals for our Resnet on these new scenarios can be seen in Figure 3.11. We see that the ‘Padmanabhan’ tests lead to biased results for luminosities below $5 \times 10^5 L_\odot$, but it does keep the relative error within the range $[-1, 1]$. This bias is expected as the Padmanabhan LIMs and luminosity functions are different than Li ones. The Resnet was trained on only Li ones so it was not ready for data produced in a new way. Both the ‘Less Bright Sources’ and ‘Geometric Noise’ lead to a loss of prediction versus the fiducial case. Geometric noise was something entirely new to the Resnet, so the constraints are sensibly much worse than any other test we consider.

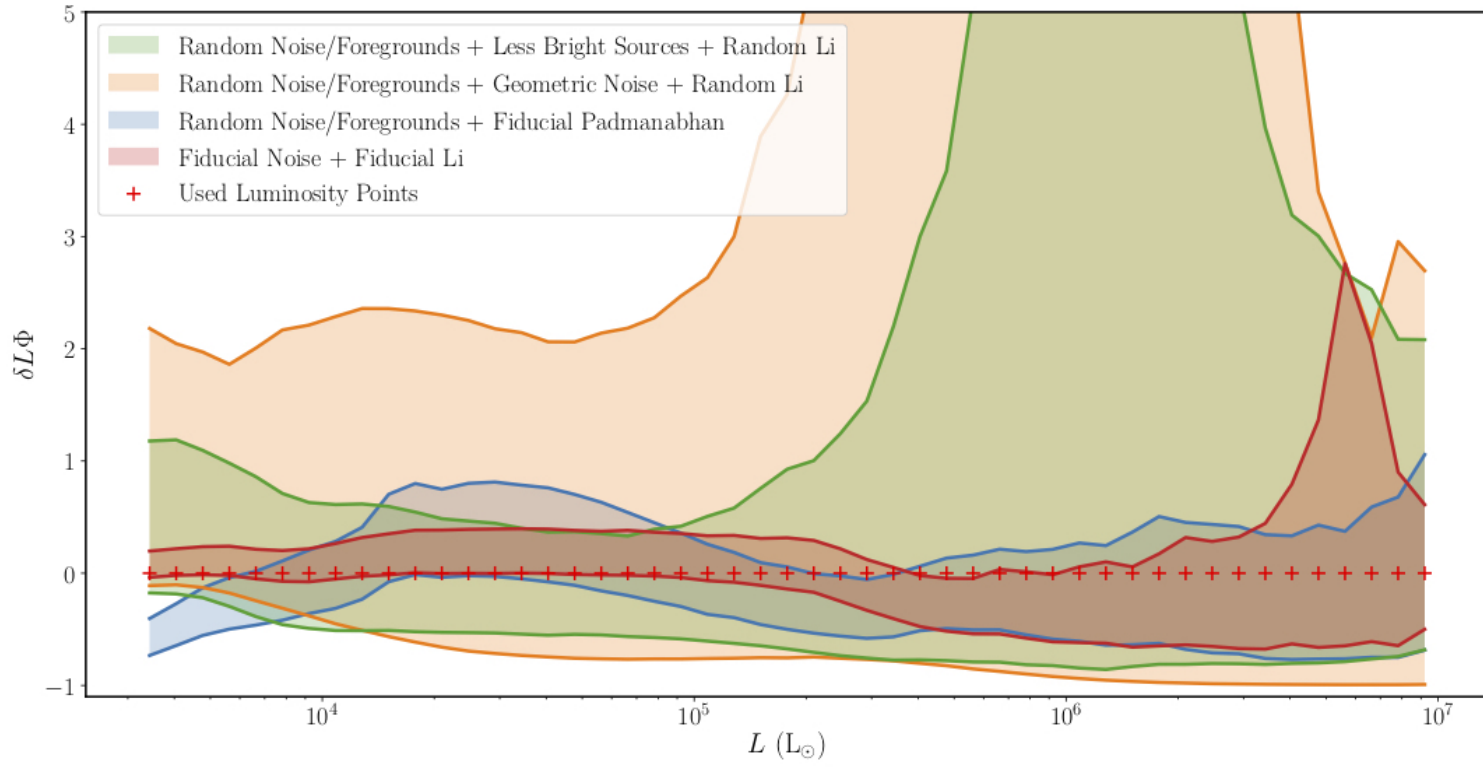


Figure 3.11: Confidence intervals for test data with effects not included in the training data, including the ‘Padmanabhan’ signal model (green), the hand-chosen ‘Less Bright Sources’ mocks (orange), and the extra ‘Geometric Noise’ contamination (blue). As before, the red contour from previous plots is shown here as a comparison.

CHAPTER 3. LIM WITH NEURAL NETWORKS

	Scenario	$10^4 L_{\odot}$	$10^5 L_{\odot}$	$10^6 L_{\odot}$
‘Fiducial Li’ signal	No Noise/Foregrounds	1.4	0.54	3.2
	‘Fiducial Noise’	1.0	1.1	4.0
	‘Random Noise/Foregrounds’	3.3	3.7	5.6
‘Random Li’ signals	No Noise/Foregrounds	2.6	2.7	9.3
	‘Fiducial Noise’	2.3	2.2	17
	‘Random Noise/Foregrounds’	4.8	4.7	32
Untrained effects	‘Padmanabhan’ signal	2.8	2.8	4.3
	‘Less Bright Sources’	4.7	4.8	27
	‘Geometric Noise’	7.6	11	120
Other	Ihle et al.	5.6	3.4	2.7

Table 3.4: Accuracy of the Resnet on different scenarios relative to the accuracy of the ‘Fiducial Li’/‘Fiducial Noise’/‘No Foregrounds’ case. Accuracy is measured as the difference between the maximum and minimum values of the 95% confidence interval at the given luminosities. All quoted values are relative to the accuracy of the fiducial scenario at $L = 10^4 L_{\odot}$.

Aside from the ‘Geometric Noise’, the ‘Less Bright Sources’ test yields similar constraints to our Random Li with Random noise and foregrounds test. Figure 3.12 zooms in on the high-luminosity confidence intervals for the Less Bright Sources’, and ‘Random Li’ tests. The shapes are extremely similar. This implies that the LIMs with less bright sources are driving the large size of the 95% confidence interval for the Random Li with Random noise and foregrounds test.

We can use the width of the 95% confidence interval in different bins to compare between the different cases. Table 3.3.2 compares these values to that of the ‘Fiducial Li’/‘Fiducial Noise’ scenario at $L = 10^4 L_{\odot}$. This allows us to summarize the performance of our Resnet across different scenarios and luminosities. For comparison, we also include the width of the [55] PS/VID confidence intervals. These values should not be taken solely by themselves as they do not contain any information about the biases the Resnet has for these different tests.

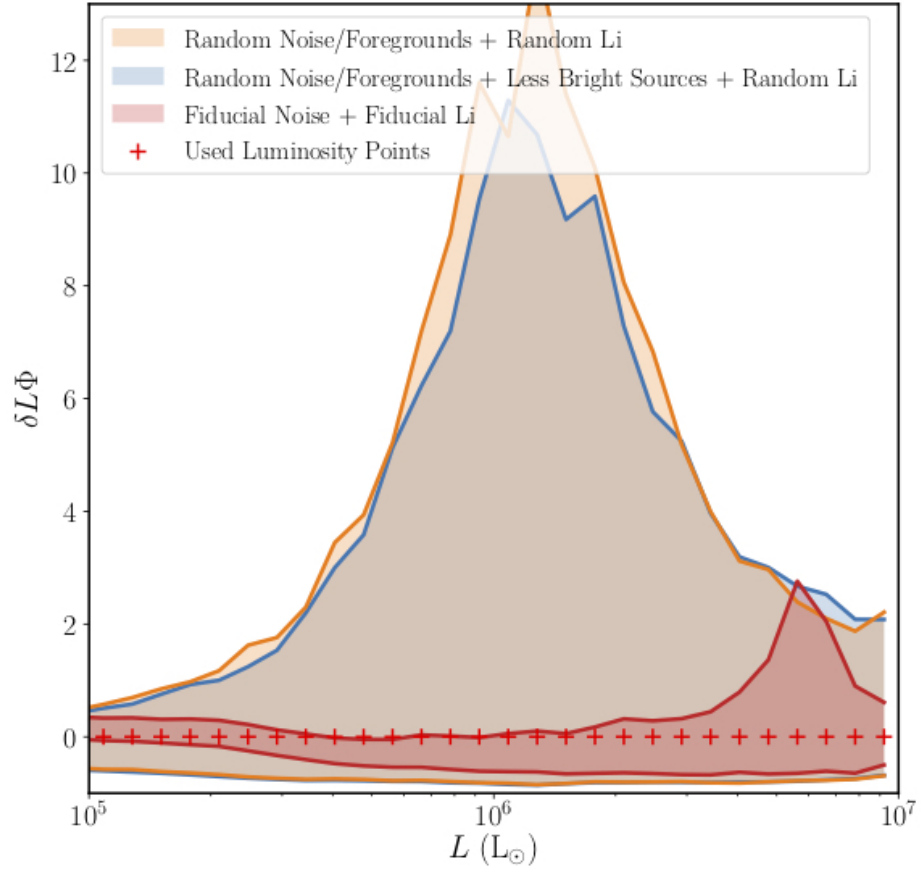


Figure 3.12: Zoomed in comparison of 95% confidence intervals for scenarios that fail in a similar fashion. The ‘Less Bright Sources’ (orange) and ‘Random Li’ (blue) cases all yield similar confidence intervals. As before, the red contour from previous plots is shown here as a comparison.

3.4 Discussion

From the above results we can now get a sense of how we expect this type of machine learning analysis to perform under different conditions. The results for the ‘Fiducial Li’ model indicate that, if all of the contributions to the signal and noise can be well modeled, a CNN can be a useful analysis tool. However, the other results give reason for caution. It is not easy to be sure *a priori* whether a map does or does not contain unmodeled effects, so there is not obvious way to tell which confidence interval one should assume around a learned luminosity function. Therefore, while we have demonstrated the utility of CNNs for this type of measurement, it remains an open question whether this technique can be safely used on real data.

There are a number of ways our Resnet could be improved for a full analysis. In this work, we made the simple choice to model the luminosity function as a series of 49 uncorrelated numbers. However, true luminosity functions tend to vary smoothly, with few sharp features. Future work could make use of, e.g., a spline model which would retain the non-parametric nature of our forecasts while taking advantage of the smooth nature of the luminosity function. There also exists a significant amount of space for improving on our network architecture. Only minor modifications were done to an existing network with only a small amount of effort going into the specific architecture modifications to obtain the results we did.

We used only a modest amount of computing power for this work. More resources would also enable more training of the network or larger networks. In addition, we did not make

CHAPTER 3. LIM WITH NEURAL NETWORKS

a full study of the effects of different architectures. With more computing power we could explore the parameter space of different models to find an optimized model. This work motivates future study of what types of networks are best for studying three-dimensional intensity mapping data.

Interestingly, we see that the Resnet generally performs better at the lowest luminosities. This may be due to the underlying range of possible LIMs that we trained it on. In Figure 3.1 we see that the 95% confidence band starts growing in size above a luminosity of $10^5 L_{\odot}$ as well. This decrease in performance is found in the Random Li tests that use the diverse luminosity functions, but not in the fiducial Li and Pandmanabhan tests. Possible training differences could help alleviate this issue, but we leave for future work a study of the effects of these “prior” choices on the final results.

We see above that, when allowing for the non-parametric nature of our model and the loss of line-of-sight information, our network performs comparably to the PS/VID analytic forecasts. This is another area worthy of additional consideration. Statistics like the power spectrum and VID of a map require human recognition of patterns in data and connection to the underlying physics. In complicated, highly correlated data sets like we see in LIMs it may be possible for a CNN to recognize additional patterns beyond what we can represent in analytic statistics. Combined with the fact that our Resnet does best with models near the center of the training range, this perhaps motivates a combined approach. One can imagine using the confidence intervals from a PS/VID analysis to set the range of training data for a network like ours, then seeing if the trained network can improve on those constraints. This would have the benefit of allowing the CNN to tease out extra patterns while avoiding

CHAPTER 3. LIM WITH NEURAL NETWORKS

some (but not all) of the pitfalls we describe here.

We also need not restrict the methods described here to luminosity function measurements. LIMs contain information about a wide variety of physics on scales ranging from star forming regions to the large-scale structure. One could easily imagine training a network like ours to measure cosmological parameters instead of luminosity functions. There has also been extensive study in the literature on what can be learned from cross-correlations between intensity maps and other tracers e.g. [133, 134, 190–193], which could be studied using our methods by feeding both data sets at once into a CNN.

Another use-case of the results shown here could be for foreground removal. Though the foreground contamination added to our maps is relatively minor, the network was able to handle it without much loss of accuracy. Even for maps with more severe contamination, one could apply conventional foreground cleaning to both the real and simulated data and use the network to help account for any residual emission. This could be particularly useful for cases where the foreground cleaning removes part of the signal in the process [109]. We considered only continuum foreground here, but our same approach may also be useful for separating out interloper emission lines at different redshifts, an effect which is not important for the CO(1-0) maps we consider here but will be very important for maps of several other lines e.g. [137, 194].

3.5 Conclusion

In this work we have presented the first application of a CNN to determine the underlying luminosity function of line intensity maps. We considered the example case of CO intensity maps observed by the currently-active COMAP survey. Under ideal conditions, our Resnet was found to have comparable to better precision in predicting the luminosity function as conventional techniques, but had a small bias. This work suggests that, used properly, machine learning could be a valuable tool in extracting astrophysical and cosmological information from intensity mapping data.

However, we also went on to explore some of the weaknesses of these techniques. We have shown that the accuracy degrades significantly under various conditions that the network was either not trained or insufficiently trained on. This crucial step has relevance not just to intensity mapping, but to all attempts to use machine learning for cosmological data analysis, and is often missing from past work in the literature. Though the great potential of neural networks is obvious, this work makes it clear that extreme care must be taken when applying them in this context, as small missing effects can drastically bias the output of neural networks.

Machine learning-based data analysis in cosmology is a field in its infancy. The proof-of-concept work we present here illustrates both the opportunities and challenges present in the application of these methods. With proper care, CNNs like our Resnet may play a valuable role in understanding the next generation of experimental data.

Chapter 4

Investigating new signatures of dark matter annihilation and scattering in the cosmic microwave background

The anisotropy of the cosmic microwave background (CMB) is a powerful tool for studying the nongravitational properties of dark matter (DM) [195]. In particular, DM interactions with particles of the Standard Model (SM) may leave detectable imprints in the CMB sky that deviate from the predictions of the concordance Λ CDM model, in which cold DM (CDM) is modeled as a nonrelativistic, collisionless fluid. If DM particles elastically scatter with baryons, the DM and baryon fluids exchange momentum, which suppresses

CHAPTER 4. INTERACTING DM SIGNATURES ON THE CMB

structure at small scales [56–61]. In case of DM annihilation (or decay), the resulting energy injection affects the era of cosmic recombination and increases the ionization fraction in the post-recombination universe, thereby increasing the optical depth for CMB photons and modifying the visibility function [13, 62–83].

DM annihilation and scattering with baryons are typically studied separately. Using a generic parametrization of the interaction can produce robust constraints, and the results of annihilation and scattering analyses can be individually applied to a broad class of DM models. For instance, in the case of asymmetric DM [196], there are scattering processes but no annihilation at times relevant for the CMB. Focusing on a single interaction channel is also particularly useful for comparing the CMB limits to limits from other DM searches, such as annihilation limits from indirect detection studies with gamma rays [197–201] and scattering limits from direct detection via nuclear and electronic recoil [202–213].

While indirect and direct detection experiments are designed to search for only annihilation and only scattering processes, respectively, the CMB is sensitive to both effects simultaneously. Previous studies [214] have shown that the next-generation CMB experiments will be able to distinguish between signals of a velocity-independent elastic scattering and of s-wave annihilation, given they are confidently detected in future data. However, it is not clear how those conclusions extrapolate onto a more general case of velocity-dependent interactions; furthermore, in the case of a marginal detection of a DM signal, signals from the two effects may be degenerate with each other and a joint likelihood analysis is necessary in order to avoid biasing measurements of DM parameters (the cross sections in particular).

CHAPTER 4. INTERACTING DM SIGNATURES ON THE CMB

In this chapter we investigate the combined effects of DM scattering and annihilation on the CMB anisotropy. Our goal is two fold. Using existing limits, we identify parts of the DM parameter space in which one can study the effects of annihilation and scattering separately. These correspond to regions where one effect largely dominates the CMB signal over the other. In the remaining part of the parameter space, we identify new signatures of DM in the CMB power spectra that can greatly differ from what arises in a naive analysis that separates the interactions and studies them independently. In these regions, both effects help drive and improve current CMB constraints.

We consider scattering and annihilation cross sections with power-law dependencies on v , the relative velocity between interacting particles. We focus in particular on s-wave annihilation, because it has the greatest impact on the CMB and is the least dependent on the details of the structure formation process [80–82]. We determine that annihilation tends to drive the CMB constraint under many scattering scenarios, especially for scattering cross sections that scale with large nonnegative powers of v , but also for v^{-2} scattering; the reverse situation occurs for v^{-4} scattering.

Models of DM interactions with light mediators can produce scattering cross sections that scale inversely with v , though only for even powers of v . Thus, there is a gap between v^{-2} and v^{-4} in which we could generically expect models to produce competing effects from scattering and s-wave annihilation in the CMB. We circumvent this issue by considering special situations in the context of photon-mediated models, described in Appendix A.1.

For the first scenario, we consider dipole DM, which may have electromagnetic inter-

CHAPTER 4. INTERACTING DM SIGNATURES ON THE CMB

actions through both an electric and a magnetic dipole moment. The strengths of these interactions are independent and can separately control the relative amount of scattering and s-wave annihilation. In the second scenario, we study the case of millicharge DM, in which scattering processes nominally drive the CMB constraint. If, however, only a sub-percent of DM is interacting, this component can tightly couple to the baryon fluid to the point that a stronger coupling no longer impacts the scattering signal [61, 215–217] (i.e., the effect of scattering saturates), while annihilation does not have this limitation. Using *Planck* 2015 temperature, polarization, and lensing anisotropies measurements, we analyze these scenarios to study what effect the interplay of scattering and s-wave annihilation has on forming limits on the models.

The chapter is organized as follows. In Sec. 4.1 we review the impact of DM-baryon scattering and DM annihilation on the CMB power spectra. In Sec. 4.2 we investigate the circumstances under which one of these processes is more important than the other and under which they both contribute in driving current CMB constraints. We use photon-mediated models to explore the combined effect of scattering and annihilation. In Sec. 4.3, we analyze these models to obtain improved CMB constraints. We conclude in Sec. 4.4.

This chapter is based heavily on work in preparation with coauthors Kimberly Boddy, Vivian Poulin and Vera Gluscevic.

4.1 Modified CMB physics

In this section, we describe the impact of DM interactions on the CMB. We discuss DM scattering with baryons in Sec. 4.1.1 and DM annihilation in Sec. 4.1.2.

We model the interacting DM χ as a cold, nonrelativistic fluid that features both scattering and annihilation, unless otherwise stated. Furthermore, we allow for the possibility that this interacting species of DM is only a subcomponent, representing a fraction

$$f_\chi \equiv \frac{\Omega_\chi}{\Omega_{\text{DM}}} \quad (4.1)$$

of the total DM density $\Omega_{\text{DM}} = \Omega_\chi + \Omega_{\text{CDM}}$, while the remaining component is standard CDM.

4.1.1 Dark matter scattering

We first consider the scenario in which DM elastically scatters with ordinary particles. In particular, we focus on scattering with baryons (i.e., protons, electrons, and helium nuclei) and denote the type of baryon involved in the interaction with a subscript t . We ignore interactions with photons. The momentum-transfer cross section¹ has the assumed form $\sigma_{\text{MT}} = \sigma_S v^{n_S}$, where v is the relative velocity between scattering particles and n_S is an integer determined by a particular DM model. Each type of baryon may scatter with a different $\sigma_{S,t}$, though we assume the same value of n_S for convenience.

¹The relevant quantity for early-universe cosmology is the momentum-transfer cross section, $\sigma_{\text{MT}} = \int d\Omega (1 - \cos \theta) \frac{d\sigma}{d\Omega}$. For brevity, however, we refer to σ_{MT} simply as the scattering cross section throughout this paper.

CHAPTER 4. INTERACTING DM SIGNATURES ON THE CMB

We incorporate the effect of DM scattering in the early Universe by modifying the standard Boltzmann equations [218]. In the synchronous gauge, the evolution equations for the density fluctuations, δ_b and δ_χ , and velocity divergences, θ_b and θ_χ , for baryons and DM, respectively, are

$$\begin{aligned}\dot{\delta}_b &= -\theta_b - \frac{\dot{h}}{2}, & \dot{\delta}_\chi &= -\theta_\chi - \frac{\dot{h}}{2}, \\ \dot{\theta}_b &= -\frac{\dot{a}}{a}\theta_b + c_b^2 k^2 \delta_b + R_\gamma(\theta_\gamma - \theta_b) + \frac{\rho_\chi}{\rho_b} R_\chi(\theta_\chi - \theta_b), \\ \dot{\theta}_\chi &= -\frac{\dot{a}}{a}\theta_\chi + c_\chi^2 k^2 \delta_\chi + R_\chi(\theta_b - \theta_\chi),\end{aligned}\tag{4.2}$$

where the dot notation indicates a derivative with respect to conformal time, h is the trace of the scalar metric perturbation, a is the scale factor, k is the wave number for a particular Fourier mode, ρ_χ and ρ_b are the energy densities of the DM and baryons, and c_χ and c_b are their sound speeds. If χ represents an interacting subcomponent of the total DM, we have $\rho_{\text{DM}} = \rho_\chi + \rho_{\text{CDM}}$, and the Boltzmann equations for CDM remain unchanged from the standard case.

The factor R_γ is the coefficient of the rate of momentum transfer between the photon and baryon fluids due to Thomson scattering. There is a similar factor for DM-baryon scattering, whose form depends on the velocity dependence of the cross section:

$$R_\chi = \sum_t \frac{a\rho_t \mathcal{N}_{n_S} \sigma_{S,t}}{m_\chi + m_t} \left(\frac{T_b}{m_t} + \frac{T_\chi}{m_\chi} \right)^{(1+n_S)/2},\tag{4.3}$$

where $\mathcal{N}_{n_S} \equiv 2^{(5+n_S)/2} \Gamma(3 + n_S/2) / (3\sqrt{\pi})$ is a numerical factor and m_t is the mass of species t . We treat all baryonic particles as pointlike; accounting for the nuclear form factor

CHAPTER 4. INTERACTING DM SIGNATURES ON THE CMB

of helium produces a negligible correction [59].

DM scattering also couples the baryon and DM temperatures, given by

$$\begin{aligned}\dot{T}_b &= -2\frac{\dot{a}}{a}T_b + \frac{2\mu_b}{m_e}R_\gamma(T_\gamma - T_b) + \sum_t 2\frac{\rho_\chi}{\rho_t}R'_{\chi,t}(T_\chi - T_b) \\ \dot{T}_\chi &= -2\frac{\dot{a}}{a}T_\chi + \sum_t 2R'_{\chi,t}(T_b - T_\chi) ,\end{aligned}\tag{4.4}$$

where $\mu_b \approx m_p(n_H + 4n_{\text{He}})/(n_H + n_{\text{He}} + n_e)$ is the mean molecular weight of baryons; m_e and m_p are the masses of the electron and proton, respectively; n_e , n_H , and n_{He} are the number densities of electrons, hydrogen, and helium, respectively; and T_γ is the photon temperature. The coefficient of the rate of heat transfer is

$$R'_{\chi,t} = \frac{m_\chi}{m_\chi + m_t}R_{\chi,t} .\tag{4.5}$$

Thus far, we have assumed $n_S \geq 0$. For negative values of n_S , the relative bulk motion of the DM and baryon fluids must be accounted for in the Boltzmann equations, introducing nonlinearities [57, 61]. In the case of $n_S < 0$ and $f_\chi = 1$, we modify Eq. (4.3) to be [57]

$$R_\chi = \sum_t \frac{a\rho_t\mathcal{N}_{n_S}\sigma_{S,t}}{m_\chi + m_t} \left(\frac{T_b}{m_t} + \frac{T_\chi}{m_\chi} + \frac{V_{\text{RMS}}^2}{3} \right)^{(1+n_S)/2} .\tag{4.6}$$

When dealing with $n_S < 0$ and $f_\chi < 1$, we follow Ref. [61], which further modifies Eqs. (4.3) and (4.4). We refer the reader to Ref. [61] for more details.

The dominant effect of DM scattering on the CMB power spectra is the suppression of

CHAPTER 4. INTERACTING DM SIGNATURES ON THE CMB

power at small scales, as shown by the orange curves in Fig. 4.2. The interaction induces a drag force between the DM and baryon fluids, which reduces the growth of perturbations and the associated metric potentials that affect the CMB photons. Moreover, the suppression is greater for the smaller density-perturbation modes, because they enter the cosmological horizon earlier and are subject to damping for a longer period of time. There is, however, an increase of power at large scales for the odd acoustic peaks due to a modification of the Sachs-Wolfe and early integrated Sachs-Wolfe terms from baryon loading [56]. The secondary effect of DM-baryon interactions is the reduction of the baryon-photon plasma sound speed, which reduces the frequency of the acoustic oscillations and shifts the peaks to smaller angular scales.

4.1.2 Dark matter annihilation

We now consider the case in which DM annihilates into SM particles. We refer to the total velocity-averaged annihilation cross section times velocity $\langle\sigma_A v\rangle = \sigma_A v^{n_A}$ simply as the s-wave ($n_A = 0$), p-wave ($n_A = 2$), d-wave ($n_A = 4$), etc. annihilation cross section. After velocity averaging, v here refers to the one-dimensional velocity dispersion of DM, with $v^2 = 3T_\chi/m_\chi$.

The main impact of DM annihilation is the modification of the evolution of the free-electron fraction x_e and the temperature of the intergalactic medium (IGM) T_{IGM} . The byproducts of annihilation do not directly ionize the IGM; instead, byproducts such as electrons inverse-Compton scatter on photons until they cool to keV energy to rapidly deposit their energy in the IGM by ionization and excitation [67]. More importantly, the

CHAPTER 4. INTERACTING DM SIGNATURES ON THE CMB

upscattered photons then Compton scatter and photoionize the IGM, and it is this process that is responsible for the bulk of the energy injected into the IGM.

The effect of DM annihilation is manifest in the CMB power spectra through changes in the free-electron fraction. The free-electron fraction enters in the line-of-sight solution of the CMB photon Boltzmann hierarchy [219] through the Thompson optical depth

$$\tau_{\text{depth}}(z) \equiv \int_0^z n_H(z) x_e(z) \sigma_{\text{Th}} \frac{dt}{dz'} dz' , \quad (4.7)$$

where t is the look back time. At early times, a higher free-electron fraction delays the decoupling of photons from baryons, thus increasing the time of recombination. As a result, the size of the sound horizon is larger, shifting the CMB acoustic peaks to lower multipoles ℓ , and higher multipoles are subject to diffusion damping for longer.

During the Dark Ages, increasing the free-electron fraction (and therefore the Thomson scattering rate of CMB photons) removes power at large ℓ due to an increase optical depth after recombination while increasing power of the polarization anisotropy for $\ell < 200$. These effects are illustrated in Fig. 4.2.

The impact of s-wave annihilation on the CMB can be characterized by the single parameter [74]

$$p_{\text{ann}} \equiv \mathcal{F}_{600} f_{\chi}^2 \frac{\langle \sigma_A v \rangle}{m_{\chi}} , \quad (4.8)$$

where \mathcal{F}_{600} is the fraction of the injected annihilation energy absorbed into the IGM at redshift $z = 600$, which depends on the DM mass and the annihilation channel. The fraction

CHAPTER 4. INTERACTING DM SIGNATURES ON THE CMB

\mathcal{F} is redshift-dependent, but since the CMB power spectra have the greatest sensitivity to s-wave annihilation at $z \sim 600$ [220], evaluating at that redshift yields an approximate constraint on $\langle\sigma_A v\rangle$. Note that contrary to standard definition, we include f_χ in the above expression to account for the possibility of a subcomponent of annihilating DM.

The case of $n_A \neq 0$ is more complicated. It is possible to apply an s-wave limit on p_{ann} to other annihilation scenarios by using a non-s-wave form of $\langle\sigma_A v\rangle$ in Eq. (4.8). A stronger velocity dependence (larger n_A) suppresses the energy injection rate and results in much weaker constraints. Through the velocity dispersion $v \sim \sqrt{T_\chi/m_\chi}$, the constraints depend on the thermal history of DM. Moreover, they are sensitive to the details of structure formation, while the s-wave constraints are not [80–82]. Therefore, we focus our discussion on s-wave annihilation for the remainder of this paper.

4.2 Scattering and annihilation signals in the CMB

We have discussed how DM scattering and annihilation individually influence the CMB, leaving distinct features in the power spectra. We are now interested in their combined impact. In Sec. 4.2.1, we determine the conditions under which both interactions are expected to play an important role for the CMB, based on existing limits from *Planck*. We then focus on two photon-mediated DM models (summarized in Appendix A.1) in Secs. 4.2.2 and 4.2.3 to demonstrate the combined effect of scattering and annihilation on the power spectra.

CHAPTER 4. INTERACTING DM SIGNATURES ON THE CMB

As in Sec. 4.1, we assume DM scattering and annihilation cross sections have the form

$$\sigma_{\text{MT}} = \sigma_S v^{n_S}, \quad \langle \sigma_A v \rangle = \sigma_A v^{n_A}, \quad (4.9)$$

where v is the relative velocity between the incoming interacting particles (DM particle and baryon for scattering and two DM particles for annihilation) and n_S and n_A are the integer power-law scalings of v for scattering and annihilation, respectively. Such cross sections are easily obtained in various simplified models of DM (e.g., see Ref. [221] in the context of collider searches) and in DM effective theories that can in principle match onto more UV complete theories (e.g., see Refs. [222–225] in the context of direct detection and Ref [59] in the context of the CMB). For reasons discussed in Sec. 4.1.2, we consider only s-wave annihilation ($n_A = 0$).

4.2.1 Previous limits from *Planck*

The forms of the scattering and annihilation cross sections depend on the particular DM model. We would like, however, to make an assessment of the importance of scattering versus annihilation in the CMB in a model-independent fashion. Once we know the target regime in which both scattering and annihilation should drive the CMB bound, we can analyze specific models in detail.

The simplest way of determining this target regime is to consider the current limits on the annihilation and scattering cross sections, for $f_\chi = 1$. The upper limit on s-wave annihilation from *Planck* 2015 temperature, polarization, and lensing data is $p_{\text{ann}} < 3.4 \times$

CHAPTER 4. INTERACTING DM SIGNATURES ON THE CMB

$10^{-28} \text{ cm}^3/\text{GeV/s}$ at 95% confidence [10], with a corresponding bound on σ_A through Eq. (4.8).² Analyses of DM-proton scattering place 95% upper limits on σ_S for $n_S \in \{-4, -2, 0, 2, 4\}$ using the same *Planck* data [59, 61].³

In Fig. 4.1 we plot the ratio of the limits, $\mathcal{F}_{600}\sigma_A/\sigma_S$, as a function of m_χ for various values of n_S . Since the limits of σ_S vary significantly between different n_S , we scale the ratios by a factor of C , indicated in the legend, to accommodate them all in one plot.

The form of the cross sections σ_A and σ_S is determined by a particular model of DM. For simple cases in which there is a single (relevant) interaction term in the Lagrangian, the scattering and annihilation cross sections are related through crossing symmetry [226] and thus have the same dependence on any coupling constants. Therefore, the ratio $p_{\text{ann}}/R_\chi \propto \sigma_A/\sigma_S$ is independent of coupling strength, reducing the number of free parameters to consider, and the requirement of fixing either p_{ann} or R_χ to its maximum limit is trivially satisfied.

For any given model, one can compute the equivalent $\mathcal{F}_{600}\sigma_A/\sigma_S \times C$ and check where it lies on Fig. 4.1. If it is well above the line corresponding to the value of n_s in the model, the signal will be dominated by the effect of annihilation. Otherwise, it will be dominated by the effect of scattering. As a simple example of how to interpret Fig. 4.1, let us consider the interaction between DM and protons to be

$$\mathcal{L}_{\text{int}} = \frac{g}{\Lambda^2} \bar{\chi} \gamma^\mu \gamma^5 \chi \bar{p} \gamma_\mu \gamma^5 p, \quad (4.10)$$

²The more recent *Planck* 2018 data yield a similar constraint of $p_{\text{ann}} < 3.3 \times 10^{-28} \text{ cm}^3/\text{GeV/s}$ [13].

³There are also limits for $n_S = 6$ in Ref. [59], but only for DM masses $\geq 1 \text{ GeV}$.

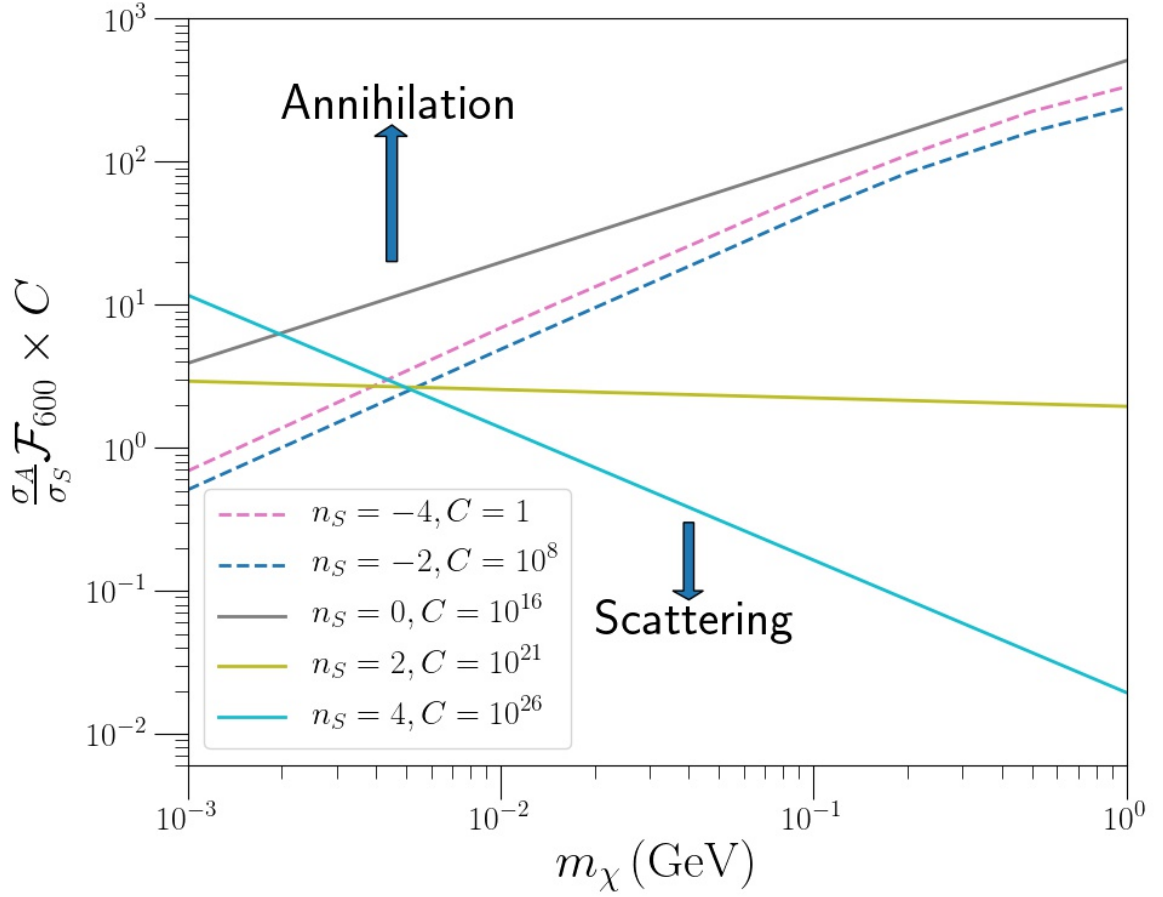


Figure 4.1: Boundaries for various value of n_S that demarcate the regions of expected annihilation and scattering domination for CMB constraints as a function of DM mass m_χ . All boundaries are obtained using *Planck* 2015 limits. For a given model and set of parameters, if the value of $\sigma_A \mathcal{F}_{600}/\sigma_S$ at a particular m_χ is well above (below) the boundary, the CMB constraints are driven by annihilation (scattering). For consistency, parameters must be chosen such that σ_A (σ_S) matches current CMB bounds, provided in the main text, in the annihilation (scattering) region. The different boundaries have been scaled by a factor of C only to fit them within the same plot, as indicated in the legend.

CHAPTER 4. INTERACTING DM SIGNATURES ON THE CMB

where g is the coupling and Λ is the scale of the effective theory. For simplicity, we assume DM scatters with and annihilates into protons only and $m_\chi > m_p$. In the nonrelativistic limit, the scattering cross section is independent of velocity ($n_S = 0$) and the annihilation cross section is s-wave ($n_A = 0$) such that

$$\sigma_S = \frac{3g^2\mu_{\chi p}^2}{\pi\Lambda^4}, \quad \sigma_A = \frac{g^2m_p^2}{4\pi\Lambda^4}\sqrt{1 - \frac{m_p^2}{m_\chi^2}}, \quad (4.11)$$

where $\mu_{\chi p}$ is the reduced mass of DM and the proton. In the limit $m_\chi \gg m_p$, we have $\sigma_A/\sigma_S = 1/12$. Accounting for the scaling factor C in Fig. 4.1 and taking $f_\chi, \mathcal{F}_{600} \sim 1$, we see that this model lies well above the $n_S = 0$ boundary, indicating annihilation drives the CMB bound and scattering is unimportant. It is also possible to get some rough generic expectations based on Fig. 4.1. Given the value of the pre-factors C , it is reasonable to expect annihilation to dominate if $n_S \geq -2$, while scattering dominates for $n_S = -4$. While this assertion is certainly model-dependent, we do not necessarily expect extremely large differences between σ_A and σ_S to be generic in the simplest of models.

Additionally we are interested in identifying what cross section parametrizations lead to DM scattering and annihilation having comparable impact on the CMB power spectra. In order to investigate situations in which the effects of scattering and annihilation can be equally important, we focus on the two scenarios that, from previous analysis, come the closest: $n_S = -2$ and $n_S = -4$. We note that $n_S = -3$ would be an ideal case study, but a velocity scaling with odd powers is not straightforwardly produced in simple DM models.

CHAPTER 4. INTERACTING DM SIGNATURES ON THE CMB

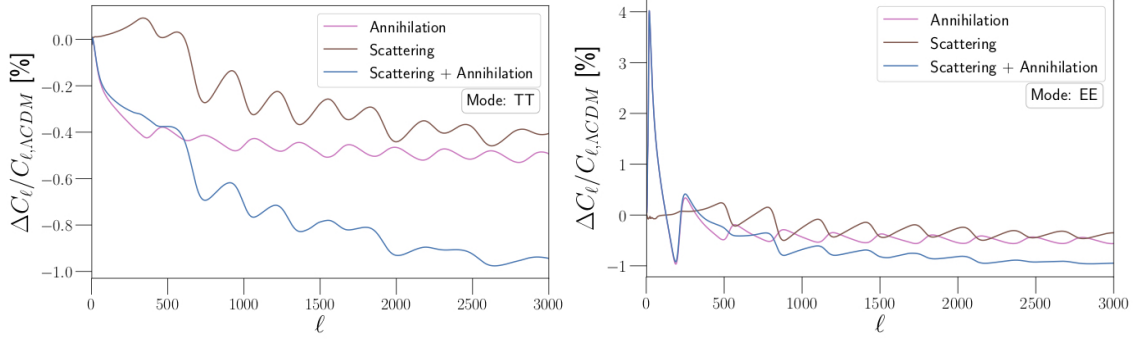


Figure 4.2: Residual CMB TT (left) and EE (right) power spectra for dipole DM with $\mathcal{D} = 10^{-15.3} e \text{ cm}$ and $\mathcal{M} = 10^{-18.7} e \text{ cm}$. The residuals $\Delta C_\ell = (C_{\ell, \chi} - C_{\ell, \Lambda CDM})$ are for $m_\chi = 1 \text{ MeV}$ and taken with respect to a ΛCDM cosmology, using the *Planck* 2018 TT, TE, EE + lensing best fit parameters [13]. The purple annihilation curve corresponds to only the s-wave annihilation from the magnetic dipole interaction, while the brown scattering curve shows only the scattering effects from the electric dipole interaction. The blue curve shows scattering effects from both the magnetic and electric dipole interactions and the annihilation effects from the magnetic dipole interaction (we neglect the p-wave annihilation due to the electric dipole).

4.2.2 Both effects from multiple couplings

The most straightforward way to obtain σ_A and σ_S that lie near one of the boundaries in Fig. 4.1 is to introduce more freedom in the DM model than the example we show at the end of Sec. 4.2.1. Specifically, we can vary σ_A and σ_S independently through different interaction terms.

To show what independent couplings for annihilation and scattering can lead to, we consider a model with an electric and magnetic dipole or dipole DM, described in Appendix A.1.1. The electric dipole gives a $n = -2$ velocity dependent scattering with baryons while the magnetic dipole gives the s-wave annihilation channel. The potential complication lies in the fact that the electric dipole also opens up a p-wave annihilation channel, while the magnetic dipole yields additional velocity independent scattering with baryons. However,

CHAPTER 4. INTERACTING DM SIGNATURES ON THE CMB

because the DM particles are non-relativistic, p-wave annihilation and velocity independent scattering are strongly suppressed compared to other effects at redshifts of interest⁴. The presence of both an electric dipole \mathcal{D} and a magnetic dipole \mathcal{M} allows us to independently vary the scattering and annihilation rates, because the scattering and annihilation rates only depend on \mathcal{D} and \mathcal{M} respectively.

We can apply the notation introduced in Eq. (4.9) to the cross sections in Sec. A.1.1 for dipole DM to see what interaction should dominate. We get $n_S = -2$, $n_A = 0$,

$$\sigma_S = 2\alpha\mathcal{D}^2 \quad (4.12)$$

and

$$\sigma_A = \frac{\alpha}{2}\mathcal{M}^2 \left[2 + \left(\frac{m_t}{m_\chi} \right)^2 \right] \sqrt{1 - \left(\frac{m_t}{m_\chi} \right)^2}. \quad (4.13)$$

We can then take the ratio of σ_A and σ_S to see if baryon scattering or annihilation constraints should dominate. The ratio we get for dipole DM is

$$\frac{\sigma_A}{\sigma_S} \approx \frac{1}{4} \left(\frac{\mathcal{M}}{\mathcal{D}} \right)^2, \quad (4.14)$$

for $m_\chi > m_t$. By comparing this to Eqs. (4.9), we see that dipole DM should be annihilation dominated for comparable values of \mathcal{M} and \mathcal{D} .

In Figure 4.2 we show the effects of baryon scattering and annihilation on the CMB when fixing either $\log_{10}(\mathcal{D}/e\text{ cm}) = -15.3$, $\log_{10}(\mathcal{M}/e\text{ cm}) = -18.7$, or both simultaneously. This

⁴Strictly speaking, at $z \lesssim 50$ structure formation might lead to non-negligible p-wave annihilation in halos. We neglect these effects for simplicity here as they would not change much the results and add a layer of astrophysical uncertainties. See e.g. Refs. [80–82].

CHAPTER 4. INTERACTING DM SIGNATURES ON THE CMB

point in parameter space was chosen because the amplitude of both effects are comparable and is on the boundary of the 95% exclusion region we find in Sec. 4.3.1. Most other points in parameter space have one effect clearly dominating over the other. We compare the case where both effects are present to the case where only one of the two effects is present.

When both interactions are included simultaneously, the effects are mostly additive: they do not cancel each other, rather they help improve the constraining power of the CMB.

Overall, the signals at large multipole ($\ell > 100$) tend to resemble the oscillatory features of scattering, but with extra damping due to the annihilation. On the other hand, the low-multipole part is closer to that of annihilation as it dominates for low multipole. This is especially visible in the polarization, where the increase in the height of the reionization bump, a bump in the polarization power spectrum for $l < 10$ that is due to scatterings that take place during reionization, is typical of the effect of DM annihilation.

There are however some noticeable differences compared to what is obtained when including solely either effect. In both temperature and polarization, the effective Silk damping scale is much larger as it is affected both by the delayed recombination and the effect of DM-baryon scattering, resulting in a strong reduction of power at all multipoles. It is also striking to see that oscillations in the residuals when only one effect is activated are exactly out of phase. This is because annihilation leads to an overall shift of the spectrum (due to delayed recombination), while the scattering mostly affects the Doppler-term. Hence, the combined effects lead to a different amplitude between maximas and minimas, compared to

CHAPTER 4. INTERACTING DM SIGNATURES ON THE CMB

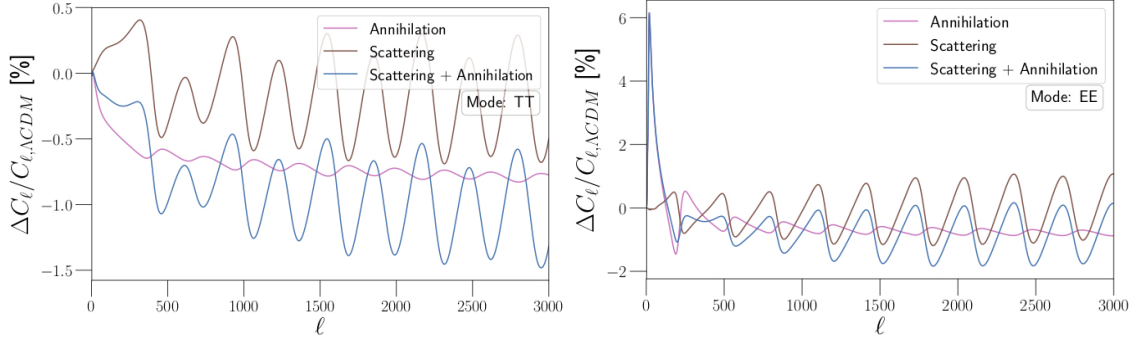


Figure 4.3: Similar to Fig. 4.2, but for millicharge DM instead of dipole DM and with fractional electric charge $\epsilon = 10^{-4.7}$, comprising a fraction $f_\chi = 10^{-2.9}$ of all DM. The purple curve shows the residual for a cosmology with only DM annihilation, brown shows only DM-baryon scattering, and solid blue shows both interactions.

activating only one of the effect.

4.2.3 Both effects from scattering saturation

For the case of $n_S = -4$, we explore an interesting effect that allows annihilation to become important for an otherwise scattering dominated model. The discussion in Sec. 4.2.1 incorporates assumptions and previous constraints that are valid only for $f_\chi \sim 1$. At face value, lowering f_χ should only make scattering more important, since annihilation effects are proportional to f_χ^2 , while scattering effects are proportional to f_χ . However, at a small enough f_χ , the maximally allowed rate R_χ^{\max} does not continue increasing as $1/f_\chi$. Instead, the effect of scattering saturates once the DM and baryon fluids become tightly coupled and more interactions do not further influence the density and velocity perturbation equations. A sufficiently small fraction of tightly-coupled DM is indistinguishable (in a finite-precision CMB instrument) from a small, additional component of baryons [61, 215–217, 227]. Therefore, the effect of scattering eventually saturates, the effect of annihilation

CHAPTER 4. INTERACTING DM SIGNATURES ON THE CMB

does not. Thus, for a situation in which scattering nominally dominates, we can explore the transition as scattering saturates and annihilation effects become important.

As a concrete example of baryon scattering saturation we consider the specific model of millicharge DM, described in Appendix A.1.2, in which DM is imbued with a small electric charge ϵe and $\epsilon \ll 1$. Millicharge DM has s-wave annihilation and a cross-section for scattering with charged particles that scales as v^{-4} . To check if millicharge DM is generically scattering dominated we follow Sec. 4.2.2 by applying the notation introduced in Eq. (4.9) to the cross sections in Sec. A.1.2. From this we get $n_S = -4$, $n_A = 0$ and

$$\sigma_S \approx \frac{2\pi\alpha^2\epsilon^2}{\mu_{\chi t}^2} \log\left(\frac{9T_t^3}{4\pi\alpha^3 n_t}\right) \quad (4.15)$$

$$\sigma_A = \frac{\pi\alpha^2\epsilon^2}{4m_\chi^2} \sqrt{1 - \left(\frac{m_f}{m_\chi}\right)^2} \left(2 + \frac{m_f^2}{m_\chi^2}\right), \quad (4.16)$$

where we have neglected an additional ϵ dependence of the logarithm in Eq. (4.15) which leads to percent level difference in the scattering cross-section.

We can then take the ratio of σ_A and σ_S to see if baryon scattering or annihilation constraints should dominate. The ratio we get for MDM is

$$\frac{\sigma_A}{\sigma_S} \approx \frac{1}{8} \frac{\mu_{\chi t}^2}{m_\chi^2} \frac{1}{\log\left(\frac{9T_t^3}{4\pi\alpha^3 n_t}\right)}. \quad (4.17)$$

The logarithmic term will be roughly constant during the time of interest and will have a

CHAPTER 4. INTERACTING DM SIGNATURES ON THE CMB

value around 50 [228], so for $m_\chi > 1$ MeV we have

$$\frac{\sigma_A}{\sigma_S} \approx 2.5 \left(\frac{1\text{MeV}}{m_\chi} \right)^2 \times 10^{-3}. \quad (4.18)$$

Comparing this to Fig. 4.1 we see that millicharge DM is indeed scattering dominated for masses of interest here.

In Fig. 4.3 we show the effects of baryon scattering and annihilation on the CMB temperature and polarization anisotropies, with $\epsilon = 10^{-4.7}$ and $f_\chi = 10^{-2.9}$. As before, the point in parameter space was chosen such that the amplitude of both interactions are comparable and is on the boundary of the 95% exclusion region we find in Sec. 4.3.2. The annihilation curve has the same features as those observed in Fig. 4.2, while the scattering curve is different due to the baryon scattering saturation. This is due to the baryon scattering saturation changing how the DM effects the CMB and results in a different spectra than what was discussed in Sec. 4.1.1. In this case it also acts as if there were more baryons that effected the CMB. As was the case with dipole DM in Figure 4.2, simultaneously including scattering and annihilation leads to additive effects, which can increase the constraining power of the CMB. The overall behavior is similar to previous case, with scattering dominating at small angular scales and annihilation taking over on large angular scales. Because of the different velocity dependence of the scattering between dipole and millicharge DM, there are however some noticeable differences at high- ℓ and we refer to Ref. [214] for a discussion about the ability to disentangle these features.

4.3 Looking for electromagnetic signals of Dark Matter in CMB data

We now analyze the dipole and millicharge DM scenarios discussed in the previous section. Unless noted otherwise, we compute the effects of DM annihilation using the EXOCLASS branch of the Boltzmann code CLASS [83, 229], which incorporates results from Ref. [230] to compute \mathcal{F}_{600} .⁵ For DM scattering, we incorporate the modified version of CLASS presented in Ref. [61].

We constrain the DM models with *Planck* 2015⁶ temperature, polarization, and lensing power spectra using the nuisance-marginalized joint TT, TE, EE (i.e., “lite”) likelihood within the Planck Likelihood Code v2.0 (CLIK/PLIK) [233, 234].

We explore the cosmological parameter space using the MONTEPYTHON-V3⁷ [235, 236] software package with a Markov chain Monte Carlo (MCMC) sampler. The MCMC sampler implemented in MONTEPYTHON-V3 uses the Metropolis-Hastings algorithm, and chain convergence is evaluated using the Gelman-Rubin convergence criterion $R - 1 < 0.05$ [237]. In addition to the six standard Λ CDM parameters (baryon density $\Omega_b h^2$, total CDM density $\Omega_{\text{CDM}} h^2$, Hubble parameter h , reionization optical depth τ_{reio} , amplitude of scalar perturbations A_s , and scalar spectral index n_s), we also vary new DM parameters associated with each model, as described in the subsequent subsections. In both cases, we perform analysis

⁵A more recent version of the Monte Carlo code used in Ref. [230] has now been released [231], but would not affect the conclusions of this work, as the time dependence of the energy deposition and other new subtle effects leaves negligible signatures in the CMB [74, 82].

⁶While this analysis was being finalized, the *Planck* 2018 data became public [232] but is not yet available in MONTEPYTHON-V3. We anticipate that bounds derived here can be improved by a factor of roughly 20%, similar to the improvement in the limit on p_{ann} between 2015 to 2018 data [13].

⁷https://github.com/brinckmann/montepython_public

CHAPTER 4. INTERACTING DM SIGNATURES ON THE CMB

runs at fixed DM mass with values $m_\chi = 1$ MeV, 10 MeV, 100 MeV, and 1 GeV.

4.3.1 Dipole dark matter

We fix the fraction f_χ of dipole dark matter to be 100% of the dark matter and allow the electric dipole coupling strength \mathcal{D} and the magnetic dipole coupling strength \mathcal{M} to vary as free parameters, along with the standard six Λ CDM parameters, with broad log-flat priors. The scattering cross section scales with an inverse power of relative velocity, so we must incorporate corrections arising from the relative bulk velocity. Moreover, the scattering limit from *Planck* for $f_\chi = 1$ places DM in a regime in which the assumptions in Ref. [57] are valid (see Ref. [61] for details), so we use the treatment shown in Eq. (4.6) (thereby neglecting any modifications to the temperature evolution in Eq. (4.4)).

In our analysis, we include both the electric dipole v^{-2} scattering and the magnetic dipole v^0 scattering. For the regime we are interested in and for $f_\chi = 100\%$ we get that the magnetic dipole scattering has no impact on the CMB, while the electric dipole scattering constraint dominates.

In Fig. 4.4, we show the exclusion regions in the \mathcal{M} vs \mathcal{D} plane. The exclusion regions or contours are the inverted 95% marginalized posterior probability distributions and exclude the shaded regions at the 95% confidence level using *Planck* 2015 data and are marginalized over the Λ CDM parameters. For small \mathcal{D} , the annihilation constraints dominate and exclude large values of \mathcal{M} , resulting in the flat, horizontal segments of the exclusion contours. At large \mathcal{D} , the scattering constraints from the electric dipole interaction dominate, rendering

CHAPTER 4. INTERACTING DM SIGNATURES ON THE CMB

the vertical exclusion contour, independent of \mathcal{M} .

As in Sec. 4.3.2, we show the estimated annihilation and scattering constraints. Annihilation predictions come from combining Eqs. (4.8) and (A.21) and values of \mathcal{F}_{600} extracted from Ref. [230] for the model of interest. Scattering was estimated with Eqs. (4.3) and (A.20). In Fig. 4.4 we find that the scattering predictions were generally correct while the annihilation predictions were off by about a factor of three. This discrepancy may be due to the more complete treatment of annihilation in EXOCLASS compared to our basic electron only annihilation at $z = 600$ in our analytic prediction.

We find an interesting transition regime for which the constraints are stronger when including the scattering and annihilation effects together. This region is the smoothed out corner between the scattering and annihilation dominated regions for each mass. The reason for why combination of annihilation and scattering in the case of dipole DM improves the limit over individual-effect analyses can be understood when examining the signals in Fig. 4.2. Both scattering and annihilation reduce power so when the shift in the acoustic peaks due to scattering is small, both effects can look similar and add together.

We can compare our results to previous work on dipole DM in [238], which considered multiple constraints. When concerned with the CMB, they only focused on baryon scattering and did not consider DM annihilation. For masses below 500 MeV, the best constraint on dipole DM was from the mass of the W boson. Such a constraint placed limits on the dipole moments such that $(\mathcal{D}^2 + \mathcal{M}^2)^{1/2} \leq 3 \times 10^{-16} e \text{ cm}$ and is independent of the DM mass in this mass range. At one GeV the main constraint used to come from

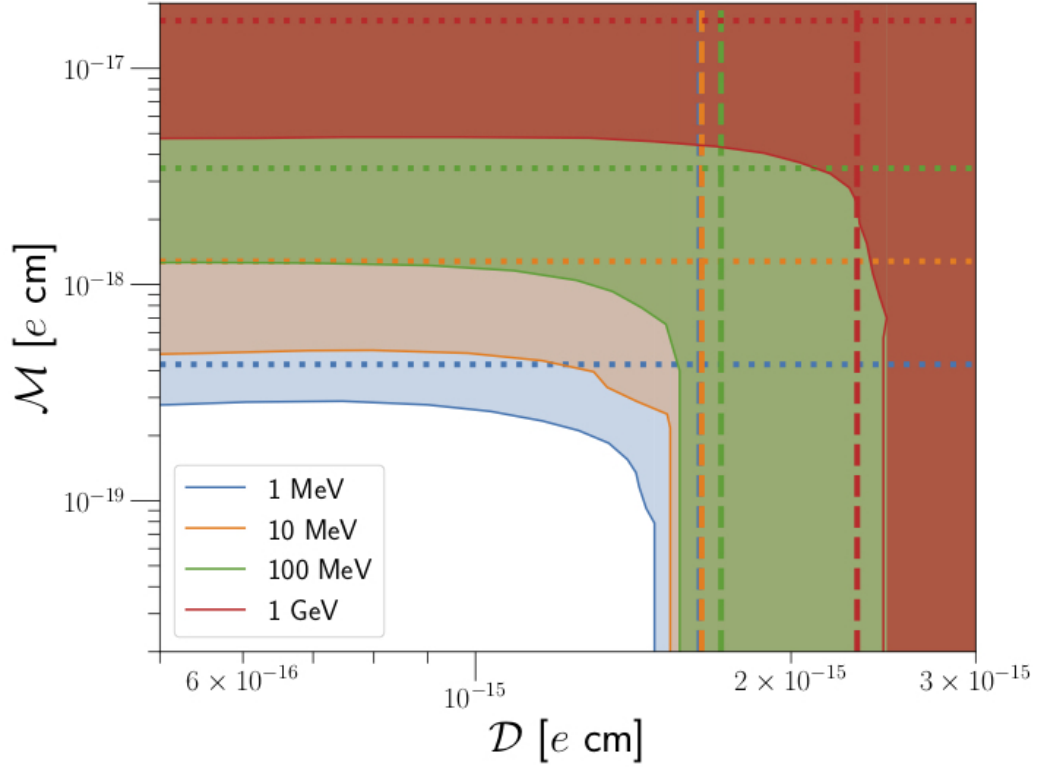


Figure 4.4: Exclusion contours for various masses of dipole dark matter as a function of the dipole coupling strengths. The shaded exclusion contours are the inverted 95% marginalized posterior probability distributions and exclude the shaded regions at the 95% confidence level using *Planck* 2015 data. Flat horizontal boundaries are due to annihilation constraints while the vertical boundaries are due to baryon scattering constraints. The dashed lines are the limits from DM annihilation alone, from Eqs. (4.8) and (A.21) and the dotted lines are the limits from DM-b scattering alone, from Eqs. (4.3) and (A.20).

CHAPTER 4. INTERACTING DM SIGNATURES ON THE CMB

X-ray Quantum Calorimeter (XQC) detector [239]. Although designed to probe the soft x-ray background, XQC can detect energy transfer by dark particles down to 1 GeV. At 1 GeV it can detect dipole couplings such that $(\mathcal{D}^2 + \mathcal{M}^2)^{1/2} \leq 6 \times 10^{-15} e \text{ cm}$.

In the case of our 1, 10 and 100 MeV runs, we find our (CMB) limit on \mathcal{D} to be an order of magnitude less constraining than the previous (W boson mass) limit. This is due to the W boson mass constraints being stronger than the CMB constraints, which we match. For one GeV the CMB scattering constraints are about a factor of 30 weaker for \mathcal{D} than XQC constraints. The inclusion of the impact of annihilation on the CMB leads to improved constraints on the magnetic dipole \mathcal{M} , which had not been done before. At one GeV the constraint is improved by an order of magnitude and at smaller masses the improvement is over two orders of magnitude.

4.3.2 Millicharge dark matter

We perform a similiar analysis to millicharge DM as we did for dipole DM in Sec. 4.3.1. Here we allow the fraction of millicharge DM f_χ and fractional electric charge ϵ to vary as free parameters. We use log-normal priors over the ranges $\epsilon \in [10^{-10}, 10^{-4}]$ and $f_\chi \in [10^{-4}, 1]$. These two parameters are used in addition to the six base Λ CDM parameters.

As with dipole DM, the scattering cross section has a negative value for n_S . On top of the negative n_S , we consider small values of f_χ which requires the use of the modifications to the scattering rate and temperature evolution Eqs. (4.3) and (4.4) from Ref. [61].

In Fig. 4.5 we show the 95% exclusion regions of f_χ versus ϵ , with $m_\chi = 1 \text{ MeV}$ and

CHAPTER 4. INTERACTING DM SIGNATURES ON THE CMB

for runs with only scattering (brown), only annihilation (purple), and both scattering and annihilation (blue). As expected, for small ϵ and large fraction f_χ , the scattering constraint dominates. On the other hand, increasing ϵ causes scattering to saturate and the posterior to flatten in ϵ for fractions $\log_{10} f_\chi \lesssim -2.7$. For $\log_{10} \epsilon > -4.7$, the effect of DM annihilation becomes important in constraining the model.

For small ϵ , the boundary of the exclusion region has the form $f_\chi \propto \epsilon^{-2}$. We expect this behavior, because the relevant cosmological observable that is constrained for DM scattering is the coefficient of the momentum-transfer rate, which scales as $R_\chi \propto f_\chi \epsilon^2$ as can be seen through the combination of Eqs. (4.3) and (A.25). The heat transfer rate can be a relevant and constraining quantity, but for negative values of n_S , DM does not couple to baryons at early times and the heat transfer is negligible on the CMB. As ϵ increases, DM scattering begins to saturate and the annihilation constraint becomes prominent. In this regime, after combining Eqs. (4.8) and (A.26), the constraint takes the form $f_\chi \propto \epsilon^{-1}$ when the annihilation parameter is set to its constrained upper limit.

In the case of millicharge, considering the effects of scattering and annihilation together produces the same result as a combination of the two: the region of the parameter space excluded from joint analyses of the two effects is a simple combination of the regions excluded by individual analyses, as seen in Fig. 4.5. This could be understood when examining Fig. 4.3: annihilation produces suppression of power in the CMB temperature, while scattering also produces a shift of the acoustic peaks towards smaller scales. Since the shift has a significant amplitude in the millicharge case, resulting oscillatory features seen in the residual signal are of large amplitude; they are sufficiently distinct from the suppression

CHAPTER 4. INTERACTING DM SIGNATURES ON THE CMB

produced by DM annihilation, and therefore the two processes have orthogonal effects on the CMB. For this reason, the combined limit is not substantially stronger than a combination of limits from individual effects. In the case of dipole DM, the two effects were of comparable size, and this lead to a stronger combined limit.

We can compare the exclusion contour of 1 MeV DM for scattering only to the similiar result from [61]. In their Fig. 8 we see the exclusion region for DM with v^{-4} DM-proton scattering. Our work differs because in their work, DM scatters on only protons while in our work, DM scatter on protons, electrons and helium nuclei, and that rather than use a specific model for their DM, they use $\sigma_{\text{MT,f}} = \sigma_0 v^{-4}$. After accounting for the different x and y axis of Fig. 4.3 and Fig. 8 of [61], we see that both contour boundaries line up and that our results agree with theirs. The maximum value of ϵ considered in this work corresponds to a larger maximum value of σ_0 than what was considered in [61], but for $\epsilon \lesssim 3 \times 10^{-7}$ our work matches theirs.

In Fig. 4.6 we show the 95% exclusion regions for all four DM masses under consideration. Each of the four cases display the same general trend as in Fig. 4.5. We show an estimated annihilation constraint, obtained by combining Eqs. (4.8) and (A.26) and values of \mathcal{F}_{600} extracted from Ref. [230] for the model of interest. These predictions match the contours at large ϵ , where the annihilation constraint dominates. Furthermore, we show the estimated scattering constraint, found with Eqs. (4.3) and (A.25), matches the contour for low ϵ .

For all four masses in Fig. 4.6, we see the effects of baryon scattering saturation which

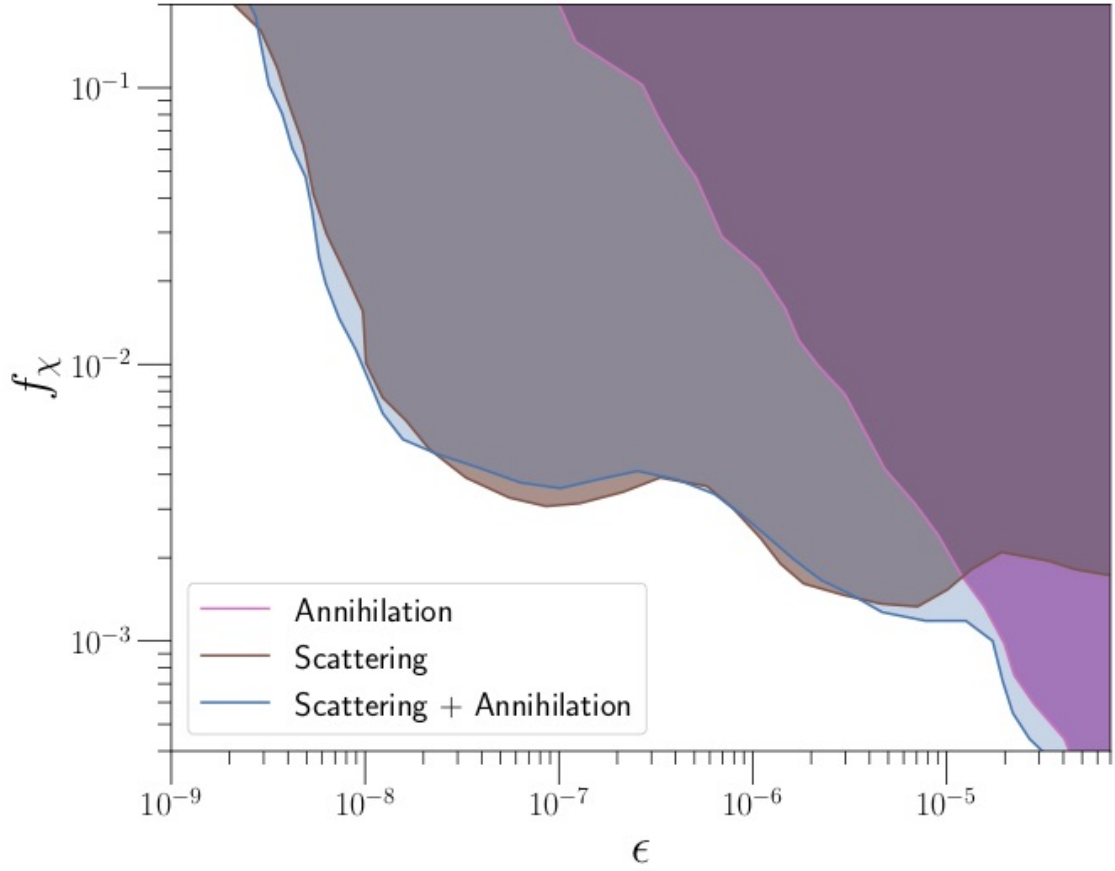


Figure 4.5: Shaded excluded regions for the fraction of millicharge DM f_χ as a function of the fraction electric charge ϵ for a DM mass of $m_\chi = 1$ MeV. Excluded regions are the inverted 95% marginalized posterior distribution. We show the contours from analyzing *Planck* 2015 temperature, polarization, and lensing data for the cases of only DM scattering (brown), only DM annihilation (purple), and both effects combined (blue).

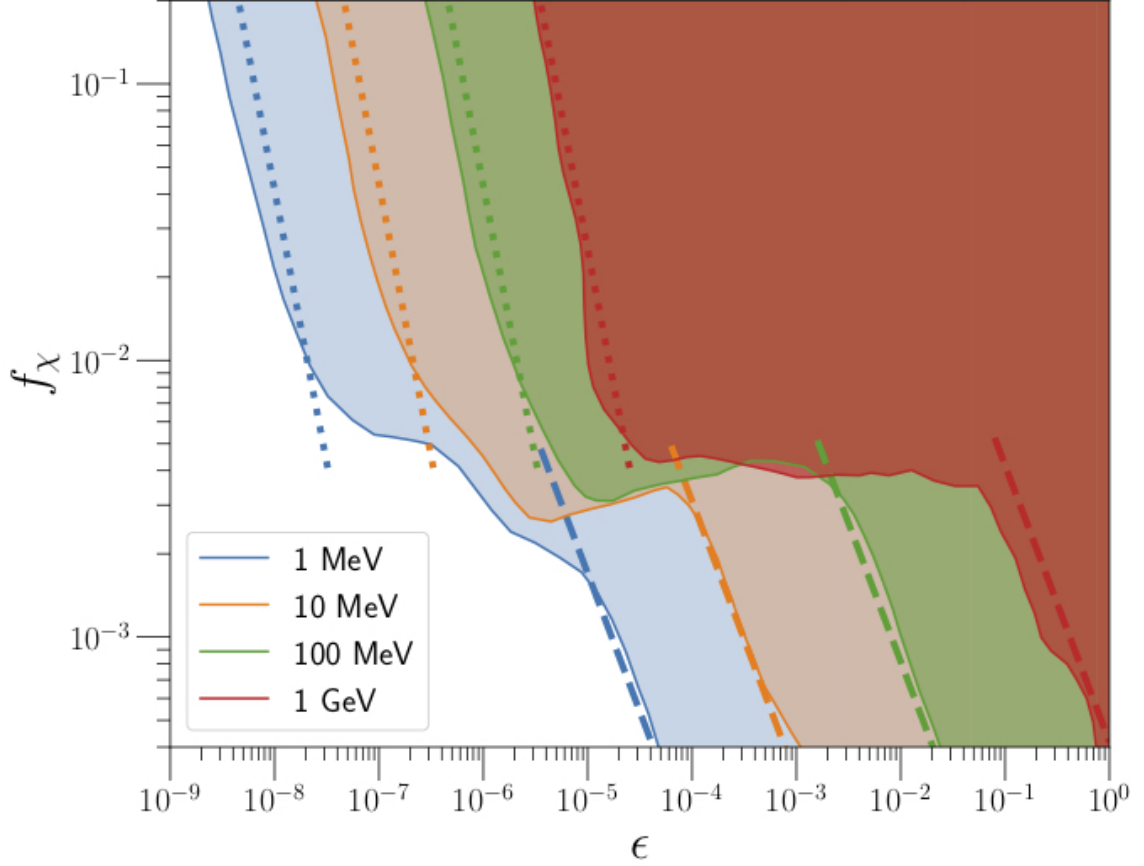


Figure 4.6: Excluded regions for the fraction of millicharge DM f_χ as a function of the fraction electric charge ϵ for DM masses of 1 MeV (blue), 10 MeV (orange), 100 MeV (green), and 1 GeV (red). Shaded excluded regions are the inverted 95% marginalized posterior distribution. We show the 95% CL contours from analyzing *Planck* 2015 temperature, polarization, and lensing data. The dashed lines are the limits from DM annihilation alone, from Eqs. (4.8) and (A.26) and the dotted lines are the limits from DM-b scattering alone, from Eqs. (4.3) and (A.25).

CHAPTER 4. INTERACTING DM SIGNATURES ON THE CMB

manifests different for the different masses. In the case of one GeV this leads to a plateau in the constraints with respect to ϵ between the predicted scattering and annihilation constraints. The lower masses of 10 and 100 MeV show their saturation by first reaching a maximum constraint on f_χ as ϵ increases. As ϵ increases further the constraint weakens until the annihilation constraint becomes relevant. For one MeV, the saturation displays a more complicated feature. There are multiple joints where the constraint on f_χ gets weaker with ϵ only to strengthen again as ϵ increases further. We checked that these features are not a numerical artifact but leave a detailed investigation for future work. As with the higher masses, the saturation affects end when annihilation constraints become relevant.

While dipole DM has a clear region where the constraints are improved when considering both effects, it is not clear if millicharge DM has one as well. In Fig. 4.3, annihilation produces suppression of power in the CMB temperature, while scattering also produces a shift of the acoustic peaks towards smaller scales. Since the shift has a significant amplitude in the millicharge case, resulting oscillatory features seen in the residual signal are of large amplitude; they are sufficiently distinct from the suppression produced by DM annihilation, and therefore the two processes have orthogonal effects on the CMB. It is easy to separate out the individual effects, so there is no degeneracy between the two which. This lack of degeneracy results in the combined limit that is not stronger than the individual limits.

Finally, we note that millicharge DM has drawn recent attention in effort to explain the anomalously large 21 cm absorption signal [227, 228, 240, 241] in the Experiment to Detect the Global Epoch of Reionization Signature (EDGES) [242]. In order not to violate CMB constraints [60, 61, 243], the fraction of millicharge DM must be $f_\chi \lesssim 0.4\%$ such

CHAPTER 4. INTERACTING DM SIGNATURES ON THE CMB

that scattering saturates and *Planck* loses sensitivity [61]. Here, we include annihilation in our CMB analysis and thus *Planck* continues to have constraining power at lower f_χ ; however, we find that it does not impact the target parameter space to explain the EDGES signal [227]. Instead, the far more relevant annihilation process is from DM freezeout, constrained (for the appropriate range of DM masses) by the number of relativistic degrees of freedom N_{eff} during big bang nucleosynthesis [227, 228, 240, 241].

4.4 Discussion/Conclusions

This work explores, for the first time, the combined effects of DM scattering and annihilation on the CMB anisotropy. We identified regions of parameter space where a single effect dominates over the other effects, justifying a posteriori the approach followed in the literature to focus on a single type of interaction at a time. We additionally identify regions where both effects contribute equally and lead to new electromagnetic signatures of DM in the CMB power spectra. By considering both scattering and annihilation cross sections with power-law dependencies on the relative velocities between interacting species, we were able to determine generically in what scenarios scattering would dominate over annihilation and vice versa.

We then explored caveats to our general predictions that can exist in specific models. The first caveat we investigated was independent couplings for the scattering and annihilation cross sections, which naturally arise for dipole DM. The electric dipole leads to a $n_s = -2$ baryon scattering and the magnetic dipole leads to an s-wave annihilation. Dipole

CHAPTER 4. INTERACTING DM SIGNATURES ON THE CMB

DM was predicted and shown to be annihilation dominated. By independently varying the electric and magnetic couplings, we found when each interaction dominates over the other and if there was a region of parameter space where their combined effects lead to new signatures. We found that the transition regime between different effects dominating to be very sharp. Only in small, fine-tuned regions of parameter space did the two effects become comparable which lead to a strengthening of the constraint on the dipole couplings..

The second caveat we explored was baryon scattering saturation. Millicharge DM, a model with $n_s = -4$, was predicted and shown to be scattering dominated for $f_\chi = 1$. Naively lowering the fraction of DM that is interacting should make scattering stronger relative to annihilation, however, we demonstrated with a decreasing fraction f_χ and increasing coupling strength ϵ , the impact on the CMB power spectra can saturate. Importantly, we showed that with the addition of annihilation, the saturation effect was broken at large enough ϵ . Although the inclusion of annihilation effects broke the saturation effect, the existence of both types of DM interactions did not lead to new signatures on the CMB as the new constraint at high ϵ becomes purely an annihilation effect. Only for small regions of parameter space do we both effects as comparable which leads to very little improvement in the constraint. The two effects are non-degenerate and separable. We investigated millicharge DM with a small f_χ as it has been invoked to explain EDGES [242], however, we find that including annihilation does not impact the target parameter space to explain the signal [227].

For both models we examined, we observed that the transition between the scattering-dominated and annihilation-dominated regions were very abrupt. We also found that,

CHAPTER 4. INTERACTING DM SIGNATURES ON THE CMB

scattering and annihilation have very distinct impacts on the CMB and do not correlate nor anti-correlate. We hence prove that treating the individual effects of each interaction independently is generally as good as comparing the impact of both interactions at once. Only in small regions around the transition does a non-combined analysis break down. In the small region where both effects matter, the resultant power spectra has features that do not map directly onto the effect of a single interaction.

Despite a wealth of activity, the true nature of DM is still undetermined, with cold DM only providing a parametric description. Many suggested models include electromagnetic interaction in the form of self-annihilation and scattering. In this work we have demonstrated that in most of the parameter space, as far as the CMB anisotropy is concerned, scattering and annihilation can be studied separately since one effect usually dominates over the other. However, there exists interesting loopholes for which new signatures emerge which could be missed in analysis focusing on a single effect. To continue to explore physics beyond cold DM, this paper provides an important check for all interacting DM models.

Appendix

A.1 Benchmark models of dark matter

We describe the photon-mediated DM models we use as concrete examples in this paper.

A.1.1 Dipole dark matter

For a Dirac spin-1/2 DM particle χ with mass m_χ , the Lagrangian for electric and magnetic dipole interactions is

$$\mathcal{L}_{\text{int}} = -\frac{i}{2} \bar{\chi} \sigma_{\mu\nu} (\mathcal{M} + \gamma_5 \mathcal{D}) \chi F^{\mu\nu} , \quad (\text{A.19})$$

where \mathcal{M} and \mathcal{D} are the magnetic and electric dipole moments, $F^{\mu\nu}$ is the electromagnetic field strength and $\sigma_{\mu\nu} = \frac{i}{2} [\gamma_\mu, \gamma_\nu]$. Dipole DM interacts with SM fermions f (with electric charge Ze) through the photon.

APPENDIX

The scattering cross section between dipole DM and f is [238]

$$\sigma_{\text{MT}} = \alpha \left(\frac{2\mathcal{D}^2}{v^2} + \mathcal{M}^2 \left[3 - \frac{m_f(m_f + 4m_\chi)}{(m_f + m_\chi)^2} \right] \right) , \quad (\text{A.20})$$

where m_f is the mass of the fermion and α is the fine structure constant. We see that the electric dipole scattering cross section has a v^{-2} dependence, while the magnetic scattering cross section is independent of relative velocity. Since we are working in a nonrelativistic regime in which $v \ll 1$, we expect the electric dipole scattering cross section to dominate, for comparable values of \mathcal{D} and \mathcal{M} .

Annihilation into SM particles occurs through both the electric and magnetic dipole interaction. However, the electric dipole interaction leads to p-wave annihilation, which is subdominant to the s-wave annihilation of the magnetic dipole interaction for $v \ll 1$. While we incorporate both electric and magnetic dipole scattering in our analyses, we do not include p-wave annihilation. The s-wave annihilation cross section into f is [244]

$$\langle \sigma_{Av} \rangle = \frac{\alpha Z^2 \mathcal{M}^2}{2} \left[2 + \left(\frac{m_f}{m_\chi} \right)^2 \right] \sqrt{1 - \left(\frac{m_f}{m_\chi} \right)^2} . \quad (\text{A.21})$$

There is also scattering with and annihilation into photon. Again, we neglect these processes, since they scale with an additional factor of \mathcal{D}^2 or \mathcal{M}^2 , and we assume $\mathcal{D}, \mathcal{M} \ll 1 \text{ e cm}$.

Using the notation in Eq. (4.9), the ratio of the annihilation and scattering cross-section

APPENDIX

coefficients is

$$\frac{\sigma_A}{\sigma_S} = \frac{\mathcal{M}^2}{4\mathcal{D}^2} \left[2 + \left(\frac{m_f}{m_\chi} \right)^2 \right] \sqrt{1 - \left(\frac{m_f}{m_\chi} \right)^2} . \quad (\text{A.22})$$

A.1.2 Millicharge dark matter

Let us consider a spin-1/2 DM particle χ with mass m_χ . We assume this DM particle is millicharged: it has electromagnetic interactions with charge ϵe , where e is the standard electric charge and $\epsilon < 1$ is a free parameter. Incorporating this new particle in the SM Lagrangian, we have

$$\mathcal{L} = \mathcal{L}_{\text{SM}} + \bar{\chi} (i\not{D} - m_\chi) \chi , \quad (\text{A.23})$$

where \not{D} is the usual covariant derivative from QED. The resulting interaction term between millicharge DM and the photon is

$$\mathcal{L}_{\text{int}} = \epsilon e \bar{\chi} \gamma^\mu A_\mu \chi , \quad (\text{A.24})$$

where γ^μ are Dirac gamma matrices and A_μ is the vector field of the photon. The millicharge DM thus has all the same electromagnetic interactions as the electron, but with a coupling strength reduced by a factor of ϵ .

The scattering cross section between millicharge DM and a SM fermion f (with electric charge Ze) is given by

$$\sigma_{\text{MT},f} = \frac{2\pi Z^2 \alpha^2 \epsilon^2}{\mu_{\chi f}^2 v^4} \xi_f \quad (\text{A.25})$$

where α is the fine-structure constant and $\mu_{\chi f}$ is the reduced mass. The quantity ξ_f is

APPENDIX

due to Debye screening, which regulates the forward divergence of the differential cross section. We use the expression from previous calculations, $\xi_f = \ln(9T_b^3/4\pi\epsilon^2\alpha^3n_f)$, where T_b is the baryon fluid temperature, α is the fine structure constant, and n_e is the number density of electrons f [245]. However, this expression has been recently corrected to properly account for the plasma mass of the photon, yielding $\xi_f = \ln(T_b m_b m_\chi v / \pi \alpha n_e (m_b + m_\chi))$, where m_b is the mass of the baryons with which the DM is scattering [246]. Work in [246] suggest that the newer form of the Debye logarithm results in a momentum transfer rate at recombination that is smaller by up to a factor of 3.

The annihilation cross section $\chi\bar{\chi} \rightarrow f\bar{f}$ is

$$\langle\sigma_{Av}\rangle = \frac{\pi\alpha^2\epsilon^2}{4m_\chi^2} \sqrt{1 - \left(\frac{m_f}{m_\chi}\right)^2} \left(2 + \frac{m_f^2}{m_\chi^2}\right). \quad (\text{A.26})$$

Additionally, there is scattering with and annihilation into photons. The cross sections, however, with charged fermions scale as $\alpha^2\epsilon^2$, whereas cross sections with photons scale as $\alpha^2\epsilon^4$. Assuming $\epsilon \ll 1$, cross sections involving photons are subdominant and thus ignored, consistent with ignoring scattering with photons in the Boltzmann equations in Sec. 4.1.1.

Bibliography

- [1] D. J. Eisenstein *et al.*, “Detection of the Baryon Acoustic Peak in the Large-Scale Correlation Function of SDSS Luminous Red Galaxies,” *Astrophys. J.*, vol. 633, pp. 560–574, 2005.
- [2] G. Hinshaw *et al.*, “Five-Year Wilkinson Microwave Anisotropy Probe (WMAP) Observations: Data Processing, Sky Maps, and Basic Results,” *Astrophys. J. Suppl.*, vol. 180, pp. 225–245, 2009.
- [3] C. L. Bennett *et al.*, “Nine-Year Wilkinson Microwave Anisotropy Probe (WMAP) Observations: Final Maps and Results,” *Astrophys. J. Suppl.*, vol. 208, p. 20, 2013.
- [4] F. Beutler, C. Blake, M. Colless, D. H. Jones, L. Staveley-Smith, L. Campbell, Q. Parker, W. Saunders, and F. Watson, “The 6dF Galaxy Survey: Baryon Acoustic Oscillations and the Local Hubble Constant,” *Mon. Not. Roy. Astron. Soc.*, vol. 416, pp. 3017–3032, 2011.
- [5] C. Blake *et al.*, “The WiggleZ Dark Energy Survey: mapping the distance-redshift

BIBLIOGRAPHY

- relation with baryon acoustic oscillations,” *Mon. Not. Roy. Astron. Soc.*, vol. 418, pp. 1707–1724, 2011.
- [6] L. Anderson *et al.*, “The clustering of galaxies in the SDSS-III Baryon Oscillation Spectroscopic Survey: Baryon Acoustic Oscillations in the Data Release 9 Spectroscopic Galaxy Sample,” *Mon. Not. Roy. Astron. Soc.*, vol. 427, no. 4, pp. 3435–3467, 2013.
- [7] A. G. Riess *et al.*, “A 2.4% Determination of the Local Value of the Hubble Constant,” *Astrophys. J.*, vol. 826, no. 1, p. 56, 2016.
- [8] V. Bonvin *et al.*, “H0LiCOW – V. New COSMOGRAIL time delays of HE 0435-1223: H_0 to 3.8 per cent precision from strong lensing in a flat Λ CDM model,” *Mon. Not. Roy. Astron. Soc.*, vol. 465, no. 4, pp. 4914–4930, 2017.
- [9] P. A. R. Ade *et al.*, “Planck 2013 results. XVI. Cosmological parameters,” *Astron. Astrophys.*, vol. 571, p. A16, 2014.
- [10] ———, “Planck 2015 results. XIII. Cosmological parameters,” *Astron. Astrophys.*, vol. 594, p. A13, 2016.
- [11] B. D. Sherwin *et al.*, “Evidence for dark energy from the cosmic microwave background alone using the Atacama Cosmology Telescope lensing measurements,” *Phys. Rev. Lett.*, vol. 107, p. 021302, 2011.
- [12] A. Aghamousa, J. Hamann, and A. Shafieloo, “A non-parametric consistency test of the Λ CDM model with Planck CMB data,” *JCAP*, vol. 1709, no. 09, p. 031, 2017.

BIBLIOGRAPHY

- [13] N. Aghanim *et al.*, “Planck 2018 results. VI. Cosmological parameters,” 2018.
- [14] F. Zwicky, “On the Masses of Nebulae and of Clusters of Nebulae,” *Astrophys. J.*, vol. 86, pp. 217–246, 1937.
- [15] J. C. Kapteyn, “First Attempt at a Theory of the Arrangement and Motion of the Sidereal System,” *Astrophys. J.*, vol. 55, pp. 302–328, 1922.
- [16] V. C. Rubin and W. K. Ford, Jr., “Rotation of the Andromeda Nebula from a Spectroscopic Survey of Emission Regions,” *Astrophys. J.*, vol. 159, pp. 379–403, 1970.
- [17] V. C. Rubin, N. Thonnard, and W. K. Ford, Jr., “Rotational properties of 21 SC galaxies with a large range of luminosities and radii, from NGC 4605 / $R = 4\text{kpc}$ / to UGC 2885 / $R = 122\text{kpc}$ /,” *Astrophys. J.*, vol. 238, p. 471, 1980.
- [18] M. Persic, P. Salucci, and F. Stel, “The Universal rotation curve of spiral galaxies: 1. The Dark matter connection,” *Mon. Not. Roy. Astron. Soc.*, vol. 281, p. 27, 1996.
- [19] S. Perlmutter *et al.*, “Measurements of Omega and Lambda from 42 high redshift supernovae,” *Astrophys. J.*, vol. 517, pp. 565–586, 1999.
- [20] A. G. Riess *et al.*, “Observational evidence from supernovae for an accelerating universe and a cosmological constant,” *Astron. J.*, vol. 116, pp. 1009–1038, 1998.
- [21] R. R. Caldwell and M. Kamionkowski, “The Physics of Cosmic Acceleration,” *Ann. Rev. Nucl. Part. Sci.*, vol. 59, pp. 397–429, 2009.
- [22] J. Martin, “Everything You Always Wanted To Know About The Cosmological Con-

BIBLIOGRAPHY

- stant Problem (But Were Afraid To Ask),” *Comptes Rendus Physique*, vol. 13, pp. 566–665, 2012.
- [23] R. A. Flores and J. R. Primack, “Observational and theoretical constraints on singular dark matter halos,” *Astrophys. J.*, vol. 427, pp. L1–4, 1994.
- [24] B. Moore, “Evidence against dissipationless dark matter from observations of galaxy haloes,” *Nature*, vol. 370, p. 629, 1994.
- [25] J. D. Simon, A. D. Bolatto, A. Leroy, L. Blitz, and E. L. Gates, “High-resolution measurements of the halos of four dark matter-dominated galaxies: Deviations from a universal density profile,” *Astrophys. J.*, vol. 621, pp. 757–776, 2005.
- [26] J. I. Read, M. I. Wilkinson, N. W. Evans, G. Gilmore, and J. T. Kleyna, “The importance of tides for the local group dwarf spheroidals,” *Mon. Not. Roy. Astron. Soc.*, vol. 367, pp. 387–399, 2006.
- [27] M. Boylan-Kolchin, J. S. Bullock, and M. Kaplinghat, “Too big to fail? The puzzling darkness of massive Milky Way subhaloes,” *Mon. Not. Roy. Astron. Soc.*, vol. 415, p. L40, 2011.
- [28] B. Moore, S. Ghigna, F. Governato, G. Lake, T. R. Quinn, J. Stadel, and P. Tozzi, “Dark matter substructure within galactic halos,” *Astrophys. J.*, vol. 524, pp. L19–L22, 1999.
- [29] A. A. Klypin, A. V. Kravtsov, O. Valenzuela, and F. Prada, “Where are the missing Galactic satellites?” *Astrophys. J.*, vol. 522, pp. 82–92, 1999.

BIBLIOGRAPHY

- [30] D. N. Spergel and P. J. Steinhardt, “Observational evidence for selfinteracting cold dark matter,” *Phys. Rev. Lett.*, vol. 84, pp. 3760–3763, 2000.
- [31] R. Foot, “Mirror matter-type dark matter,” *Int. J. Mod. Phys.*, vol. D13, pp. 2161–2192, 2004.
- [32] J. I. Read and G. Gilmore, “Mass loss from dwarf spheroidal galaxies: The Origins of shallow dark matter cores and exponential surface brightness profiles,” *Mon. Not. Roy. Astron. Soc.*, vol. 356, pp. 107–124, 2005.
- [33] S. Mashchenko, J. Wadsley, and H. M. P. Couchman, “Stellar Feedback in Dwarf Galaxy Formation,” *Science*, vol. 319, p. 174, 2008.
- [34] A. Pontzen and F. Governato, “How supernova feedback turns dark matter cusps into cores,” *Mon. Not. Roy. Astron. Soc.*, vol. 421, p. 3464, 2012.
- [35] A. Di Cintio, C. B. Brook, A. V. Macciò, G. S. Stinson, A. Knebe, A. A. Dutton, and J. Wadsley, “The dependence of dark matter profiles on the stellar-to-halo mass ratio: a prediction for cusps versus cores,” *Mon. Not. Roy. Astron. Soc.*, vol. 437, no. 1, pp. 415–423, 2014.
- [36] T. K. Chan, D. Kereš, J. Oñorbe, P. F. Hopkins, A. L. Muratov, C. A. Faucher-Giguère, and E. Quataert, “The impact of baryonic physics on the structure of dark matter haloes: the view from the FIRE cosmological simulations,” *Mon. Not. Roy. Astron. Soc.*, vol. 454, no. 3, pp. 2981–3001, 2015.
- [37] J. S. Bullock, “Notes on the Missing Satellites Problem,” 2010.

BIBLIOGRAPHY

- [38] A. M. Brooks, M. Kuhlen, A. Zolotov, and D. Hooper, “A Baryonic Solution to the Missing Satellites Problem,” *Astrophys. J.*, vol. 765, p. 22, 2013.
- [39] S. Y. Kim, A. H. G. Peter, and J. R. Hargis, “Missing Satellites Problem: Completeness Corrections to the Number of Satellite Galaxies in the Milky Way are Consistent with Cold Dark Matter Predictions,” *Phys. Rev. Lett.*, vol. 121, no. 21, p. 211302, 2018.
- [40] D. N. Pfeffer, E. D. Kovetz, and M. Kamionkowski, “Ultrahigh-energy cosmic ray hotspots from tidal disruption events,” *Mon. Not. Roy. Astron. Soc.*, vol. 466, no. 3, pp. 2922–2926, 2017.
- [41] M. J. Rees, “Tidal disruption of stars by black holes of 10 to the 6th–10 to the 8th solar masses in nearby galaxies,” *Nature*, vol. 333, pp. 523–528, 1988.
- [42] D. N. Pfeffer, P. C. Breysse, and G. Stein, “Deconfusing intensity maps with neural networks,” 2019.
- [43] R. U. Abbasi *et al.*, “Indications of Intermediate-Scale Anisotropy of Cosmic Rays with Energy Greater Than 57 EeV in the Northern Sky Measured with the Surface Detector of the Telescope Array Experiment,” *Astrophys. J.*, vol. 790, p. L21, 2014.
- [44] A. Aab *et al.*, “Searches for Anisotropies in the Arrival Directions of the Highest Energy Cosmic Rays Detected by the Pierre Auger Observatory,” *Astrophys. J.*, vol. 804, no. 1, p. 15, 2015.
- [45] K. Greisen, “End to the cosmic ray spectrum?” *Phys. Rev. Lett.*, vol. 16, pp. 748–750,

BIBLIOGRAPHY

- 1966.
- [46] G. T. Zatsepin and V. A. Kuz'min, "Upper Limit of the Spectrum of Cosmic Rays," *Soviet Journal of Experimental and Theoretical Physics Letters*, vol. 4, p. 78, Aug. 1966.
- [47] E. Waxman and J. Miralda-Escude, "Images of bursting sources of high-energy cosmic rays. 1. Effects of magnetic fields," *Astrophys. J.*, vol. 472, pp. L89–L92, 1996.
- [48] J. Abraham *et al.*, "Correlation of the highest energy cosmic rays with nearby extragalactic objects," *Science*, vol. 318, pp. 938–943, 2007.
- [49] I. Zaw, G. R. Farrar, and J. E. Greene, "Galaxies Correlating with Ultra-high Energy Cosmic Rays," *Astrophys. J.*, vol. 696, pp. 1218–1229, 2009.
- [50] E. Waxman, "Cosmological gamma-ray bursts and the highest energy cosmic rays," *Phys. Rev. Lett.*, vol. 75, pp. 386–389, 1995.
- [51] N. C. Stone and B. D. Metzger, "Rates of Stellar Tidal Disruption as Probes of the Supermassive Black Hole Mass Function," *Mon. Not. Roy. Astron. Soc.*, vol. 455, no. 1, pp. 859–883, 2016.
- [52] G. R. Farrar and T. Piran, "Tidal disruption jets as the source of Ultra-High Energy Cosmic Rays," 2014.
- [53] E. D. Kovetz *et al.*, "Line-Intensity Mapping: 2017 Status Report," 2017.
- [54] T. Y. Li, R. H. Wechsler, K. Devaraj, and S. E. Church, "Connecting CO Intensity

BIBLIOGRAPHY

- Mapping to Molecular Gas and Star Formation in the Epoch of Galaxy Assembly,” *ApJ*, vol. 817, p. 169, Feb. 2016.
- [55] H. T. Ihle *et al.*, “Joint power spectrum and voxel intensity distribution forecast on the CO luminosity function with COMAP,” *Astrophys. J.*, vol. 871, no. 1, p. 75, 2019.
- [56] X.-l. Chen, S. Hannestad, and R. J. Scherrer, “Cosmic microwave background and large scale structure limits on the interaction between dark matter and baryons,” *Phys. Rev.*, vol. D65, p. 123515, 2002.
- [57] C. Dvorkin, K. Blum, and M. Kamionkowski, “Constraining Dark Matter-Baryon Scattering with Linear Cosmology,” *Phys. Rev.*, vol. D89, no. 2, p. 023519, 2014.
- [58] V. Gluscevic and K. K. Boddy, “Constraints on Scattering of keV–TeV Dark Matter with Protons in the Early Universe,” *Phys. Rev. Lett.*, vol. 121, no. 8, p. 081301, 2018.
- [59] K. K. Boddy and V. Gluscevic, “First Cosmological Constraint on the Effective Theory of Dark Matter-Proton Interactions,” *Phys. Rev.*, vol. D98, no. 8, p. 083510, 2018.
- [60] W. L. Xu, C. Dvorkin, and A. Chael, “Probing sub-GeV Dark Matter-Baryon Scattering with Cosmological Observables,” *Phys. Rev.*, vol. D97, no. 10, p. 103530, 2018.
- [61] K. K. Boddy, V. Gluscevic, V. Poulin, E. D. Kovetz, M. Kamionkowski, and R. Barkana, “Critical assessment of CMB limits on dark matter-baryon scattering: New treatment of the relative bulk velocity,” *Phys. Rev.*, vol. D98, no. 12, p. 123506, 2018.

BIBLIOGRAPHY

- [62] X.-L. Chen and M. Kamionkowski, “Particle decays during the cosmic dark ages,” *Phys. Rev.*, vol. D70, p. 043502, 2004.
- [63] N. Padmanabhan and D. P. Finkbeiner, “Detecting dark matter annihilation with CMB polarization: Signatures and experimental prospects,” *Phys.Rev.*, vol. D72, p. 023508, 2005.
- [64] A. V. Belikov and D. Hooper, “How Dark Matter Reionized The Universe,” *Phys.Rev.*, vol. D80, p. 035007, 2009.
- [65] M. Cirelli, F. Iocco, and P. Panci, “Constraints on Dark Matter annihilations from reionization and heating of the intergalactic gas,” *JCAP*, vol. 0910, p. 009, 2009.
- [66] G. Huetsi, A. Hektor, and M. Raidal, “Constraints on leptonically annihilating Dark Matter from reionization and extragalactic gamma background,” *Astron. Astrophys.*, vol. 505, pp. 999–1005, 2009.
- [67] T. R. Slatyer, N. Padmanabhan, and D. P. Finkbeiner, “CMB Constraints on WIMP Annihilation: Energy Absorption During the Recombination Epoch,” *Phys.Rev.*, vol. D80, p. 043526, 2009.
- [68] A. Natarajan and D. J. Schwarz, “The effect of early dark matter halos on reionization,” *Phys.Rev.*, vol. D78, p. 103524, 2008.
- [69] —, “Dark matter annihilation and its effect on CMB and Hydrogen 21 cm observations,” *Phys.Rev.*, vol. D80, p. 043529, 2009.

BIBLIOGRAPHY

- [70] —, “Distinguishing standard reionization from dark matter models,” *Phys.Rev.*, vol. D81, p. 123510, 2010.
- [71] M. Valdes, C. Evoli, and A. Ferrara, “Particle energy cascade in the Intergalactic Medium,” *Mon. Not. Roy. Astron. Soc.*, vol. 404, pp. 1569–1582, 2010.
- [72] C. Evoli, M. Valdes, A. Ferrara, and N. Yoshida, “Energy deposition by weakly interacting massive particles: a comprehensive study,” *Mon. Not. Roy. Astron. Soc.*, vol. 422, pp. 420–433, 2012.
- [73] S. Galli, T. R. Slatyer, M. Valdes, and F. Iocco, “Systematic Uncertainties In Constraining Dark Matter Annihilation From The Cosmic Microwave Background,” *Phys.Rev.*, vol. D88, p. 063502, 2013.
- [74] D. P. Finkbeiner, S. Galli, T. Lin, and T. R. Slatyer, “Searching for Dark Matter in the CMB: A Compact Parameterization of Energy Injection from New Physics,” *Phys.Rev.*, vol. D85, p. 043522, 2012.
- [75] G. Hutsi, J. Chluba, A. Hektor, and M. Raidal, “WMAP7 and future CMB constraints on annihilating dark matter: implications on GeV-scale WIMPs,” *Astron. Astrophys.*, vol. 535, p. A26, 2011.
- [76] T. R. Slatyer, “Energy Injection And Absorption In The Cosmic Dark Ages,” *Phys.Rev.*, vol. D87, no. 12, p. 123513, 2013.
- [77] G. Giesen, J. Lesgourgues, B. Audren, and Y. Ali-Haïmoud, “CMB photons shedding light on dark matter,” *JCAP*, vol. 1212, p. 008, 2012.

BIBLIOGRAPHY

- [78] S. Galli, T. R. Slatyer, M. Valdes, and F. Iocco, “Systematic Uncertainties In Constraining Dark Matter Annihilation From The Cosmic Microwave Background,” *Phys.Rev.*, vol. D88, p. 063502, 2013.
- [79] T. R. Slatyer, “Indirect Dark Matter Signatures in the Cosmic Dark dAges I. Generalizing the Bound on s-wave Dark Matter Annihilation from Planck,” 2015.
- [80] L. Lopez-Honorez, O. Mena, S. Palomares-Ruiz, and A. C. Vincent, “Constraints on dark matter annihilation from CMB observations before Planck,” *JCAP*, vol. 1307, p. 046, 2013.
- [81] V. Poulin, P. D. Serpico, and J. Lesgourgues, “Dark Matter annihilations in halos and high-redshift sources of reionization of the universe,” *JCAP*, vol. 1512, no. 12, p. 041, 2015.
- [82] H. Liu, T. R. Slatyer, and J. Zavala, “Contributions to cosmic reionization from dark matter annihilation and decay,” *Phys. Rev.*, vol. D94, no. 6, p. 063507, 2016.
- [83] P. Stöcker, M. Krämer, J. Lesgourgues, and V. Poulin, “Exotic energy injection with ExoCLASS: Application to the Higgs portal model and evaporating black holes,” *JCAP*, vol. 1803, no. 03, p. 018, 2018.
- [84] G. R. Farrar and A. Gruzinov, “Giant AGN Flares and Cosmic Ray Bursts,” *Astrophys. J.*, vol. 693, pp. 329–332, 2009.
- [85] M.-P. Véron-Cetty and P. Véron, “A catalogue of quasars and active nuclei: 13th edition,” *A&A*, vol. 518, p. A10, Jul. 2010.

BIBLIOGRAPHY

- [86] H.-N. He, A. Kusenko, S. Nagataki, B.-B. Zhang, R.-Z. Yang, and Y.-Z. Fan, “Monte Carlo Bayesian search for the plausible source of the Telescope Array hotspot,” *Phys. Rev.*, vol. D93, p. 043011, 2016.
- [87] I. D. Karachentsev and O. G. Kashibadze, “Total masses of the local group and m81 group derived from the local hubble flow,” *Submitted to: Astrophysics*, 2005.
- [88] N. Gaffney, D. Lester, and C. Telesco, “Kinematics of the stars in the starburst nucleus of M82: just another normal stellar bulge?” *Rev. Mexicana Astron. Astrofis.*, vol. 27, pp. 137–140, Nov. 1993.
- [89] G. L. H. Harris, “NGC 5128: The Giant Beneath,” *Publ. Astron. Soc. Austral.*, vol. 27, p. 475, 2010.
- [90] K. Fang, T. Fujii, T. Linden, and A. V. Olinto, “Is the Ultra-High Energy Cosmic-Ray Excess Observed by the Telescope Array Correlated with IceCube Neutrinos?” *Astrophys. J.*, vol. 794, no. 2, p. 126, 2014.
- [91] M. D. Kistler, T. Stanev, and H. Yüksel, “Cosmic PeV Neutrinos and the Sources of Ultrahigh Energy Protons,” *Phys. Rev.*, vol. D90, no. 12, p. 123006, 2014.
- [92] A. Aab *et al.*, “The Pierre Auger Observatory: Contributions to the 33rd International Cosmic Ray Conference (ICRC 2013),” in *Proceedings, 33rd International Cosmic Ray Conference (ICRC2013): Rio de Janeiro, Brazil, July 2-9, 2013*, 2013. [Online]. Available: <http://lss.fnal.gov/archive/2013/conf/fermilab-conf-13-285-ad-ae-cd-td.pdf>

BIBLIOGRAPHY

- [93] T. Abu-Zayyad *et al.*, “The Cosmic Ray Energy Spectrum Observed with the Surface Detector of the Telescope Array Experiment,” *Astrophys. J.*, vol. 768, p. L1, 2013.
- [94] P. Abreu *et al.*, “Update on the Correlation of the Highest Energy Cosmic Rays with Nearby Extragalactic matter,” *Astropart. Phys.*, vol. 34, pp. 314–326, 2010.
- [95] M. C. Beck, A. M. Beck, R. Beck, K. Dolag, A. W. Strong, and P. Nielaba, “New constraints on modelling the random magnetic field of the MW,” *JCAP*, vol. 1605, no. 05, p. 056, 2016.
- [96] G. R. Farrar, “The Galactic Magnetic Field and Ultrahigh-Energy Cosmic Ray Deflections,” *Comptes Rendus Physique*, vol. 15, pp. 339–348, 2014.
- [97] K. Kotera and A. V. Olinto, “The Astrophysics of Ultrahigh Energy Cosmic Rays,” *Ann. Rev. Astron. Astrophys.*, vol. 49, pp. 119–153, 2011.
- [98] D. Dzanovic, A. J. Benson, C. S. Frenk, and R. Sharples, “Luminosity and stellar mass functions of disks and spheroids in the SDSS and the supermassive black hole mass function,” *Mon. Not. Roy. Astron. Soc.*, vol. 379, pp. 841–866, 2007.
- [99] L. I. Caramete and P. L. Biermann, “The mass function of nearby black hole candidates,” *Astron. Astrophys.*, vol. 521, p. A55, 2010.
- [100] J. Magorrian and S. Tremaine, “Rates of tidal disruption of stars by massive central black holes,” *Mon. Not. Roy. Astron. Soc.*, vol. 309, p. 447, 1999.
- [101] A. Aab *et al.*, “Depth of maximum of air-shower profiles at the Pierre Auger Observatory. II. Composition implications,” *Phys. Rev.*, vol. D90, no. 12, p. 122006, 2014.

BIBLIOGRAPHY

- [102] A. M. Ghez *et al.*, “Measuring Distance and Properties of the Milky Way’s Central Supermassive Black Hole with Stellar Orbits,” *Astrophys. J.*, vol. 689, pp. 1044–1062, 2008.
- [103] A. Patruno, S. F. P. Zwart, J. Dewi, and C. Hopman, “The ultraluminous x-ray source in m82: an intermediate mass black hole with a giant companion,” *Mon. Not. Roy. Astron. Soc.*, vol. 370, pp. L6–L9, 2006.
- [104] D. R. Pasham, T. E. Strohmayer, and R. F. Mushotzky, “A 400 solar mass black hole in the Ultraluminous X-ray source M82 X-1 accreting close to its Eddington limit,” 2015, [Nature513,74(2014)].
- [105] H. B. Perets, C. Hopman, and T. Alexander, “Massive perturber-driven interactions of stars with a massive black hole,” *Astrophys. J.*, vol. 656, pp. 709–720, 2007.
- [106] J. R. Pritchard and A. Loeb, “21 cm cosmology in the 21st century,” *Reports on Progress in Physics*, vol. 75, p. 086901, Aug 2012.
- [107] K. W. Masui, E. R. Switzer, N. Banavar, K. Bandura, C. Blake, L.-M. Calin, T.-C. Chang, X. Chen, Y.-C. Li, Y.-W. Liao, A. Natarajan, U.-L. Pen, J. B. Peterson, J. R. Shaw, and T. C. Voytek, “Measurement of 21 cm Brightness Fluctuations at $z \sim 0.8$ in Cross-correlation,” *ApJ*, vol. 763, p. L20, Jan. 2013.
- [108] E. R. Switzer *et al.*, “Determination of $z \sim 0.8$ neutral hydrogen fluctuations using the 21 cm intensity mapping auto-correlation,” *Mon. Not. Roy. Astron. Soc.*, vol. 434, p. L46, 2013.

BIBLIOGRAPHY

- [109] C. J. Anderson *et al.*, “Low-amplitude clustering in low-redshift 21-cm intensity maps cross-correlated with 2dF galaxy densities,” *Mon. Not. Roy. Astron. Soc.*, vol. 476, no. 3, pp. 3382–3392, 2018.
- [110] S. J. Tingay, R. Goeke, J. D. Bowman, D. Emrich, S. M. Ord, D. A. Mitchell, M. F. Morales, T. Booler, B. Crosse, R. B. Wayth, C. J. Lonsdale, S. Tremblay, D. Palot, T. Colegate, A. Wicenec, N. Kudryavtseva, W. Arcus, D. Barnes, G. Bernardi, F. Briggs, S. Burns, J. D. Bunton, R. J. Cappallo, B. E. Corey, A. Deshpande, L. Desouza, B. M. Gaensler, L. J. Greenhill, P. J. Hall, B. J. Hazelton, D. Herne, J. N. Hewitt, M. Johnston-Hollitt, D. L. Kaplan, J. C. Kasper, B. B. Kincaid, R. Koenig, E. Kratzenberg, M. J. Lynch, B. Mckinley, S. R. Mcwhirter, E. Morgan, D. Oberoi, J. Pathikulangara, T. Prabu, R. A. Remillard, A. E. E. Rogers, A. Roshi, J. E. Salah, R. J. Sault, N. Udaya-Shankar, F. Schlagenhauser, K. S. Srivani, J. Stevens, R. Subrahmanyan, M. Waterson, R. L. Webster, A. R. Whitney, A. Williams, C. L. Williams, and J. S. B. Wyithe, “The Murchison Widefield Array: The Square Kilometre Array Precursor at Low Radio Frequencies,” *PASA*, vol. 30, p. e007, Jan. 2013.
- [111] M. P. van Haarlem, M. W. Wise, A. W. Gunst, G. Heald, J. P. McKean, J. W. T. Hessels, A. G. de Bruyn, R. Nijboer, J. Swinbank, R. Fallows, M. Brentjens, A. Nelles, R. Beck, H. Falcke, R. Fender, J. Hörandel, L. V. E. Koopmans, G. Mann, G. Miley, H. Röttgering, B. W. Stappers, R. A. M. J. Wijers, S. Zaroubi, M. van den Akker, A. Alexov, J. Anderson, K. Anderson, A. van Ardenne, M. Arts, A. Asgekar, I. M. Avruch, F. Batejat, L. Bähren, M. E. Bell, M. R. Bell, I. van Bemmelen, P. Bennema, M. J. Bentum, G. Bernardi, P. Best, L. Bîrzan, A. Bonafede, A.-J. Boonstra, R. Braun,

BIBLIOGRAPHY

J. Bregman, F. Breitling, R. H. van de Brink, J. Broderick, P. C. Broekema, W. N. Brouw, M. Brüggén, H. R. Butcher, W. van Cappellen, B. Ciardi, T. Coenen, J. Conway, A. Coolen, A. Corstanje, S. Damstra, O. Davies, A. T. Deller, R.-J. Dettmar, G. van Diepen, K. Dijkstra, P. Donker, A. Doorduyn, J. Dromer, M. Drost, A. van Duin, J. Eislöffel, J. van Enst, C. Ferrari, W. Frieswijk, H. Gankema, M. A. Garrett, F. de Gasperin, M. Gerbers, E. de Geus, J.-M. Grießmeier, T. Grit, P. Gruppen, J. P. Hamaker, T. Hassall, M. Hoeft, H. A. Holties, A. Horneffer, A. van der Horst, A. van Houwelingen, A. Huijgen, M. Iacobelli, H. Intema, N. Jackson, V. Jelic, A. de Jong, E. Juetten, D. Kant, A. Karastergiou, A. Koers, H. Kollen, V. I. Kondratiev, E. Kooistra, Y. Koopman, A. Koster, M. Kuniyoshi, M. Kramer, G. Kuper, P. Lambropoulos, C. Law, J. van Leeuwen, J. Lemaitre, M. Loose, P. Maat, G. Macario, S. Markoff, J. Masters, R. A. McFadden, D. McKay-Bukowski, H. Meijering, H. Meulman, M. Mevius, E. Middelberg, R. Millenaar, J. C. A. Miller-Jones, R. N. Mohan, J. D. Mol, J. Morawietz, R. Morganti, D. D. Mulcahy, E. Mulder, H. Munk, L. Nieuwenhuis, R. van Nieuwpoort, J. E. Noordam, M. Norden, A. Noutsos, A. R. Offringa, H. Olofsson, A. Omar, E. Orrú, R. Overeem, H. Paas, M. Pandey-Pommier, V. N. Pandey, R. Pizzo, A. Polatidis, D. Rafferty, S. Rawlings, W. Reich, J.-P. de Reijer, J. Reitsma, G. A. Renting, P. Riemers, E. Rol, J. W. Romein, J. Roosjen, M. Ruiter, A. Scaife, K. van der Schaaf, B. Scheers, P. Schellart, A. Schoenmakers, G. Schoonderbeek, M. Serylak, A. Shulevski, J. Sluman, O. Smirnov, C. Sobey, H. Spreeuw, M. Steinmetz, C. G. M. Sterks, H.-J. Stiepel, K. Stuurwold, M. Tagger, Y. Tang, C. Tasse, I. Thomas, S. Thoudam, M. C. Toribio, B. van der Tol,

BIBLIOGRAPHY

- O. Usov, M. van Veelen, A.-J. van der Veen, S. ter Veen, J. P. W. Verbiest, R. Vermeulen, N. Vermaas, C. Vocks, C. Vogt, M. de Vos, E. van der Wal, R. van Weeren, H. Weggemans, P. Weltevrede, S. White, S. J. Wijnholds, T. Wilhelmsson, O. Wucknitz, S. Yatawatta, P. Zarka, A. Zensus, and J. van Zwieten, “LOFAR: The LOW-Frequency ARray,” *A&A*, vol. 556, p. A2, Aug. 2013.
- [112] K. Bandura *et al.*, “Canadian Hydrogen Intensity Mapping Experiment (CHIME) Pathfinder,” *Proc. SPIE Int. Soc. Opt. Eng.*, vol. 9145, p. 22, 2014.
- [113] Z. S. Ali *et al.*, “PAPER-64 Constraints on Reionization: The 21cm Power Spectrum at $z=8.4$,” *Astrophys. J.*, vol. 809, no. 1, p. 61, 2015.
- [114] Y. Xu, X. Wang, and X. Chen, “Forecasts on the Dark Energy and Primordial Non-Gaussianity Observations with the Tianlai Cylinder Array,” *ApJ*, vol. 798, p. 40, Jan. 2015.
- [115] L. B. Newburgh, K. Bandura, M. A. Bucher, T.-C. Chang, H. C. Chiang, J. F. Cliche, R. Davé, M. Dobbs, C. Clarkson, K. M. Ganga, T. Gogo, A. Gumba, N. Gupta, M. Hilton, B. Johnstone, A. Karastergiou, M. Kunz, D. Lokhorst, R. Maartens, S. Macpherson, M. Mdlalose, K. Moodley, L. Ngwenya, J. M. Parra, J. Peterson, O. Recnik, B. Saliwanchik, M. G. Santos, J. L. Sievers, O. Smirnov, P. Stronkhorst, R. Taylor, K. Vanderlinde, G. Van Vuuren, A. Weltman, and A. Witzemann, “HIRAX: a probe of dark energy and radio transients,” in *Ground-based and Airborne Telescopes VI*, ser. Proc. SPIE, vol. 9906, Aug. 2016, p. 99065X.
- [116] D. R. DeBoer *et al.*, “Hydrogen Epoch of Reionization Array (HERA),” *Publ. Astron.*

BIBLIOGRAPHY

- Soc. Pac.*, vol. 129, no. 974, p. 045001, 2017.
- [117] R. A. C. Croft, J. Miralda-Escudé, Z. Zheng, M. Blomqvist, and M. Pieri, “Intensity mapping with SDSS/BOSS Lyman- α emission, quasars, and their Lyman- α forest,” *Mon. Not. Roy. Astron. Soc.*, vol. 481, no. 1, pp. 1320–1336, 2018.
- [118] A. R. Pullen, P. Serra, T.-C. Chang, O. Doré, and S. Ho, “Search for C II emission on cosmological scales at redshift $Z \sim 2.6$,” *MNRAS*, vol. 478, no. 2, pp. 1911–1924, Aug 2018.
- [119] S. Yang, A. R. Pullen, and E. R. Switzer, “Evidence for CII diffuse line emission at redshift $z \sim 2.6$,” *arXiv e-prints*, p. arXiv:1904.01180, Apr 2019.
- [120] G. K. Keating, D. P. Marrone, G. C. Bower, E. Leitch, J. E. Carlstrom, and D. R. DeBoer, “COPSS II: The Molecular Gas Content of Ten Million Cubic Megaparsecs at Redshift $z \sim 3$,” *ApJ*, vol. 830, p. 34, Oct. 2016.
- [121] E. D. Kovetz, P. C. Breysse, A. Lidz, J. Bock, C. M. Bradford, T.-C. Chang, S. Foreman, H. Padmanabhan, A. Pullen, D. Riechers, M. B. Silva, and E. Switzer, “Astrophysics and Cosmology with Line-Intensity Mapping,” *arXiv e-prints*, p. arXiv:1903.04496, Mar 2019.
- [122] G. J. Hill *et al.*, “The Hobby-Eberly Telescope Dark Energy Experiment (HETDEX): Description and Early Pilot Survey Results,” *ASP Conf. Ser.*, vol. 399, pp. 115–118, 2008.
- [123] A. T. Crites, J. J. Bock, C. M. Bradford, T. C. Chang, A. R. Cooray, L. Duband,

BIBLIOGRAPHY

- Y. Gong, S. Hailey-Dunsheath, J. Hunacek, P. M. Koch, C. T. Li, R. C. O’Brien, T. Prouve, E. Shirokoff, M. B. Silva, Z. Staniszewski, B. Uzgil, and M. Zemcov, “The TIME-Pilot intensity mapping experiment,” in *Millimeter, Submillimeter, and Far-Infrared Detectors and Instrumentation for Astronomy VII*, ser. Proc. SPIE, vol. 9153, Aug. 2014, p. 91531W.
- [124] O. Doré *et al.*, “Cosmology with the SPHEREX All-Sky Spectral Survey,” 2014.
- [125] G. C. Bower, G. K. Keating, D. P. Marrone, and S. T. YT Lee Array Team, “Cosmic Structure and Galaxy Evolution through Intensity Mapping of Molecular Gas,” vol. 227, p. 426.04, Jan. 2016.
- [126] A. Cooray *et al.*, “Cosmic Dawn Intensity Mapper,” 2016.
- [127] J. Aguirre and STARFIRE Collaboration, “STARFIRE: The Spectroscopic Terahertz Airborne Receiver for Far-InfraRed Exploration,” in *American Astronomical Society Meeting Abstracts #231*, ser. American Astronomical Society Meeting Abstracts, vol. 231, Jan. 2018, p. 328.04.
- [128] G. Lagache, “Exploring the dusty star-formation in the early Universe using intensity mapping,” in *Peering towards Cosmic Dawn*, ser. IAU Symposium, V. Jelić and T. van der Hulst, Eds., vol. 333, May 2018, pp. 228–233.
- [129] H. Padmanabhan, “Constraining the evolution of CII intensity through the end stages of reionization,” 2018.
- [130] G. J. Stacey, M. Aravena, K. Basu, N. Battaglia, B. Beringue, F. Bertoldi, J. R. Bond,

BIBLIOGRAPHY

- P. Breyse, R. Bustos, S. Chapman, D. T. Chung, N. Cothard, J. Erler, M. Fich, S. Foreman, P. Gallardo, R. Giovanelli, U. U. Graf, M. P. Haynes, R. Herrera-Camus, T. L. Herter, R. Hložek, D. Johnstone, L. Keating, B. Magnelli, D. Meerburg, J. Meyers, N. Murray, M. Niemack, T. Nikola, M. Nolta, S. C. Parshley, D. A. Riechers, P. Schilke, D. Scott, G. Stein, J. Stevens, J. Stutzki, E. M. Vavagiakis, and M. P. Viero, “CCAT-Prime: science with an ultra-widefield submillimeter observatory on Cerro Chajnantor,” in *Ground-based and Airborne Telescopes VII*, ser. Society of Photo-Optical Instrumentation Engineers (SPIE) Conference Series, vol. 10700, Jul 2018, p. 107001M.
- [131] G. Popping, D. Narayanan, R. S. Somerville, A. L. Faisst, and M. R. Krumholz, “The art of modelling CO, [C I], and [C II] in cosmological galaxy formation models,” *MNRAS*, vol. 482, pp. 4906–4932, Feb. 2019.
- [132] P. C. Breyse, E. D. Kovetz, P. S. Behroozi, L. Dai, and M. Kamionkowski, “Insights from probability distribution functions of intensity maps,” *Mon. Not. Roy. Astron. Soc.*, vol. 467, no. 3, pp. 2996–3010, 2017.
- [133] A. Lidz, S. R. Furlanetto, S. P. Oh, J. Aguirre, T.-C. Chang, O. Doré, and J. R. Pritchard, “Intensity Mapping with Carbon Monoxide Emission Lines and the Redshifted 21 cm Line,” *ApJ*, vol. 741, p. 70, Nov. 2011.
- [134] P. C. Breyse and R. M. Alexandroff, “Observing AGN feedback with CO intensity mapping,” *arXiv e-prints*, Apr 2019.
- [135] M. F. Morales and J. S. B. Wyithe, “Reionization and Cosmology with 21-cm Fluc-

BIBLIOGRAPHY

- tuations,” *ARA&A*, vol. 48, pp. 127–171, Sep. 2010.
- [136] L. Wolz, F. B. Abdalla, D. Alonso, C. Blake, P. Bull, T. C. Chang, P. Ferreira, C. Y. Kuo, M. Santos, and J. R. Shaw, “Foreground Subtraction in Intensity Mapping with the SKA,” in *Advancing Astrophysics with the Square Kilometre Array (AASKA14)*, Apr 2015, p. 35.
- [137] G. Sun, L. Moncelsi, M. P. Viero, M. B. Silva, J. Bock, C. M. Bradford, T. C. Chang, Y. T. Cheng, A. R. Cooray, A. Crites, S. Hailey-Dunsheath, B. Uzgil, J. R. Hunacek, and M. Zemcov, “A Foreground Masking Strategy for [C II] Intensity Mapping Experiments Using Galaxies Selected by Stellar Mass and Redshift,” *ApJ*, vol. 856, no. 2, p. 107, Apr 2018.
- [138] E. R. Switzer, C. J. Anderson, A. R. Pullen, and S. Yang, “Intensity Mapping in the Presence of Foregrounds and Correlated Continuum Emission,” *ApJ*, vol. 872, no. 1, p. 82, Feb 2019.
- [139] M. Ntampaka, C. Avestruz, S. Boada, J. Caldeira, J. Cisewski-Kehe, R. Di Stefano, C. Dvorkin, A. E. Evrard, A. Farahi, D. Finkbeiner, S. Genel, A. Goodman, A. Goulding, S. Ho, A. Kosowsky, P. La Plante, F. Lanusse, M. Lochner, R. Mandelbaum, D. Nagai, J. A. Newman, B. Nord, J. E. G. Peek, A. Peel, B. Poczos, M. M. Rau, A. Siemiginowska, D. J. Sutherland, H. Trac, and B. Wandelt, “The Role of Machine Learning in the Next Decade of Cosmology,” *arXiv e-prints*, p. arXiv:1902.10159, Feb 2019.
- [140] S. Ravanbakhsh, J. Oliva, S. Fromenteau, L. C. Price, S. Ho, J. Schneider, and B. Poc-

BIBLIOGRAPHY

- zos, “Estimating Cosmological Parameters from the Dark Matter Distribution,” *arXiv e-prints*, p. arXiv:1711.02033, Nov 2017.
- [141] H. Shimabukuro and B. Semelin, “Analysing the 21 cm signal from the epoch of reionization with artificial neural networks,” *MNRAS*, vol. 468, no. 4, pp. 3869–3877, Jul 2017.
- [142] C. J. Schmit and J. R. Pritchard, “Emulation of reionization simulations for Bayesian inference of astrophysics parameters using neural networks,” *MNRAS*, vol. 475, no. 1, pp. 1213–1223, Mar 2018.
- [143] N. Gillet, A. Mesinger, B. Greig, A. Liu, and G. Ucci, “Deep learning from 21-cm tomography of the cosmic dawn and reionization,” *MNRAS*, vol. 484, no. 1, pp. 282–293, Mar 2019.
- [144] D. Ribli, B. Ármín Pataki, J. M. Zorrilla Matilla, D. Hsu, Z. Haiman, and I. Csabai, “Weak lensing cosmology with convolutional neural networks on noisy data,” *arXiv e-prints*, p. arXiv:1902.03663, Feb 2019.
- [145] A. Doussot, E. Eames, and B. Semelin, “Improved supervised learning methods for EoR parameters reconstruction,” *arXiv e-prints*, p. arXiv:1904.04106, Apr 2019.
- [146] J. Schmelzle, A. Lucchi, T. Kacprzak, A. Amara, R. Sgier, A. Réfrégier, and T. Hofmann, “Cosmological model discrimination with Deep Learning,” *arXiv e-prints*, p. arXiv:1707.05167, Jul 2017.
- [147] J. Merten, C. Giocoli, M. Baldi, M. Meneghetti, A. Peel, F. Lalande, J.-L. Starck, and

BIBLIOGRAPHY

- V. Pettorino, “On the dissection of degenerate cosmologies with machine learning,” *MNRAS*, p. 961, Apr 2019.
- [148] A. C. Rodríguez, T. Kacprzak, A. Lucchi, A. Amara, R. Sgier, J. Fluri, T. Hofmann, and A. Réfrégier, “Fast cosmic web simulations with generative adversarial networks,” *Computational Astrophysics and Cosmology*, vol. 5, no. 1, p. 4, Nov 2018.
- [149] P. Berger and G. Stein, “A volumetric deep Convolutional Neural Network for simulation of mock dark matter halo catalogues,” *MNRAS*, vol. 482, no. 3, pp. 2861–2871, Jan 2019.
- [150] S. He, Y. Li, Y. Feng, S. Ho, S. Ravanbakhsh, W. Chen, and B. Póczos, “Learning to Predict the Cosmological Structure Formation,” *arXiv e-prints*, p. arXiv:1811.06533, Nov 2018.
- [151] X. Zhang, Y. Wang, W. Zhang, Y. Sun, S. He, G. Contardo, F. Villaescusa-Navarro, and S. Ho, “From Dark Matter to Galaxies with Convolutional Networks,” *arXiv e-prints*, p. arXiv:1902.05965, Feb 2019.
- [152] D. Kodi Ramanah, T. Charnock, and G. Lavaux, “Painting halos from 3D dark matter fields using Wasserstein mapping networks,” *arXiv e-prints*, p. arXiv:1903.10524, Mar 2019.
- [153] T. Tröster, C. Ferguson, J. Harnois-Déraps, and I. G. McCarthy, “Painting with baryons: augmenting N-body simulations with gas using deep generative models,” *arXiv e-prints*, p. arXiv:1903.12173, Mar 2019.

BIBLIOGRAPHY

- [154] S. Agarwal, R. Davé, and B. A. Bassett, “Painting galaxies into dark matter haloes using machine learning,” *MNRAS*, vol. 478, no. 3, pp. 3410–3422, Aug 2018.
- [155] M. A. Aragon-Calvo, “Classifying the large-scale structure of the universe with deep neural networks,” *MNRAS*, vol. 484, no. 4, pp. 5771–5784, Apr 2019.
- [156] M. Ho, M. M. Rau, M. Ntampaka, A. Farahi, H. Trac, and B. Poczós, “A Robust and Efficient Deep Learning Method for Dynamical Mass Measurements of Galaxy Clusters,” *arXiv e-prints*, p. arXiv:1902.05950, Feb 2019.
- [157] D. Ribli, L. Dobos, and I. Csabai, “Galaxy shape measurement with convolutional neural networks,” *arXiv e-prints*, p. arXiv:1902.08161, Feb 2019.
- [158] C. Modi, Y. Feng, and U. Seljak, “Cosmological reconstruction from galaxy light: neural network based light-matter connection,” *Journal of Cosmology and Astro-Particle Physics*, vol. 2018, no. 10, p. 028, Oct 2018.
- [159] K. Fukushima, “Neocognitron: A self-organizing neural network model for a mechanism of pattern recognition unaffected by shift in position,” *Biological Cybernetics*, vol. 36, no. 4, pp. 193–202, Apr 1980. [Online]. Available: <https://doi.org/10.1007/BF00344251>
- [160] Y. Lecun, L. Bottou, Y. Bengio, and P. Haffner, “Gradient-based learning applied to document recognition,” in *Proceedings of the IEEE*, 1998, pp. 2278–2324.
- [161] A. Krizhevsky, I. Sutskever, and G. E. Hinton, “Imagenet classification with deep convolutional neural networks,” in *Advances in Neural Information Processing Sys-*

BIBLIOGRAPHY

- tems 25*, F. Pereira, C. J. C. Burges, L. Bottou, and K. Q. Weinberger, Eds. Curran Associates, Inc., 2012, pp. 1097–1105.
- [162] D. E. Rumelhart, G. E. Hinton, and R. J. Williams, “Neurocomputing: Foundations of research,” J. A. Anderson and E. Rosenfeld, Eds. Cambridge, MA, USA: MIT Press, 1988, ch. Learning Representations by Back-propagating Errors, pp. 696–699. [Online]. Available: <http://dl.acm.org/citation.cfm?id=65669.104451>
- [163] J. R. Bond, L. Kofman, and D. Pogosyan, “How filaments of galaxies are woven into the cosmic web,” *Nature*, vol. 380, no. 6575, pp. 603–606, Apr 1996.
- [164] M. D. Zeiler and R. Fergus, “Visualizing and Understanding Convolutional Networks,” *arXiv e-prints*, p. arXiv:1311.2901, Nov 2013.
- [165] J. Tremblay, A. Prakash, D. Acuna, M. Brophy, V. Jampani, C. Anil, T. To, E. Cameracci, S. Bochoon, and S. Birchfield, “Training Deep Networks with Synthetic Data: Bridging the Reality Gap by Domain Randomization,” *arXiv e-prints*, p. arXiv:1804.06516, Apr 2018.
- [166] N. Patki, R. Wedge, and K. Veeramachaneni, “The synthetic data vault,” in *DSAA*. IEEE, 2016, pp. 399–410.
- [167] N. Gillet, A. Mesinger, B. Greig, A. Liu, and G. Ucci, “Deep learning from 21-cm tomography of the Cosmic Dawn and Reionization,” *Mon. Not. Roy. Astron. Soc.*, vol. 484, no. 1, pp. 282–293, 2019.
- [168] S. Hassan, A. Liu, S. Kohn, J. E. Aguirre, P. La Plante, and A. Lidz, “Reionization

BIBLIOGRAPHY

- Models Classifier using 21cm Map Deep Learning,” in *Peering towards Cosmic Dawn*, ser. IAU Symposium, V. Jelić and T. van der Hulst, Eds., vol. 333, May 2018, pp. 47–51.
- [169] S. Hassan, A. Liu, S. Kohn, and P. La Plante, “Identifying reionization sources from 21 cm maps using Convolutional Neural Networks,” *MNRAS*, vol. 483, no. 2, pp. 2524–2537, Feb 2019.
- [170] J. Zamudio-Fernandez, A. Okan, F. Villaescusa-Navarro, S. Bilaloglu, A. Derin Cengiz, S. He, L. Perreault Levasseur, and S. Ho, “HIGAN: Cosmic Neutral Hydrogen with Generative Adversarial Networks,” *arXiv e-prints*, p. arXiv:1904.12846, Apr 2019.
- [171] A. D. Bolatto, M. Wolfire, and A. K. Leroy, “The CO-to-H₂ Conversion Factor,” *Annual Review of Astronomy and Astrophysics*, vol. 51, no. 1, pp. 207–268, Aug 2013.
- [172] C. Carilli and F. Walter, “Cool Gas in High Redshift Galaxies,” *Ann. Rev. Astron. Astrophys.*, vol. 51, pp. 105–161, 2013.
- [173] M. Heyer and T. M. Dame, “Molecular Clouds in the Milky Way,” *Annual Review of Astronomy and Astrophysics*, vol. 53, pp. 583–629, Aug 2015.
- [174] Planck Collaboration, Y. Akrami, F. Arroja, M. Ashdown, J. Aumont, C. Baccigalupi, M. Ballardini, A. J. Banday, R. B. Barreiro, N. Bartolo, S. Basak, R. Battye, K. Benabed, J. P. Bernard, M. Bersanelli, P. Bielewicz, J. J. Bock, J. R. Bond, J. Borrill, F. R. Bouchet, F. Boulanger, M. Bucher, C. Burigana, R. C. Butler, E. Calabrese,

BIBLIOGRAPHY

J. F. Cardoso, J. Carron, B. Casaponsa, A. Challinor, H. C. Chiang, L. P. L. Colombo, C. Combet, D. Contreras, B. P. Crill, F. Cuttaia, P. de Bernardis, G. de Zotti, J. Delabrouille, J. M. Delouis, F. X. Désert, E. Di Valentino, C. Dickinson, J. M. Diego, S. Donzelli, O. Doré, M. Douspis, A. Ducout, X. Dupac, G. Efstathiou, F. Elsner, T. A. Enßlin, H. K. Eriksen, E. Falgarone, Y. Fantaye, J. Fergusson, R. Fernandez-Cobos, F. Finelli, F. Forastieri, M. Frailis, E. Franceschi, A. Frolov, S. Galeotta, S. Galli, K. Ganga, R. T. Génova-Santos, M. Gerbino, T. Ghosh, J. González-Nuevo, K. M. Górski, S. Gratton, A. Gruppuso, J. E. Gudmundsson, J. Hamann, W. Handley, F. K. Hansen, G. Helou, D. Herranz, E. Hivon, Z. Huang, A. H. Jaffe, W. C. Jones, A. Karakci, E. Keihänen, R. Keskitalo, K. Kiiveri, J. Kim, T. S. Kisner, L. Knox, N. Krachmalnicoff, M. Kunz, H. Kurki-Suonio, G. Lagache, J. M. Lamarre, M. Langer, A. Lasenby, M. Lattanzi, C. R. Lawrence, M. Le Jeune, J. P. Leahy, J. Lesgourgues, F. Levrier, A. Lewis, M. Liguori, P. B. Lilje, M. Lilley, V. Lindholm, M. López-Caniego, P. M. Lubin, Y. Z. Ma, J. F. Macías-Pérez, G. Maggio, D. Maino, N. Mandolese, A. Mangilli, A. Marcos-Caballero, M. Maris, P. G. Martin, E. Martínez-González, S. Matarrese, N. Mauri, J. D. McEwen, P. D. Meerburg, P. R. Meinhold, A. Melchiorri, A. Mennella, M. Migliaccio, M. Millea, S. Mitra, M. A. Miville-Deschênes, D. Molinari, A. Moneti, L. Montier, G. Morgante, A. Moss, S. Motet, M. Münchmeyer, P. Natoli, H. U. Nørgaard-Nielsen, C. A. Oxborrow, L. Pagano, D. Paoletti, B. Partridge, G. Patanchon, T. J. Pearson, M. Peel, H. V. Peiris, F. Perrotta, V. Pettorino, F. Piacentini, L. Polastri, G. Polenta, J. L. Puget, J. P. Rachen, M. Reinecke, M. Remazeilles, A. Renzi, G. Rocha, C. Rosset, G. Roudier, J. A.

BIBLIOGRAPHY

- Rubiño-Martín, B. Ruiz-Granados, L. Salvati, M. Sandri, M. Savelainen, D. Scott, E. P. S. Shellard, M. Shiraishi, C. Sirignano, G. Sirri, L. D. Spencer, R. Sunyaev, A. S. Suur-Uski, J. A. Tauber, D. Tavagnacco, M. Tenti, L. Terenzi, L. Toffolatti, M. Tomasi, T. Trombetti, J. Valiviita, B. Van Tent, L. Vibert, P. Vielva, F. Villa, N. Vittorio, B. D. Wandelt, I. K. Wehus, M. White, S. D. M. White, A. Zacchei, and A. Zonca, “Planck 2018 results. I. Overview and the cosmological legacy of Planck,” *arXiv e-prints*, p. arXiv:1807.06205, Jul 2018.
- [175] G. Stein, M. A. Alvarez, and J. R. Bond, “The mass-Peak Patch algorithm for fast generation of deep all-sky dark matter halo catalogues and its N-body validation,” *MNRAS*, vol. 483, pp. 2236–2250, Feb 2019.
- [176] J. Tinker, A. V. Kravtsov, A. Klypin, K. Abazajian, M. Warren, G. Yepes, S. Gottlöber, and D. E. Holz, “Toward a Halo Mass Function for Precision Cosmology: The Limits of Universality,” *ApJ*, vol. 688, pp. 709–728, Dec 2008.
- [177] P. S. Behroozi, R. H. Wechsler, and C. Conroy, “On the Lack of Evolution in Galaxy Star Formation Efficiency,” *ApJ*, vol. 762, p. L31, Jan 2013.
- [178] —, “The Average Star Formation Histories of Galaxies in Dark Matter Halos from $z = 0-8$,” *ApJ*, vol. 770, p. 57, Jun. 2013.
- [179] H. Padmanabhan, “Constraining the CO intensity mapping power spectrum at intermediate redshifts,” *Mon. Not. Roy. Astron. Soc.*, vol. 475, no. 2, pp. 1477–1484, 2018.

BIBLIOGRAPHY

- [180] S. Muchovej *et al.*, “Radio Sources from a 31 GHz Sky Survey with the Sunyaev-Zel’dovich Array,” *Astrophys. J.*, vol. 716, pp. 521–529, 2010.
- [181] G. K. Keating *et al.*, “First Results from COPSS: The CO Power Spectrum Survey,” *Astrophys. J.*, vol. 814, no. 2, p. 140, 2015.
- [182] K. He, X. Zhang, S. Ren, and J. Sun, “Deep Residual Learning for Image Recognition,” *arXiv e-prints*, p. arXiv:1512.03385, Dec 2015.
- [183] A. L. Maas, A. Y. Hannun, and A. Y. Ng, “Rectifier nonlinearities improve neural network acoustic models,” in *in ICML Workshop on Deep Learning for Audio, Speech and Language Processing*, 2013.
- [184] S. Ioffe and C. Szegedy, “Batch Normalization: Accelerating Deep Network Training by Reducing Internal Covariate Shift,” *arXiv e-prints*, p. arXiv:1502.03167, Feb 2015.
- [185] F. Chollet *et al.*, “Keras,” <https://keras.io>, 2015.
- [186] M. Abadi, A. Agarwal, P. Barham, E. Brevdo, Z. Chen, C. Citro, G. S. Corrado, A. Davis, J. Dean, M. Devin, S. Ghemawat, I. Goodfellow, A. Harp, G. Irving, M. Isard, Y. Jia, R. Jozefowicz, L. Kaiser, M. Kudlur, J. Levenberg, D. Mané, R. Monga, S. Moore, D. Murray, C. Olah, M. Schuster, J. Shlens, B. Steiner, I. Sutskever, K. Talwar, P. Tucker, V. Vanhoucke, V. Vasudevan, F. Viégas, O. Vinyals, P. Warden, M. Wattenberg, M. Wicke, Y. Yu, and X. Zheng, “TensorFlow: Large-scale machine learning on heterogeneous systems,” 2015, software available from tensorflow.org. [Online]. Available: <https://www.tensorflow.org/>

BIBLIOGRAPHY

- [187] G. E. Hinton, N. Srivastava, A. Krizhevsky, I. Sutskever, and R. R. Salakhutdinov, “Improving neural networks by preventing co-adaptation of feature detectors,” *arXiv e-prints*, p. arXiv:1207.0580, Jul 2012.
- [188] N. Srivastava, G. Hinton, A. Krizhevsky, I. Sutskever, and R. Salakhutdinov, “Dropout: A simple way to prevent neural networks from overfitting,” *Journal of Machine Learning Research*, vol. 15, pp. 1929–1958, 2014. [Online]. Available: <http://jmlr.org/papers/v15/srivastava14a.html>
- [189] D. P. Kingma and J. Ba, “Adam: A Method for Stochastic Optimization,” *arXiv e-prints*, p. arXiv:1412.6980, Dec 2014.
- [190] P. C. Breysse and M. Rahman, “Feeding cosmic star formation: Exploring high-redshift molecular gas with CO intensity mapping,” *Mon. Not. Roy. Astron. Soc.*, vol. 468, no. 1, pp. 741–750, 2017.
- [191] L. Wolz, C. Blake, and J. S. B. Wyithe, “Determining the H I content of galaxies via intensity mapping cross-correlations,” *MNRAS*, vol. 470, no. 3, pp. 3220–3226, Sep 2017.
- [192] J. Fonseca, R. Maartens, and M. G. Santos, “Synergies between intensity maps of hydrogen lines,” *Mon. Not. Roy. Astron. Soc.*, vol. 479, no. 3, pp. 3490–3497, 2018.
- [193] D. T. Chung *et al.*, “Cross-correlating Carbon Monoxide Line-intensity Maps with Spectroscopic and Photometric Galaxy Surveys,” *Astrophys. J.*, vol. 872, no. 2, p. 186, 2019.

BIBLIOGRAPHY

- [194] Y. Gong, A. Cooray, M. B. Silva, M. Zemcov, C. Feng, M. G. Santos, O. Dore, and X. Chen, “Intensity Mapping of $H\alpha$, $H\beta$, [OII], and [OIII] Lines at $z < 5$,” *ApJ*, vol. 835, p. 273, Feb. 2017.
- [195] V. Gluscevic *et al.*, “Cosmological Probes of Dark Matter Interactions: The Next Decade,” 2019.
- [196] D. E. Kaplan, M. A. Luty, and K. M. Zurek, “Asymmetric Dark Matter,” *Phys. Rev.*, vol. D79, p. 115016, 2009.
- [197] E. Charles *et al.*, “Sensitivity Projections for Dark Matter Searches with the Fermi Large Area Telescope,” *Phys. Rept.*, vol. 636, pp. 1–46, 2016.
- [198] M. Di Mauro, X. Hou, C. Eckner, G. Zaharijas, and E. Charles, “Search for γ -ray emission from dark matter particle interactions from Andromeda and Triangulum Galaxies with the Fermi Large Area Telescope,” *Phys. Rev.*, vol. D99, no. 12, p. 123027, 2019.
- [199] C. Johnson, R. Caputo, C. Karwin, S. Murgia, S. Ritz, and J. Shelton, “Search for gamma-ray emission from p -wave dark matter annihilation in the Galactic Center,” *Phys. Rev.*, vol. D99, no. 10, p. 103007, 2019.
- [200] A. Albert *et al.*, “Searching for Dark Matter Annihilation in Recently Discovered Milky Way Satellites with Fermi-LAT,” *Astrophys. J.*, vol. 834, no. 2, p. 110, 2017.
- [201] R. Caputo, M. R. Buckley, P. Martin, E. Charles, A. M. Brooks, A. Drlica-Wagner, J. M. Gaskins, and M. Wood, “Search for Gamma-ray Emission from Dark Matter

BIBLIOGRAPHY

- Annihilation in the Small Magellanic Cloud with the Fermi Large Area Telescope,” *Phys. Rev.*, vol. D93, no. 6, p. 062004, 2016.
- [202] J. Amaré *et al.*, “First Results on Dark Matter Annual Modulation from the ANAIS-112 Experiment,” *Phys. Rev. Lett.*, vol. 123, no. 3, p. 031301, 2019.
- [203] H. Jiang *et al.*, “Limits on Light Weakly Interacting Massive Particles from the First 102.8 kg \times day Data of the CDEX-10 Experiment,” *Phys. Rev. Lett.*, vol. 120, no. 24, p. 241301, 2018.
- [204] R. Agnese *et al.*, “New Results from the Search for Low-Mass Weakly Interacting Massive Particles with the CDMS Low Ionization Threshold Experiment,” *Phys. Rev. Lett.*, vol. 116, no. 7, p. 071301, 2016.
- [205] G. Adhikari *et al.*, “An experiment to search for dark-matter interactions using sodium iodide detectors,” *Nature*, vol. 564, no. 7734, pp. 83–86, 2018, [erratum: *Nature*566,no.7742,E2(2019)].
- [206] R. Ajaj *et al.*, “Search for dark matter with a 231-day exposure of liquid argon using DEAP-3600 at SNOLAB,” *Phys. Rev.*, vol. D100, no. 2, p. 022004, 2019.
- [207] J. B. R. Battat *et al.*, “Low Threshold Results and Limits from the DRIFT Directional Dark Matter Detector,” *Astropart. Phys.*, vol. 91, pp. 65–74, 2017.
- [208] L. Hehn *et al.*, “Improved EDELWEISS-III sensitivity for low-mass WIMPs using a profile likelihood approach,” *Eur. Phys. J.*, vol. C76, no. 10, p. 548, 2016.

BIBLIOGRAPHY

- [209] D. S. Akerib *et al.*, “Results from a search for dark matter in the complete LUX exposure,” *Phys. Rev. Lett.*, vol. 118, no. 2, p. 021303, 2017.
- [210] E. Aprile *et al.*, “Dark Matter Search Results from a One Ton-Year Exposure of XENON1T,” *Phys. Rev. Lett.*, vol. 121, no. 11, p. 111302, 2018.
- [211] K. Abe *et al.*, “A direct dark matter search in XMASS-I,” *Phys. Lett.*, vol. B789, pp. 45–53, 2019.
- [212] O. Abramoff *et al.*, “SENSEI: Direct-Detection Constraints on Sub-GeV Dark Matter from a Shallow Underground Run Using a Prototype Skipper-CCD,” *Phys. Rev. Lett.*, vol. 122, no. 16, p. 161801, 2019.
- [213] R. Agnese *et al.*, “First Dark Matter Constraints from a SuperCDMS Single-Charge Sensitive Detector,” *Phys. Rev. Lett.*, vol. 121, no. 5, p. 051301, 2018, [erratum: *Phys. Rev. Lett.* 122, no. 6, 069901 (2019)].
- [214] Z. Li, V. Gluscevic, K. K. Boddy, and M. S. Madhavacheril, “Disentangling Dark Physics with Cosmic Microwave Background Experiments,” *Phys. Rev.*, vol. D98, no. 12, p. 123524, 2018.
- [215] S. L. Dubovsky, D. S. Gorbunov, and G. I. Rubtsov, “Narrowing the window for millicharged particles by CMB anisotropy,” *JETP Lett.*, vol. 79, pp. 1–5, 2004, [*Pisma Zh. Eksp. Teor. Fiz.* 79, 3 (2004)].
- [216] A. D. Dolgov, S. L. Dubovsky, G. I. Rubtsov, and I. I. Tkachev, “Constraints on

BIBLIOGRAPHY

- millicharged particles from Planck data,” *Phys. Rev.*, vol. D88, no. 11, p. 117701, 2013.
- [217] R. de Putter, O. Doré, J. Gleyzes, D. Green, and J. Meyers, “Dark Matter Interactions, Helium, and the Cosmic Microwave Background,” *Phys. Rev. Lett.*, vol. 122, no. 4, p. 041301, 2019.
- [218] C.-P. Ma and E. Bertschinger, “Cosmological perturbation theory in the synchronous and conformal Newtonian gauges,” *Astrophys. J.*, vol. 455, pp. 7–25, 1995.
- [219] U. Seljak and M. Zaldarriaga, “A Line of sight integration approach to cosmic microwave background anisotropies,” *Astrophys. J.*, vol. 469, pp. 437–444, 1996.
- [220] D. P. Finkbeiner, S. Galli, T. Lin, and T. R. Slatyer, “Searching for Dark Matter in the CMB: A Compact Parameterization of Energy Injection from New Physics,” *Phys. Rev.*, vol. D85, p. 043522, 2012.
- [221] J. Abdallah *et al.*, “Simplified Models for Dark Matter Searches at the LHC,” *Phys. Dark Univ.*, vol. 9-10, pp. 8–23, 2015.
- [222] J. Fan, M. Reece, and L.-T. Wang, “Non-relativistic effective theory of dark matter direct detection,” *JCAP*, vol. 1011, p. 042, 2010.
- [223] A. L. Fitzpatrick, W. Haxton, E. Katz, N. Lubbers, and Y. Xu, “The Effective Field Theory of Dark Matter Direct Detection,” *JCAP*, vol. 1302, p. 004, 2013.
- [224] N. Anand, A. L. Fitzpatrick, and W. C. Haxton, “Weakly interacting massive particle-nucleus elastic scattering response,” *Phys. Rev.*, vol. C89, no. 6, p. 065501, 2014.

BIBLIOGRAPHY

- [225] J. B. Dent, L. M. Krauss, J. L. Newstead, and S. Sabharwal, “General analysis of direct dark matter detection: From microphysics to observational signatures,” *Phys. Rev.*, vol. D92, no. 6, p. 063515, 2015.
- [226] J. Kumar and D. Marfatia, “Matrix element analyses of dark matter scattering and annihilation,” *Phys. Rev.*, vol. D88, no. 1, p. 014035, 2013.
- [227] E. D. Kovetz, V. Poulin, V. Gluscevic, K. K. Boddy, R. Barkana, and M. Kamionkowski, “Tighter limits on dark matter explanations of the anomalous EDGES 21 cm signal,” *Phys. Rev.*, vol. D98, no. 10, p. 103529, 2018.
- [228] J. B. Muñoz and A. Loeb, “A small amount of mini-charged dark matter could cool the baryons in the early Universe,” *Nature*, vol. 557, no. 7707, p. 684, 2018.
- [229] D. Blas, J. Lesgourgues, and T. Tram, “The Cosmic Linear Anisotropy Solving System (CLASS) II: Approximation schemes,” *JCAP*, vol. 1107, p. 034, 2011.
- [230] T. R. Slatyer, “Indirect Dark Matter Signatures in the Cosmic Dark Ages II. Ionization, Heating and Photon Production from Arbitrary Energy Injections,” 2015.
- [231] H. Liu, G. W. Ridgway, and T. R. Slatyer, “DarkHistory: A code package for calculating modified cosmic ionization and thermal histories with dark matter and other exotic energy injections,” 2019.
- [232] N. Aghanim *et al.*, “Planck 2018 results. V. CMB power spectra and likelihoods,” 2019.

BIBLIOGRAPHY

- [233] R. Adam *et al.*, “Planck 2015 results. I. Overview of products and scientific results,” *Astron. Astrophys.*, vol. 594, p. A1, 2016.
- [234] N. Aghanim *et al.*, “Planck 2015 results. XI. CMB power spectra, likelihoods, and robustness of parameters,” *Astron. Astrophys.*, vol. 594, p. A11, 2016.
- [235] B. Audren, J. Lesgourgues, K. Benabed, and S. Prunet, “Conservative Constraints on Early Cosmology: an illustration of the Monte Python cosmological parameter inference code,” *JCAP*, vol. 1302, p. 001, 2013.
- [236] T. Brinckmann and J. Lesgourgues, “MontePython 3: boosted MCMC sampler and other features,” 2018.
- [237] A. Gelman and D. B. Rubin, “Inference from Iterative Simulation Using Multiple Sequences,” *Statist. Sci.*, vol. 7, pp. 457–472, 1992.
- [238] K. Sigurdson, M. Doran, A. Kurylov, R. R. Caldwell, and M. Kamionkowski, “Dark-matter electric and magnetic dipole moments,” *Phys. Rev.*, vol. D70, p. 083501, 2004, [Erratum: *Phys. Rev.*D73,089903(2006)].
- [239] D. McCammon *et al.*, “A High spectral resolution observation of the soft x-ray diffuse background with thermal detectors,” *Astrophys. J.*, vol. 576, pp. 188–203, 2002.
- [240] A. Berlin, D. Hooper, G. Krnjaic, and S. D. McDermott, “Severely Constraining Dark Matter Interpretations of the 21-cm Anomaly,” *Phys. Rev. Lett.*, vol. 121, no. 1, p. 011102, 2018.
- [241] R. Barkana, N. J. Outmezguine, D. Redigolo, and T. Volansky, “Strong constraints on

BIBLIOGRAPHY

- light dark matter interpretation of the EDGES signal,” *Phys. Rev.*, vol. D98, no. 10, p. 103005, 2018.
- [242] J. D. Bowman, A. E. E. Rogers, R. A. Monsalve, T. J. Mozdzen, and N. Mahesh, “An absorption profile centred at 78 megahertz in the sky-averaged spectrum,” *Nature*, vol. 555, no. 7694, pp. 67–70, 2018.
- [243] T. R. Slatyer and C.-L. Wu, “Early-Universe constraints on dark matter-baryon scattering and their implications for a global 21 cm signal,” *Phys. Rev.*, vol. D98, no. 2, p. 023013, 2018.
- [244] X. Chu, J. Pradler, and L. Semmelrock, “Light dark states with electromagnetic form factors,” *Phys. Rev.*, vol. D99, no. 1, p. 015040, 2019.
- [245] S. D. McDermott, H.-B. Yu, and K. M. Zurek, “Turning off the Lights: How Dark is Dark Matter?” *Phys. Rev.*, vol. D83, p. 063509, 2011.
- [246] C. Dvorkin, T. Lin, and K. Schutz, “Making dark matter out of light: freeze-in from plasma effects,” *Phys. Rev.*, vol. D99, no. 11, p. 115009, 2019.

Vita



Daniel Pfeffer was born in New Brunswick, New Jersey on November 4th, 1991. In 2010, he went to Case Western Reserve University to obtain a bachelors degree in an undecided field of engineering, but switched to physics. He obtained the Case Western Reserve B.S. Chandrasekhar Prize for excellence in his junior year and graduated summa cum laude in 2014.

Throughout his undergraduate education he became interested in cosmology. In 2014 he joined the Department of Physics & Astronomy at Johns Hopkins University and joined the group of Professor Marc Kamionkowski soon after. While at Johns Hopkins, his teaching skills were recognized with the Rowland Prize for Innovation and Excellence in Teaching. Following the completion of his PhD in 2019, he plans to transition into data-science.